Separable Dorsal Raphe Dopamine Projections mediate the Facets of Loneliness-like state

Christopher R. Lee [1,2,3,6], Gillian A. Matthews[1,4,6], Mackenzie E. Lemieux[1,4,6], Elizabeth M. Wasserlein[4], Matilde Borio[1,4], Raymundo L. Miranda[1,2,4], Laurel R. Keyes[1,3], Gates P. Schneider[1,3], Caroline Jia[1,2,3], Andrea Tran[1], Faith Aloboudi[1], May G. Chan[1,3], Enzo Peroni[4], Grace S. Pereira[4], Alba López-Moraga[4], Anna Pallé[1,4], Eyal Y. Kimchi[4], Nancy Padilla-Coreano[1,4], Romy Wichmann[1,3,4], Kay M. Tye[1,2,3,4,5,*]

[1]Salk Institute for Biological Studies, 10010 N Torrey Pines Rd, La Jolla, CA 92037, USA.

[2]Neurosciences Graduate Program, University of California San Diego, La Jolla, CA 92093, USA

[3]Howard Hughes Medical Institute, 10010 N Torrey Pines Rd, La Jolla, CA 92037, USA.

[4]The Picower Institute for Learning and Memory, Department of Brain and Cognitive Sciences, Massachusetts Institute of Technology, Cambridge, MA 02139, USA.

[5]Kavli Institute for Brain and Mind, La Jolla, CA, USA

[6]These authors contributed equally.

*Address Correspondence to: tye@salk.edu (K.M.T.).

Abstract

Affiliative social connections facilitate well-being and survival in numerous species. Engaging in social interactions requires positive or negative motivational drive, elicited through coordinated activity across neural circuits. However, the identity, interconnectivity, and functional encoding of social information within these circuits remains poorly understood. Here, we focus on downstream projections of dorsal raphe nucleus (DRN) dopamine neurons (DRN^{DAT}), which we previously implicated in social motivation alongside an aversive affective state. We show that three prominent DRN^{DAT} projections – to the bed nucleus of the stria terminalis (BNST), central amygdala (CeA), and posterior basolateral amygdala (BLP) – play separable roles in behavior, despite substantial collateralization. Photoactivation of the DRN^{DAT}-CeA projection promoted social behavior and photostimulation of the DRN^{DAT}-BNST projection promoted exploratory behavior, while the DRN^{DAT}-BLP projection supported place avoidance, suggesting a negative affective state. Downstream regions showed diverse receptor expression, poising DRN^{DAT} neurons to act through dopamine, neuropeptide, and glutamate transmission. Furthermore, we show *ex vivo* that the effect of DRN^{DAT} photostimulation on downstream neuron excitability depended on region and baseline cell properties, resulting in excitatory responses in BNST cells and diverse responses in CeA and BLP. Finally, *in vivo* microendoscopic cellular-resolution recordings in the CeA with DRN^{DAT} photostimulation revealed a correlation between social behavior and neurons excited by social stimuli– suggesting that increased dopamine tone may recruit different CeA neurons to social ensembles. Collectively, these circuit features may facilitate a coordinated, but flexible, response in the presence of social stimuli that can be flexibly guided based on the internal social homeostatic need state of the individual.

INTRODUCTION

A close social network confers a survival advantage, both in the wild and in the laboratory [1–3]. Indeed, our brains have evolved to adapt to many changing conditions, including when we are with others and when we are alone. Many neuromodulatory systems and neural circuits engaged in social behaviors may serve a distinct function when social stimuli are not present. In non-social contexts, dopamine transporter-expressing dorsal raphe nucleus (DRN^{DAT}) neurons can promote incentive memory expression[4], antinociception [5,6], fear response [7], and arousal [8–10] – showing a clear role in many functions essential for survival. Moreover, DRN^{DAT} neurons undergo synaptic strengthening after social isolation and increase responsiveness to social stimuli, and stimulation of these neurons induces a prosocial state[11]. Strikingly, a functional imaging study in humans similarly revealed that 10 hours of social isolation heightened midbrain responses to social stimuli[12]. In mice, we further demonstrated that photostimulation of DRN^{DAT} neurons not only promoted social preference, but also induced place avoidance, suggesting an aversive internal state [11]. This led us to infer a role for these neurons in motivating social approach, driven by the desire to quell a negative state [13], and playing a role in social homeostasis[14,15].

Taken together, this suggests a broad functional role for DRN^{DAT} neurons in motivating adaptive, survival-promoting behaviors under both social and non-social conditions. While the multi-functional role of dopamine neurons in the DRN seems clear, it is yet unclear how these cells exert their influence at a circuit level, and the question remains: how do DRN^{DAT} neurons simultaneously motivate social approach while also inducing a negative state consistent with place avoidance? What downstream targets receive this signal, and how do they respond?

There are several circuit motifs and neural encoding strategies that could enable DRN^{DAT} neurons to simultaneous regulate these behavioral states and motivate adaptive responses. In a drive-state sequence model, if these DRN^{DAT} neurons were the control center in the social homeostat[14,15], the unpleasant state of being isolated could then feed-forward in a sequential chain to induce motivation to rectify this social deficit. However, in an effector state activation model, many parallel actions may be taken to address the challenge, and a pervasive behavioral state may be triggered by a neuromodulatory broadcast signal. In a parallel circuit model, distinct functional roles may be associated with projection-defined subpopulations in parallel (e.g.[16–22]), and neurons may simultaneously encode multiple types of information (i.e. exhibit 'mixed selectivity' [23,24]) or behavioral output may be governed by context- or state-dependency (e.g.[25–28]). Yet, the mechanisms through which DRN^{DAT} neurons exert their influence over social behavior has yet to be unraveled.

Here, we addressed the question of how DRN^{DAT} neurons modulate both sociability and valence, by exploring the functional role and anatomical targets of distinct DRN^{DAT} projections in mice. We show that parallel DRN^{DAT} projections to different targets play separable roles in behavior, in spite of their heavily-collateralizing anatomical arrangement. Downstream, we find that within DRN^{DAT} terminal fields, there is spatial segregation of dopamine and neuropeptide receptor expression. Furthermore, photostimulation of DRN^{DAT} inputs can modulate downstream neuronal excitability depending on their baseline cell properties. Lastly, we find that DRN^{DAT} input enables a shift in central amygdala dynamics that allows it to predict social preference. These findings highlight the anatomical and functional heterogeneity that exists at multiple levels within the DRN^{DAT} system. We suggest this organization may underlie the capacity of the DRN^{DAT} system to exert a broad influence over different forms of behavior:

allowing coordinated control over downstream neuronal activity and across the brain to signal a behavioral state that mimics a loneliness-like phenotype.

RESULTS

DRN^{DAT} neurons project to and exhibit dense collateralization to distinct subregions of the amygdala and extended amygdala.

To explore the circuit motifs [29] and computational implementation [30] through which the DRN^{DAT} system might operate, we examined whether discrete DRN^{DAT} projections underlie distinct features of behavior. Prominent DRN^{DAT} projections were identified by quantifying downstream fluorescence following Cre-dependent expression of eYFP in dopamine transporter (DAT)::IRES-Cre mice [11,31–33](Figure 1—figure supplement 1). We observed a distinct pattern of innervation arising from ventral tegmental area $(VTA)^{DAT}$ and DRN^{DAT} subpopulations (Figure 1A-D), with DRN^{DAT} projections most densely targeting the oval nucleus of the BNST (ovBNST) and lateral nucleus of the central amygdala (CeL). We also observed weaker, but significant, input to the posterior part of the basolateral amygdala (BLP), consistent with previous tracing studies [4,32,34–36]. Given that the extended amygdala and basolateral amygdala complex have been implicated in aversion- [37–40] and reward-related processes [20,41–45], and connect with hindbrain motor nuclei to elicit autonomic and behavioral changes, we focused on these DRN^{DAT} projections (Figure 1D).

We next considered the anatomical organization of these projections to determine whether form gives rise to function. In other words, we investigated whether DRN^{DAT} outputs exhibit a circuit arrangement that facilitates a coordinated behavioral response. Axonal collateralization is one circuit feature that facilitates coordinated activity across broadly distributed structures [46]. Although VTA^{DAT} projections to striatal and cortical regions typically show little evidence of collateralization [47–51], in contrast, DRN serotonergic neurons collateralize heavily to innervate the prefrontal cortex, striatum, midbrain, and amygdala [52–54]. However, it has yet to be determined whether DRN^{DAT} neurons are endowed with this property.

To assess whether DRN^{DAT} neurons exhibit axon collaterals, we performed dual retrograde tracing with fluorophore-conjugated cholera toxin subunit B (CTB) [55]. We injected each tracer into two of the three downstream sites (BNST, CeA, and/or BLP) (Figure 1E-F and Figure 1—figure supplement 2A-C) and, after 7 days for retrograde transport, we examined CTB-expressing cells in the DRN that were co-labelled with tyrosine hydroxylase (TH; Figure 1G). CTB injections into the BNST and CeA resulted in numerous TH+ cells labelled with both CTB-conjugated fluorophores, but fewer dual-labelled cells were observed when injections were placed in the BNST and BLP, or CeA and BLP (Figure 1H and Figure 1—figure supplement 2D-E). These data suggest significant collateralization to the extended amygdala, which includes the BNST and CeA [4,39]. To confirm the presence of axon collaterals we employed an intersectional viral strategy to selectively label CeA-projecting DRN^{DAT} neurons with cytoplasmic eYFP (Figure 1—figure supplement 2F-G). This resulted in eYFP-expressing terminals both in the CeA and in the BNST (Figure 1—figure supplement 2H-I).

DRN^{DAT}-BLP photostimulation promotes place avoidance.

We next considered whether DRN^{DAT} projections to the BNST, CeA, and BLP play separable or overlapping functional roles in modulating behavior. VTA dopaminergic input to the BNST and CeA has been implicated in threat discrimination [56,57], anxiety-related behavior [58], and drug-induced reward [59–62], while in the BLA complex, dopamine signaling supports both fear [63–66] and appetitive learning [45,67]. However, the question remains: do the same DRN^{DAT} projection neurons mediate different facets of a loneliness-like state, such as aversion, vigilance, and social motivation?

To test the hypothesis that distinct DRN^{DAT} projections promote sociability, vigilance, and place avoidance [11], we performed projection-specific ChR2-mediated photostimulation. We injected an AAV enabling Cre-dependent expression of ChR2 into the DRN of DAT::Cre male mice, and implanted optic fibers over the BNST, CeA, or BLP (Figure 2A and Figure 2—figure supplement 1A-F). Given that we previously observed that behavioral effects of DRN^{DAT} photostimulation were predicted by an animal's social rank [11], we also assessed relative social dominance using the tube test [68–70] prior to behavioral assays and photostimulation (Figure 2A and Figure 2—figure supplement 1G-H).

We first assessed whether photostimulation was sufficient to support place preference using the real-time place-preference (RTPP) assay. Here, we found that photostimulation of the DRN^{DAT}-BLP projection, but not the projection to the BNST or CeA, produced avoidance of the stimulation zone, relative to eYFP controls (Figure 2B-G). However, we did not find a significant correlation between social dominance and the magnitude of this effect (Figure 2H-J). Importantly, we did not detect an effect of photostimulation of DRN^{DAT} projections on operant intracranial self-stimulation (Figure 2—figure supplement 2).

DRN^{DAT}-BNST photostimulation promotes non-social exploration.

Next, we considered whether DRN^{DAT} projections to the BNST, CeA, or BLP play a role in increasing vigilance, a common behavioral marker in individuals experiencing loneliness[71,72]. To assess how projection-specific photostimulation of DRN^{DAT} terminals affected exploratory behavior, we used the open field test (OFT) and elevated plus maze (EPM). While we found no effect of optical stimulation of DRN^{DAT} terminals on locomotion or time in center in the OFT (Figure 3—figure supplement 1), we found stimulation of DRN^{DAT} terminals in the BNST (but not in the CeA or BLP) resulted in a weak trend toward increased time spent in the open arm of the EPM (Figure 3A-C), which can be interpreted as exploratory behavior linked with a vigilant state[73]. However, we found no correlation between social dominance and open arm time (Figure 3D-F). Strikingly, during social interaction with a novel juvenile in the home-cage, we found that photoactivation of the DRN^{DAT}-BNST projection increased rearing behavior (a form of nonsocial exploration[74,75]; Figure 3G-L), an effect that was not previously observed with cell body photostimulation[11]. However, we did not find a significant correlation between social dominance and the expression of optically-induced rearing behavior (Figure 3J-L).

DRN^{DAT}-CeA photostimulation promotes sociability.

To assess how projection-specific photostimulation of DRN^{DAT} terminals affected social preference, we used the three chamber sociability task [76], where group-housed mice freely-explored a

chamber containing a novel juvenile mouse and a novel object at opposite ends (Figure 4A-C). This revealed that optical stimulation of the DRN^{DAT}-CeA projection increased social preference, but no significant effect was observed with photostimulation of either the DRN^{DAT}-BNST or DRN^{DAT}-BLP projections (Figure 4D-F). Furthermore, we found that the optically-induced change in social preference in DRN^{DAT}-CeA mice was positively correlated with social dominance, suggesting that photostimulation elicited a greater increase in sociability in dominant mice (Figure 4G-I). This emulates the previous association found with photostimulation at the cell body level and social dominance[11].

Next, to gain further insight into the functional divergence of DRN^{DAT} projections in ethological behaviors, we assessed the effects of photostimulation on social interaction with a novel juvenile in the home-cage. Here, photoactivation of the DRN^{DAT}-CeA projection increased face sniffing of the juvenile mouse, consistent with a pro-social role for this projection (Figure 4J-L), although no correlation between optically-induced change in face sniffing and social dominance was observed (Figure 4M-O). When we plotted the difference score (ON-OFF) for face sniffing against rearing (ON-OFF) (Figure 4—figure supplement 1A-C), we observed that DRN^{DAT}-BNST mice tended to engage in more rearing and less face sniffing during photostimulation (i.e. located in the upper left quadrant) whereas DRN^{DAT}-CeA mice tended to exhibit less rearing and more face sniffing during photostimulation (i.e. located in the lower right quadrant).

To explore the relationship between social dominance and baseline behavioral profile, we applied a data-driven approach by examining behavioral measures obtained from different assays in a correlation matrix (Figure 4—figure supplement 1D). This showed a weak, negative correlation between social dominance and open arm time in the elevated plus maze (EPM) – consistent with a previous report of higher trait anxiety in dominant mice [77]. However, social dominance did not correlate significantly with any other behavioral variable. Additionally, our analysis of baseline behavioral profile revealed a robust negative correlation between the time spent engaged in social sniffing and time spent rearing (Figure 4—figure supplement 1D). Furthermore, following dimensionality reduction on baseline behavioral variables, we did not find clearly differentiated clusters of high- and low-ranked mice (Figure 4—figure supplement 1E), suggesting that the variation governing these latent behavioral features is not related to social rank.

Finally, to determine whether DRN^{DAT}-CeA photostimulation affected the probability of behavioral state transition[78,79], we examined the sequential structure of behavior using a First-order Markov model [79,80]. Considering a 2-state model consisting of 'social' and 'nonsocial' behaviors (Figure 4P), we found that photostimulation in DRN^{DAT}-CeA mice did not significantly change the probability of transitioning within social and nonsocial state (Figure 4Q), but did significantly change the probability of transitioning between social and nonsocial states (Figure 4R). This suggests that the DRN^{DAT}-CeA projection may increase engagement in social behavior by altering the overall structure of behavioral transitions.

DRN^{DAT} terminal fields contain spatially-segregated dopamine and neuropeptide receptor populations.

Our data suggest that DRN^{DAT} projections exert divergent effects over behavior, despite substantial overlap in their upstream cells of origin. Given this overlap, we reasoned that one mechanism through which these projections might achieve distinct behavioral effects is via differential recruitment of downstream signaling pathways. We, therefore, next considered whether the pattern of receptor expression differed within the DRN^{DAT} terminal field of these downstream regions.

Subsets of DRN^{DAT} neurons co-express vasoactive intestinal peptide (VIP) and neuropeptide-W (NPW) [81–83], and so we examined both dopamine (*Drd1* and *Drd2*) and neuropeptide (*Vipr2* and *Npbwr1*) receptor expression within DRN^{DAT} terminal fields. To achieve this, we performed single molecule fluorescence *in situ* hybridization (smFISH) using RNAscope (Figure 5—figure supplement 1A-B). In the BNST and CeA we observed a strikingly similar pattern of receptor expression with dense neuropeptide receptor expression in the oval BNST and ventromedial CeL, and a high degree of co-localization (Figure 5A-H and Figure 5—figure supplement 1C-H). In the BNST and CeA subregions containing the highest density of DRN^{DAT} terminals, dopamine receptor expression was relatively more sparse, with *Drd2* more abundant than *Drd1*, as previously described [43,56,58,84,85] (Figure 5A-H). The DRN^{DAT} terminal field of the BLP displayed a markedly different receptor expression pattern, dominated by *Drd1* (Figure 5I-L and Figure 5—figure supplement 1I-K), consistent with previous reports [58,67,84]. Thus, in contrast to the BNST and CeA, the effects of DRN^{DAT} input to the BLP may be predominantly mediated via D_1-receptor signaling. Collectively, this expression pattern suggests that the dopamine- and neuropeptide-mediated effects of DRN^{DAT} input may be spatially-segregated within downstream regions – providing the infrastructure for divergent modulation of cellular subsets.

DRN^{DAT} input has divergent effects on downstream cellular excitability.

Our data suggest that DRN^{DAT} projections exert divergent effects over behavior, despite substantial overlap in their upstream cells of origin. One mechanism through which these projections might achieve distinct behavioral effects is via differential modulation of activity in downstream neurons. The multi-transmitter phenotype of DRN^{DAT} neurons [81,82,86,87], regionally-distinct downstream receptor expression, and the observed pre- and post-synaptic actions of exogenously applied dopamine [88–95] provides optimal conditions for diverse modulation of neural activity. However, it remains unknown how temporally-precise activation of DRN^{DAT} terminals influences excitability at the single-cell level.

We, therefore, next examined how DRN^{DAT} input affects downstream excitability. To achieve this, we expressed ChR2 in DRN^{DAT} neurons, and used *ex vivo* electrophysiology to record from downstream neurons (Figure 6A-C and Figure 6—figure supplement 1A-C). Optical stimulation at the resting membrane potential evoked both excitatory and inhibitory post-synaptic potentials (EPSPs and IPSPs) in downstream cells (Figure 6D-F), which were typically monosynaptic (Figure 6—figure supplement 1D-E). During spontaneous firing, BNST cells were universally excited whereas more diverse responses were observed with the BLP and CeA (Figure 6G-K and Figure 6—figure supplement 1F-G). The fast rise and decay kinetics of the EPSP suggest an AMPAR-mediated potential, resulting from glutamate co-release [5,11], whereas the slow IPSP kinetics are consistent with opening of GIRK channels, which can occur via D_2-receptor [96,97] or $GABA\text{-}_B$ receptor signaling [98–100].

Given the diversity of responses observed in the CeA and BLP, we next examined these downstream cells in more detail. To assess whether baseline electrophysiological properties predicted the optically-evoked response, we used unsupervised agglomerative hierarchical clustering to classify downstream cells (Figure 6L-M). This established approach has been successfully applied to electrophysiological datasets to reveal distinct neuronal subclasses [101–103]. The resulting dendrograms yielded two major clusters in the CeA and BLP, with distinct electrophysiological characteristics (Figure 6N-Q and Figure 6—figure supplement 1H-K). CeA cells in cluster 1 represented ‘late-firing’ neurons, whereas cluster 2 were typical of ‘regular-firing’ neurons [104–106]. Strikingly, these clusters exhibited

dramatically different response to DRN^{DAT} photostimulation, with cluster 1 'late-firing' neurons excited and cluster 2 'regular-firing' neurons mostly inhibited (Figure 6O). Similarly, BLP cells delineated into two major clusters, with properties characteristic of pyramidal neurons (cluster 1) and GABAergic interneurons (cluster 2) (Figure 6P-Q). These clusters showed remarkably different responses to DRN^{DAT} input, with 93% of putative pyramidal neurons showing an inhibitory response, and 62% of putative GABAergic interneurons showing an excitatory response (Figure 6Q). In addition, clustering CeA and BLP cells together yielded a very similar result (Figure 6—figure supplement 1L-N). Thus, while photoactivation of DRN^{DAT} terminals elicits heterogeneous responses in downstream neurons, baseline cell properties strongly predict their response, suggesting robust synaptic organization. The opposing nature of these responses, in different neuronal subsets, suggests that – rather than inducing an overall augmentation or suppression of activity – DRN^{DAT} input may adjust the *pattern* of downstream activity, in order to exert a functional shift in behavior.

DRN^{DAT} input enables a functional shift in CeA dynamics to predict social preference.

Our data thus far suggest that photostimulation of DRN^{DAT} projections to downstream extended amygdala targets elicits divergent behaviors that are, together, congruent with a loneliness-like state, with the DRN^{DAT}-CeA projection promoting sociability. Considering the diversity of responses in the CeA elicited by DRN^{DAT} input *ex vivo*, we next wondered how DRN^{DAT} input into the CeA *in vivo* during a behaviorally-relevant task may modify how the CeA represents social information. Neuromodulatory input has been previously shown to alter responses to salient stimuli—for instance, stimulation of VTA dopamine terminals increases the signal-to-noise ratio to aversive stimuli in projection-specific populations of prefrontal cortex neurons [107]. However, how DRN^{DAT} input modifies the coding scheme of CeA neurons for social information remains unknown.

Therefore, to test the hypothesis that DRN^{DAT} input alters the responses of CeA neurons to functionally-relevant stimuli, we examined the dynamics of CeA neurons while simultaneously stimulating DRN^{DAT} terminals during a three chamber sociability task. To achieve this, we expressed the calcium indicator GCaMP7f nonspecifically in the CeA and either the red-shifted opsin ChrimsonR or a control fluorophore (TdTomato) in the DRN of DAT::Cre mice, and additionally implanted a gradient index (GRIN) lens over the CeA (Figure 7A and Figure 7—figure supplement 1A). This allowed us to stimulate DRN^{DAT} terminals in the CeA while resolving single-cell calcium dynamics in the CeA *in vivo* (Figure 7B). We confirmed *ex vivo* that blue light delivery alone onto DRN^{DAT} terminals did not elicit a ChrimsonR-mediated postsynaptic potential in CeA neurons (Figure 7—figure supplement 1B-F), and that red light delivery was still capable of eliciting ChrimsonR-mediated EPSPs and IPSPs during continuous delivery of blue light (Figure 7—figure supplement 1G-I).

We then performed microendoscopic epifluorescent calcium imaging during the three-chamber sociability task where mice freely-explored a chamber containing a novel juvenile mouse and a novel object at opposite ends. Given that social isolation produces changes in long-term potentiation of synapses onto DRN^{DAT} neurons[11], we were limited to a single manipulation of social isolation for each mouse. We hypothesized that stimulation of DRN^{DAT} inputs to CeA would mimic a loneliness-like state, consistent with our ChR2 manipulations with group-housed mice. Thus, we compared three conditions —group-housed without DRN^{DAT} stimulation (GH off), group-housed with DRN^{DAT} stimulation (GH on),

and 24 hours socially isolated without DRN^{DAT} stimulation (SI off) (Figure 7C-D) to allow for within-subjects comparisons.

In contrast to the photostimulation experiments in Figure 4, here we aimed to investigate the impact of DRN^{DAT} neuron stimulation on neural dynamics within the CeA without inducing robust behavioral changes that could introduce sensorimotor confounds to changes in neural activity due to stimulation. We successfully optimized viral expression and illumination parameters to minimize changes in social preference with DRN^{DAT}-CeA with ChrimsonR to prioritize comparison of the neural dynamics (Figure 7E) and also did not observe any behavioral effects of illumination in TdTomato expressing mice (Figure 7—figure supplement 1J-K).

We then aligned the recorded CeA calcium traces with social cup and object cup interactions and found a striking diversity of neuronal responses to these stimuli under the three experimental conditions (Figure 7—figure supplement 2A-B). We next determined the response strength of individual CeA neurons to either stimulus under the three conditions (Figure 7F-G) using an area under ROC curve-based approach[108,109] to determine responsiveness of CeA neurons to social and object stimuli (Figure 7—figure supplement 1M). At a single-cell level, we did not observe significant changes in CeA response strength or proportion of neurons significantly responding to social or object stimuli across the three conditions (Figure 7G-H). However, we did find a trend indicating stronger responses toward social stimuli compared to object stimuli in the GH on condition compared to the GH off condition in mice expressing ChrimsonR (Figure 7J), but not TdTomato (Figure 7—figure supplement 1L) in DRN^{DAT} neurons. Importantly, in co-registered neurons, we found little overlap between CeA neurons excited by the social stimulus in both GH on and GH off conditions (Figure 7I), suggesting that DRN^{DAT} terminal stimulation may recruit separate ensembles of CeA neurons to represent social stimuli. Considering the variability in social preference behavior across mice and the diverse effects of photostimulation depending on the mouse's social history, we next considered the responses of CeA neurons to social and object stimuli on an animal-by-animal basis. While we did not observe significant changes in the proportion of excitatory or inhibitory responses to social or object stimuli across the three conditions (Figure 7K-L), we did find a significant positive correlation between the proportion of socially-excited CeA neurons and social preference in the GH on condition, but not in the GH off or SI off conditions (Figure 7M). Importantly, we do not observe a correlation between social preference and object-excited CeA neurons (Figure 7—figure supplement 1N) or socially-inhibited CeA neurons (Figure 7—figure supplement 1O). This result may suggest that DRN^{DAT} input in the CeA in a behaviorally-relevant task allows for a functional shift in its dynamics that enables it to predict the amount of social preference the mouse exhibits.

DRN^{DAT}-CeA photoinhibition blocks isolation-induced sociability

Finally, considering that the DRN^{DAT}-CeA projection is sufficient in promoting sociability, we next assessed whether activity in the DRN^{DAT}-CeA projection is necessary for the rebound in sociability that occurs following acute social isolation[11]. We injected an AAV enabling Cre-dependent expression of NpHR into the DRN of DAT::Cre male mice, and implanted optic fibers over the BNST, CeA, or BLP (Figure 8A). We allowed 7 weeks for adequate terminal expression, after which we inhibited DRN^{DAT} terminals in the BNST, CeA, and BLP while mice performed the three-chamber sociability task (Figure 8B). Inhibition of DRN^{DAT} terminals in downstream regions while mice were group-housed did not change social preference (Figure 8—figure supplement 1A-B). However, inhibition of DRN^{DAT} terminals in CeA,

but not BNST or BLP, blocked the rebound in sociability associated with acute social isolation (Figure 8C). Additionally, we found that optically-inhibited changes in social preference in DRN^{DAT}-CeA mice were negatively correlated with social dominance (Figure 8D), suggesting that the DRN^{DAT}-CeA projection is necessary for the expression of isolation-induced social rebound in a rank-dependent manner.

DISCUSSION

Neural circuits that motivate social approach are essential in maintaining social connections and preventing isolation. Here we show that DRN^{DAT} neurons can exert a multi-faceted influence over behavior, with the pro-social effects mediated by the projection to the CeA, the avoidance effects mediated by the projection to the BLP, and the pro-exploratory effects mediated by the projection to the BNST. Our data suggest these effects are enabled via separable functional projections, dense collateralization, co-transmission, and precisely-organized synaptic connectivity. Taken together, these circuit features may facilitate a coordinated, but flexible, response in the presence of social stimuli, that can be flexibly guided based on internal social homeostatic need state.

DRN^{DAT} circuit arrangement enables a broadly distributed, coordinated response.

Our findings revealed several features of the DRN^{DAT} circuit which might facilitate a concerted response to novel social and non-social situations. Firstly, we observed dissociable roles for discrete downstream projections – a common motif of valence-encoding neural circuits [29]. Biased recruitment of these 'divergent paths' [29] to the BNST, CeA, and BLP by upstream inputs may serve to fine-tune the balance between social investigation and environmental exploration: facilitating behavioral flexibility with changing environmental conditions or internal state. Secondly, we demonstrate extensive collateralization of DRN^{DAT} neurons In other populations, collateralization is proposed to aid temporal coordination of a multifaceted response: enabling synchronous activation of distributed regions [46,54]. This feature may, therefore, facilitate coordinated recruitment of the BNST and CeA, allowing these regions to work in concert to promote social approach while also maintaining vigilance to salient environmental stimuli. Thirdly, we find precise synaptic organization in the DRN^{DAT} modulation of downstream neuronal activity that allows for qualitatively distinct response profiles of downstream targets. Combined with the spatially-segregated downstream receptor expression pattern, this organization may allow DRN^{DAT} neurons to elicit broad, yet finely-tuned, control over the pattern of neuronal activity, on multiple timescales—perhaps explaining the diverse behavior effects between the BNST- and CeA- projecting DRN^{DAT} populations, despite heavy collateralization.

Although we hypothesized that stimulating DRN^{DAT} inputs to the CeA in group-housed mice would mimic a state similar to that of isolation, we did not observe that the isolation OFF condition produced neural responses more similar to the group-housed ON condition. This suggests two possibilities: 1) that the photostimulation impacted neural activity beyond the endogenous dopamine innervation that may occur with social isolation because it is more potent of a change or 2) that the timing of endogenous dopamine innervation is different and is partially quenched upon exposure to a social agent. To completely understand the temporal dynamics of dopamine signaling with isolation and the firing of DRN^{DAT} neurons upon isolation, further experiments will require exploration of DRN^{DAT} stimulation

parameter space, endogenous neural activity in the DRN^{DAT}-CeA circuit during social isolation, and the effects of DRN^{DAT} stimulation timing.

Separable projections mediate social behavior and valence.

Our data support the hypothesis that separable DRN^{DAT} projections mediate distinct functional roles: a feature which has been previously observed in other neuronal circuits (e.g.[16–20]). The DRN^{DAT} circuit attributes we describe above may further enable this system to modulate other diverse forms of behavior (e.g. arousal [8], fear/reward associations [4,7], and antinociception [5,6]). These could be mediated via other downstream projections and/or via these same projections under different environmental contexts, testing conditions, social histories, and/or internal states. Further work is required to determine how this system is able to exert a broad influence over multiple forms of behavior. Indeed, a recent study examined DRN^{DAT} projection to the nucleus accumbens and its role in promoting sociability[110], suggesting a parallel circuit to that described in the current study. Collectively, however, our data and others support a role for the DRN^{DAT} system in exerting a coordinated behavioral response to novel situations – both social and non-social.

The CeA has been implicated in mediating the response to threats – orchestrating defensive behavioral responses and autonomic changes via efferents to subcortical[37,111,112] and brainstem nuclei [113]. One possible interpretation, therefore, is that DRN^{DAT} input to the CeA suppresses fear-promoting neuronal ensembles in order to facilitate social approach. In the maintenance of social homeostasis, suppression of fear in the presence of social stimuli may represent an adaptive response – preventing salient social stimuli from being interpreted as a threat. Indeed, other need states, such as hunger, are associated with fear suppression and higher-risk behavior [114], suggesting a conserved response to homeostatic imbalance [15]. However, the motivation to attend to social stimuli may also be driven by territorial defense (interacting with social rank), highlighting a need to further understand how internal states can play into the output of this system. A more comprehensive knowledge of the functional cell-types modulated by DRN^{DAT} activity will facilitate our understanding of how this input can shape the downstream neuronal representation of social and non-social stimuli.

In contrast to the CeA, photoactivation of the DRN^{DAT}-BLP projection produced avoidance of the stimulation zone, suggesting an aversive state. This differs from the valence-independent role of VTA dopamine input to the greater BLA complex, wherein dopamine signaling gates synaptic plasticity for associative learning of both positive and negative valence [45] and responds to salient stimuli predicting both positive and negative outcomes [67]. However, DRN and VTA axonal fields differ within the BLA complex, with DRN^{DAT} terminals being more concentrated within the BLP, and VTA^{DAT} inputs traversing the LA, BLA and intercalated cells more densely.

While there have been seemingly contradictory reports on the effect of dopamine on excitability in the BLA[45,63,67], our observations using photostimulation of DRN^{DAT} terminals (in short phasic bursts) are consistent with *in vivo* extracellular recordings combined with electrical stimulation of the midbrain [93]. One unifying hypothesis is that dopamine induces an *indirect* GABA-mediated suppression of pyramidal neurons, which may attenuate their response to weak inputs, while *directly* exciting pyramidal neurons to augment their response to large inputs [90,93]. In this way, amygdala dopamine may underlie a similar role to cortical dopamine [107,115] – enhancing signal-to-noise ratio to facilitate behavioral responses to salient stimuli [107].

Multi-transmitter phenotype of DRN^{DAT} neurons may permit modulation on different timescales.

DRN^{DAT} neurons possess an impressive repertoire of signaling molecules: alongside dopamine and glutamate subsets of DRN^{DAT} neuron express VIP and NPW [81–83]. While there is some partial segregation of VIP- and NPW-expressing neurons [82], our receptor expression analyses suggest that these neuropeptides converge on the same neurons in the BNST and CeA. This co-localization is intriguing, given that *Vipr2* is typically coupled to the excitatory G_s-protein [116], while *Npbwr1* is coupled to the inhibitory G_i-protein [117,118]. Therefore, signaling through these receptors may exert opposing actions on downstream cells. Recruitment of neuropeptidergic signaling pathways may support slower, sustained downstream modulation, for example, in hunger-mediating hypothalamic Agouti-Related Peptide (AgRP) neurons, neuropeptide co-release is essential for sustaining feeding behavior [119]. Therefore, a delayed, persistent neuropeptide-mediated signal might enable downstream modulation to outlive phasic DRN^{DAT} activity: promoting behavioral adjustments over longer timescales.

While the functional role of these neuropeptides remains to be elucidated, studies on knockout mice suggest a role for NPW in social behavior and stress responding [117 83]. Furthermore, in humans with a single-nucleotide polymorphism (SNP) of the *NPBWR1* gene (which impairs receptor function) the perception of fearful/angry faces was more positive and less submissive [120], suggesting a possible role for NPW signaling in interpreting social signals. Similarly, the function of DRN VIP+ neurons has received little attention in rodent models, but there has been more focus on the role of VIP in avian social behavior [121]. Of particular interest, in the rostral arcopallium (a homolog of mammalian amygdala [122]), VIP binding density is elevated in birds during seasonal flocking [123]. This suggests that elevated VIP receptor expression may encourage affiliative social grouping behavior in birds [123]. Thus, NPW and VIP may act in concert with fast glutamate-mediated and slow dopamine-mediated neurotransmission in the central extended amygdala, to modulate behavior on different timescales.

CONCLUSION

Together, these findings reveal that DRN^{DAT} projections exhibit substantial functional specialization, with anatomically distinct pathways modulating different facets of behavior. The DRN^{DAT}-CeA projection promotes sociability, DRN^{DAT}-BLP input drives avoidance, and DRN^{DAT}-BNST enhances vigilant exploration, highlighting the diverse roles of this neural circuit in coordinating adaptive responses to social and environmental contexts. These findings uncover a circuit mechanism through which DRN^{DAT} projections orchestrate distinct behavioral features of a loneliness-like state, providing a framework for understanding how neuromodulatory systems guide complex social and emotional behaviors and suggesting potential targets for therapeutic intervention in affective disorders.

Acknowledgements

K.M.T. is the Wylie Vale Chair at the Salk Institute for Biological Studies, a New York Stem Cell Foundation - Robertson Investigator, and a McKnight Scholar. This work was supported by funding from the JPB Foundation, Alfred P Sloan Foundation, New York Stem Cell Foundation, Klingenstein Foundation, McKnight Foundation, Clayton Foundation, Dolby Family Fund, R01-MH115920 (NIMH), the NIH Director's New Innovator Award DP2-DK102256 (NIDDK), and Pioneer Award DP1-AT009925 (NCCIH). G.A.M was supported by a Postdoctoral Research Fellowship from the Charles A. King Trust. R.L.M. was funded through the MSRP program in the Brains & Cognitive Sciences Department at MIT, supported by the Center for Brains, Minds and Machines (CBMM), and funded by NSF STC award CCF-1231216. E.M.W was supported by a summer scholarship from Johnson & Johnson. We thank C. Leppla, J. Olsen, P. Namburi, V. Barth, J. Wang, K. Batra, A. Brown, and A. Libster for technical advice, all members of the Tye Lab for helpful discussion, and advice from the CellProfiler team at the Broad Institute. We also thank Rachel Neve for the HSV construct, and Charu Ramakrishnan & Karl Deisseroth for AAV_5-fDIO-eYFP.

Author Contributions

K.M.T., G.A.M, and C.R.L. conceptualized the project, designed experiments, supervised experiments and directed data analyses. M.E.L and M.B. performed and analyzed smFISH experiments. G.A.M., M.E.L., C.R.L., C.J., E.M.W., E.P., G.S.P., A.L.-M., and A.P. performed stereotaxic surgeries. G.A.M., C.R.L, E.M.W, E.P, G.S.P, M.E.L., C.J., F.A., A.T., M.B., A.L.-M., R.M., and A.P. ran optogenetic manipulation experiments and analyzed behavioral data. L.R.K. performed Markov model analysis. G.A.M., C.R.L., E.M.W., G.P.S., M.G.C., E.P., G.S.P., A.L.-M., and A.P. performed immunohistochemistry and analyzed images. G.A.M performed *ex vivo* electrophysiology, and N.P.-C., E.Y.K, and R.W. contributed to experimental design and data interpretation. C.R.L performed *in vivo* calcium imaging and analysis. G.A.M., R.W., C.R.L., and L.R.K. reviewed, organized, and prepared the data for data sharing. G.A.M., C.R.L., and K.M.T. wrote the manuscript with review and editing from M.E.L., E.M.W., M.B., R.M., L.R.K., G.P.S., C.J., A.T., F.A., M.G.C., E.P., G.S.P., A.L.-M., A.P., E.Y.K., N.P.-C., and R.W.

1. Yee, J.R., Cavigelli, S.A., Delgado, B., and McClintock, M.K. (2008). Reciprocal Affiliation Among Adolescent Rats During a Mild Group Stressor Predicts Mammary Tumors and Lifespan. Psychosomatic Medicine *70*, 1050. https://doi.org/10.1097/PSY.0b013e31818425fb.

2. Koto, A., Mersch, D., Hollis, B., and Keller, L. (2015). Social isolation causes mortality by disrupting energy homeostasis in ants. Behavioral Ecology and Sociobiology *69*, 583–591.

3. Silk, J.B., Beehner, J.C., Bergman, T.J., Crockford, C., Engh, A.L., Moscovice, L.R., Wittig, R.M., Seyfarth, R.M., and Cheney, D.L. (2010). Strong and Consistent Social Bonds Enhance the Longevity of Female Baboons. Current Biology *20*, 1359–1361. https://doi.org/10.1016/j.cub.2010.05.067.

4. Lin, R., Liang, J., Wang, R., Yan, T., Zhou, Y., Liu, Y., Feng, Q., Sun, F., Li, Y., Li, A., et al. (2020). The Raphe Dopamine System Controls the Expression of Incentive Memory. Neuron *106*, 498-514.e8. https://doi.org/10.1016/j.neuron.2020.02.009.

5. Li, C., Sugam, J.A., Lowery-Gionta, E.G., McElligott, Z.A., McCall, N.M., Lopez, A.J., McKlveen, J.M., Pleil, K.E., and Kash, T.L. (2016). Mu Opioid Receptor Modulation of Dopamine Neurons in the Periaqueductal Gray/Dorsal Raphe: A Role in Regulation of Pain. Neuropsychopharmacology *41*, 2122–2132. https://doi.org/10.1038/npp.2016.12.

6. Meyer, P.J., Morgan, M.M., Kozell, L.B., and Ingram, S.L. (2009). Contribution of dopamine receptors to periaqueductal gray-mediated antinociception. Psychopharmacology (Berl.) *204*, 531–540. https://doi.org/10.1007/s00213-009-1482-y.

7. Groessl, F., Munsch, T., Meis, S., Griessner, J., Kaczanowska, J., Pliota, P., Kargl, D., Badurek, S., Kraitsy, K., Rassoulpour, A., et al. (2018). Dorsal tegmental dopamine neurons gate associative learning of fear. Nature Neuroscience *21*, 952–962. https://doi.org/10.1038/s41593-018-0174-5.

8. Cho, J.R., Treweek, J.B., Robinson, J.E., Xiao, C., Bremner, L.R., Greenbaum, A., and Gradinaru, V. (2017). Dorsal Raphe Dopamine Neurons Modulate Arousal and Promote Wakefulness by Salient Stimuli. Neuron *94*, 1205-1219.e8. https://doi.org/10.1016/j.neuron.2017.05.020.

9. Lu, J., Jhou, T.C., and Saper, C.B. (2006). Identification of wake-active dopaminergic neurons in the ventral periaqueductal gray matter. J. Neurosci. *26*, 193–202. https://doi.org/10.1523/JNEUROSCI.2244-05.2006.

10. Cho, J.R., Chen, X., Kahan, A., Robinson, J.E., Wagenaar, D.A., and Gradinaru, V. (2021). Dorsal Raphe Dopamine Neurons Signal Motivational Salience Dependent on Internal State, Expectation, and Behavioral Context. J. Neurosci. *41*, 2645–2655. https://doi.org/10.1523/JNEUROSCI.2690-20.2021.

11. Matthews, G.A., Nieh, E.H., Vander Weele, C.M., Halbert, S.A., Pradhan, R.V., Yosafat, A.S., Glober, G.F., Izadmehr, E.M., Thomas, R.E., Lacy, G.D., et al. (2016). Dorsal Raphe Dopamine Neurons Represent the Experience of Social Isolation. Cell *164*, 617–631. https://doi.org/10.1016/j.cell.2015.12.040.

12. Tomova, L., Wang, K.L., Thompson, T., Matthews, G.A., Takahashi, A., Tye, K.M., and Saxe, R. (2020). Acute social isolation evokes midbrain craving responses similar to hunger. Nat Neurosci *23*, 1597–1605. https://doi.org/10.1038/s41593-020-00742-z.

13. Hull, C.L. (1943). Principles of Behavior: An Introduction to Behavior Theory (D. Appleton-Century Company, Incorporated).

14. Lee, C.R., Chen, A., and Tye, K.M. (2021). The neural circuitry of social homeostasis: Consequences of acute versus chronic social isolation. Cell *184*, 1500–1516. https://doi.org/10.1016/j.cell.2021.02.028.

15. Matthews, G.A., and Tye, K.M. (2019). Neural mechanisms of social homeostasis. Annals of the New York Academy of Sciences *1457*, 5–25. https://doi.org/10.1111/nyas.14016.

16. Han, W., Tellez, L.A., Rangel, M.J., Motta, S.C., Zhang, X., Perez, I.O., Canteras, N.S., Shammah-Lagnado, S.J., Pol, A.N. van den, and Araujo, I.E. de (2017). Integrated Control of Predatory Hunting by the Central Nucleus of the Amygdala. Cell *168*, 311-324.e18. https://doi.org/10.1016/j.cell.2016.12.027.

17. Kim, S.-Y., Adhikari, A., Lee, S.Y., Marshel, J.H., Kim, C.K., Mallory, C.S., Lo, M., Pak, S., Mattis, J., Lim, B.K., et al. (2013). Diverging neural pathways assemble a behavioural state from separable features in anxiety. Nature *496*, 219–223. https://doi.org/10.1038/nature12018.

18. Kohl, J., Babayan, B.M., Rubinstein, N.D., Autry, A.E., Marin-Rodriguez, B., Kapoor, V., Miyamishi, K., Zweifel, L.S., Luo, L., Uchida, N., et al. (2018). Functional circuit architecture underlying parental behaviour. Nature *556*, 326–331. https://doi.org/10.1038/s41586-018-0027-0.

19. Lammel, S., Ion, D.I., Roeper, J., and Malenka, R.C. (2011). Projection-specific modulation of dopamine neuron synapses by aversive and rewarding stimuli. Neuron *70*, 855–862. https://doi.org/10.1016/j.neuron.2011.03.025.

20. Namburi, P., Beyeler, A., Yorozu, S., Calhoon, G.G., Halbert, S.A., Wichmann, R., Holden, S.S., Mertens, K.L., Anahtar, M., Felix-Ortiz, A.C., et al. (2015). A circuit mechanism for differentiating positive and negative associations. Nature *520*, 675–678. https://doi.org/10.1038/nature14366.

21. Senn, V., Wolff, S.B.E., Herry, C., Grenier, F., Ehrlich, I., Gründemann, J., Fadok, J.P., Müller, C., Letzkus, J.J., and Lüthi, A. (2014). Long-Range Connectivity Defines Behavioral Specificity of Amygdala Neurons. Neuron *81*, 428–437. https://doi.org/10.1016/j.neuron.2013.11.006.

22. Tye, K.M., Prakash, R., Kim, S.-Y., Fenno, L.E., Grosenick, L., Zarabi, H., Thompson, K.R., Gradinaru, V., Ramakrishnan, C., and Deisseroth, K. (2011). Amygdala circuitry mediating reversible and bidirectional control of anxiety. Nature *471*, 358–362. https://doi.org/10.1038/nature09820.

23. Rigotti, M., Barak, O., Warden, M.R., Wang, X.-J., Daw, N.D., Miller, E.K., and Fusi, S. (2013). The importance of mixed selectivity in complex cognitive tasks. Nature *497*, 585–590. https://doi.org/10.1038/nature12160.

24. Tian, J., Huang, R., Cohen, J.Y., Osakada, F., Kobak, D., Machens, C.K., Callaway, E.M., Uchida, N., and Watabe-Uchida, M. (2016). Distributed and Mixed Information in Monosynaptic Inputs to Dopamine Neurons. Neuron *91*, 1374–1389. https://doi.org/10.1016/j.neuron.2016.08.018.

25. Krzywkowski, P., Penna, B., and Gross, C.T. (2020). Dynamic encoding of social threat and spatial context in the hypothalamus. eLife *9*, e57148. https://doi.org/10.7554/eLife.57148.

26. Kyriazi, P., Headley, D.B., and Pare, D. (2018). Multi-dimensional Coding by Basolateral Amygdala Neurons. Neuron *99*, 1315-1328.e5. https://doi.org/10.1016/j.neuron.2018.07.036.

27. Lemos, J.C., Wanat, M.J., Smith, J.S., Reyes, B.A.S., Hollon, N.G., Van Bockstaele, E.J., Chavkin, C., and Phillips, P.E.M. (2012). Severe stress switches CRF action in the nucleus accumbens from appetitive to aversive. Nature *490*, 402–406. https://doi.org/10.1038/nature11436.

28. Seo, C., Guru, A., Jin, M., Ito, B., Sleezer, B.J., Ho, Y.-Y., Wang, E., Boada, C., Krupa, N.A., Kullakanda, D.S., et al. (2019). Intense Threat Switches Dorsal Raphe Serotonin Neurons to a Paradoxical Operational Mode. Science *363*, 538–542. https://doi.org/10.1126/science.aau8722.

29. Tye, K.M. (2018). Neural Circuit Motifs in Valence Processing. Neuron *100*, 436–452. https://doi.org/10.1016/j.neuron.2018.10.001.

30. Lockwood, P.L., Apps, M.A.J., and Chang, S.W.C. (2020). Is There a 'Social' Brain? Implementations and Algorithms. Trends in Cognitive Sciences *24*, 802–813. https://doi.org/10.1016/j.tics.2020.06.011.

31. Bäckman, C.M., Malik, N., Zhang, Y., Shan, L., Grinberg, A., Hoffer, B.J., Westphal, H., and Tomac, A.C. (2006). Characterization of a mouse strain expressing Cre recombinase from the 3' untranslated region of the dopamine transporter locus. Genesis *44*, 383–390. https://doi.org/10.1002/dvg.20228.

32. Cardozo Pinto, D.F., Yang, H., Pollak Dorocic, I., de Jong, J.W., Han, V.J., Peck, J.R., Zhu, Y., Liu, C., Beier, K.T., Smidt, M.P., et al. (2019). Characterization of transgenic mouse models targeting neuromodulatory systems reveals organizational principles of the dorsal raphe. Nature Communications *10*, 4633. https://doi.org/10.1038/s41467-019-12392-2.

33. Lammel, S., Steinberg, E.E., Földy, C., Wall, N.R., Beier, K., Luo, L., and Malenka, R.C. (2015). Diversity of transgenic mouse models for selective targeting of midbrain dopamine neurons. Neuron *85*, 429–438. https://doi.org/10.1016/j.neuron.2014.12.036.

34. Hasue, R.H., and Shammah-Lagnado, S.J. (2002). Origin of the dopaminergic innervation of the central extended amygdala and accumbens shell: a combined retrograde tracing and immunohistochemical study in the rat. J. Comp. Neurol. *454*, 15–33. https://doi.org/10.1002/cne.10420.

35. Meloni, E.G., Gerety, L.P., Knoll, A.T., Cohen, B.M., and Carlezon, W.A. (2006). Behavioral and Anatomical Interactions between Dopamine and Corticotropin-Releasing Factor in the Rat. J. Neurosci. *26*, 3855–3863. https://doi.org/10.1523/JNEUROSCI.4957-05.2006.

36. Oh, S.W., Harris, J.A., Ng, L., Winslow, B., Cain, N., Mihalas, S., Wang, Q., Lau, C., Kuan, L., Henry, A.M., et al. (2014). A mesoscale connectome of the mouse brain. Nature *508*, 207–214. https://doi.org/10.1038/nature13186.

37. Davis, M., Walker, D.L., Miles, L., and Grillon, C. (2010). Phasic vs Sustained Fear in Rats and Humans: Role of the Extended Amygdala in Fear vs Anxiety. Neuropsychopharmacology *35*, 105–135. https://doi.org/10.1038/npp.2009.109.

38. Goode, T.D., and Maren, S. (2017). Role of the bed nucleus of the stria terminalis in aversive learning and memory. Learn. Mem. *24*, 480–491. https://doi.org/10.1101/lm.044206.116.

39. Janak, P.H., and Tye, K.M. (2015). From circuits to behaviour in the amygdala. Nature *517*, 284–292. https://doi.org/10.1038/nature14188.

40. Lebow, M.A., and Chen, A. (2016). Overshadowed by the amygdala: the bed nucleus of the stria terminalis emerges as key to psychiatric disorders. Molecular Psychiatry *21*, 450–463. https://doi.org/10.1038/mp.2016.1.

41. Douglass, A.M., Kucukdereli, H., Ponserre, M., Markovic, M., Gründemann, J., Strobel, C., Alcala Morales, P.L., Conzelmann, K.-K., Lüthi, A., and Klein, R. (2017). Central amygdala circuits modulate food consumption through a positive-valence mechanism. Nature Neuroscience *20*, 1384–1394. https://doi.org/10.1038/nn.4623.

42. Jennings, J.H., Sparta, D.R., Stamatakis, A.M., Ung, R.L., Pleil, K.E., Kash, T.L., and Stuber, G.D. (2013). Distinct extended amygdala circuits for divergent motivational states. Nature *496*, 224–228. https://doi.org/10.1038/nature12041.

43. Kim, J., Zhang, X., Muralidhar, S., LeBlanc, S.A., and Tonegawa, S. (2017). Basolateral to Central Amygdala Neural Circuits for Appetitive Behaviors. Neuron *93*, 1464-1479.e5. https://doi.org/10.1016/j.neuron.2017.02.034.

44. Tye, K.M., Stuber, G.D., De Ridder, B., Bonci, A., and Janak, P.H. (2008). Rapid strengthening of thalamo-amygdala synapses mediates cue–reward learning. Nature *453*, 1253–1257.

45. Tye, K.M., Tye, L.D., Cone, J.J., Hekkelman, E.F., Janak, P.H., and Bonci, A. (2010). Methylphenidate facilitates learning-induced amygdala plasticity. Nature neuroscience *13*, 475–481.

46. Rockland, K.S. (2018). Axon Collaterals and Brain States. Front Syst Neurosci *12*. https://doi.org/10.3389/fnsys.2018.00032.

47. Aransay, A., Rodríguez-López, C., García-Amado, M., Clascá, F., and Prensa, L. (2015). Long-range projection neurons of the mouse ventral tegmental area: a single-cell axon tracing analysis. Front. Neuroanat. *9*. https://doi.org/10.3389/fnana.2015.00059.

48. Beier, K.T., Steinberg, E.E., DeLoach, K.E., Xie, S., Miyamichi, K., Schwarz, L., Gao, X.J., Kremer, E.J., Malenka, R.C., and Luo, L. (2015). Circuit Architecture of VTA Dopamine Neurons Revealed by Systematic Input–Output Mapping. Cell *162*, 622–634. https://doi.org/10.1016/j.cell.2015.07.015.

49. Lerner, T.N., Shilyansky, C., Davidson, T.J., Evans, K.E., Beier, K.T., Zalocusky, K.A., Crow, A.K., Malenka, R.C., Luo, L., Tomer, R., et al. (2015). Intact-Brain Analyses Reveal Distinct Information Carried by SNc Dopamine Subcircuits. Cell *162*, 635–647. https://doi.org/10.1016/j.cell.2015.07.014.

50. Matsuda, W., Furuta, T., Nakamura, K.C., Hioki, H., Fujiyama, F., Arai, R., and Kaneko, T. (2009). Single Nigrostriatal Dopaminergic Neurons Form Widely Spread and Highly Dense Axonal Arborizations in the Neostriatum. J Neurosci *29*, 444–453. https://doi.org/10.1523/JNEUROSCI.4029-08.2009.

51. Moore, R.Y., and Bloom, F.E. (1978). Central catecholamine neuron systems: anatomy and physiology of the dopamine systems. Annual Review of Neuroscience *1*, 129–169. https://doi.org/10.1146/annurev.ne.01.030178.001021.

52. Gagnon, D., and Parent, M. (2014). Distribution of VGLUT3 in Highly Collateralized Axons from the Rat Dorsal Raphe Nucleus as Revealed by Single-Neuron Reconstructions. PLOS ONE *9*, e87709. https://doi.org/10.1371/journal.pone.0087709.

53. van der Kooy, D., and Hattori, T. (1980). Dorsal raphe cells with collateral projections to the caudate-putamen and substantia nigra: a fluorescent retrograde double labeling study in the rat. Brain Research *186*, 1–7. https://doi.org/10.1016/0006-8993(80)90250-4.

54. Waselus, M., Valentino, R.J., and Van Bockstaele, E.J. (2011). Collateralized dorsal raphe nucleus projections: a mechanism for the integration of diverse functions during stress. J. Chem. Neuroanat. *41*, 266–280. https://doi.org/10.1016/j.jchemneu.2011.05.011.

55. Beyeler, A., Chang, C.-J., Silvestre, M., Lévêque, C., Namburi, P., Wildes, C.P., and Tye, K.M. (2018). Organization of Valence-Encoding and Projection-Defined Neurons in the Basolateral Amygdala. Cell Rep *22*, 905–918. https://doi.org/10.1016/j.celrep.2017.12.097.

56. De Bundel, D., Zussy, C., Espallergues, J., Gerfen, C.R., Girault, J.-A., and Valjent, E. (2016). Dopamine D2 receptors gate generalization of conditioned threat responses through mTORC1 signaling in the extended amygdala. Mol Psychiatry *21*, 1545–1553. https://doi.org/10.1038/mp.2015.210.

57. Jo, Y.S., Heymann, G., and Zweifel, L.S. (2018). Dopamine Neurons Reflect the Uncertainty in Fear Generalization. Neuron *100*, 916-925.e3. https://doi.org/10.1016/j.neuron.2018.09.028.

58. Perez de la Mora, M., Gallegos-Cari, A., Crespo-Ramirez, M., Marcellino, D., Hansson, A.C., and Fuxe, K. (2012). Distribution of dopamine D(2)-like receptors in the rat amygdala and their role in the modulation of unconditioned fear and anxiety. Neuroscience *201*, 252–266. https://doi.org/10.1016/j.neuroscience.2011.10.045.

59. Eiler, W.J.A., Seyoum, R., Foster, K.L., Mailey, C., and June, H.L. (2003). D1 dopamine receptor regulates alcohol-motivated behaviors in the bed nucleus of the stria terminalis in alcohol-preferring (P) rats. Synapse *48*, 45–56. https://doi.org/10.1002/syn.10181.

60. Epping-Jordan, M.P., Markou, A., and Koob, G.F. (1998). The dopamine D-1 receptor antagonist SCH 23390 injected into the dorsolateral bed nucleus of the stria terminalis decreased cocaine reinforcement in the rat. Brain Res. *784*, 105–115. https://doi.org/10.1016/s0006-8993(97)01190-6.

61. Rezayof, A., Zarrindast, M.-R., Sahraei, H., and Haeri-Rohani, A.-H.-R. (2002). Involvement of dopamine D2 receptors of the central amygdala on the acquisition and expression of morphine-induced place preference in rat. Pharmacol. Biochem. Behav. *74*, 187–197. https://doi.org/10.1016/s0091-3057(02)00989-9.

62. Thiel, K.J., Wenzel, J.M., Pentkowski, N.S., Hobbs, R.J., Alleweireldt, A.T., and Neisewander, J.L. (2010). Stimulation of dopamine D2/D3 but not D1 receptors in the central amygdala decreases cocaine-seeking behavior. Behav. Brain Res. *214*, 386–394. https://doi.org/10.1016/j.bbr.2010.06.021.

63. Bissière, S., Humeau, Y., and Luthi, A. (2003). Dopamine gates LTP induction in lateral amygdala by suppressing feedforward inhibition. Nature neuroscience *6*, 587–592.

64. Fadok, J.P., Dickerson, T.M.K., and Palmiter, R.D. (2009). Dopamine Is Necessary for Cue-Dependent Fear Conditioning. J Neurosci *29*, 11089–11097. https://doi.org/10.1523/JNEUROSCI.1616-09.2009.

65. Guarraci, F.A., Frohardt, R.J., and Kapp, B.S. (1999). Amygdaloid D1 dopamine receptor involvement in Pavlovian fear conditioning. Brain Res. *827*, 28–40. https://doi.org/10.1016/s0006-8993(99)01291-3.

66. de Oliveira, A.R., Reimer, A.E., de Macedo, C.E.A., de Carvalho, M.C., Silva, M.A. de S., and Brandão, M.L. (2011). Conditioned fear is modulated by D2 receptor pathway connecting the ventral tegmental area and basolateral amygdala. Neurobiol Learn Mem *95*, 37–45. https://doi.org/10.1016/j.nlm.2010.10.005.

67. Lutas, A., Kucukdereli, H., Alturkistani, O., Carty, C., Sugden, A.U., Fernando, K., Diaz, V., Flores-Maldonado, V., and Andermann, M.L. (2019). State-specific gating of salient cues by midbrain dopaminergic input to basal amygdala. Nat Neurosci *22*, 1820–1833. https://doi.org/10.1038/s41593-019-0506-0.

68. Lindzey, G., Winston, H., and Manosevitz, M. (1961). Social Dominance in Inbred Mouse Strains. Nature *191*, 474–476. https://doi.org/10.1038/191474a0.

69. Wang, F., Zhu, J., Zhu, H., Zhang, Q., Lin, Z., and Hu, H. (2011). Bidirectional Control of Social Hierarchy by Synaptic Efficacy in Medial Prefrontal Cortex. Science *334*, 693–697. https://doi.org/10.1126/science.1209951.

70. Zhou, T., Sandi, C., and Hu, H. (2018). Advances in understanding neural mechanisms of social dominance. Curr Opin Neurobiol *49*, 99–107. https://doi.org/10.1016/j.conb.2018.01.006.

71. Cacioppo, S., Bangee, M., Balogh, S., Cardenas-Iniguez, C., Qualter, P., and Cacioppo, J.T. (2016). Loneliness and implicit attention to social threat: A high-performance electrical neuroimaging study. Cogn Neurosci *7*, 138–159. https://doi.org/10.1080/17588928.2015.1070136.

72. Cacioppo, J.T., and Hawkley, L.C. (2009). Perceived Social Isolation and Cognition. Trends Cogn Sci *13*, 447–454. https://doi.org/10.1016/j.tics.2009.06.005.

73. Rodgers, R.J., and Dalvi, A. (1997). Anxiety, defence and the elevated plus-maze. Neuroscience & Biobehavioral Reviews *21*, 801–810. https://doi.org/10.1016/S0149-7634(96)00058-9.

74. Bailey, K.R., and Crawley, J.N. (2009). Anxiety-Related Behaviors in Mice. In Methods of Behavior Analysis in Neuroscience Frontiers in Neuroscience., J. J. Buccafusco, ed. (CRC Press/Taylor & Francis).

75. Lever, C., Burton, S., and O'Keefe, J. (2006). Rearing on hind legs, environmental novelty, and the hippocampal formation. Rev Neurosci *17*, 111–133. https://doi.org/10.1515/revneuro.2006.17.1-2.111.

76. Moy, S.S., Nadler, J.J., Perez, A., Barbaro, R.P., Johns, J.M., Magnuson, T.R., Piven, J., and Crawley, J.N. (2004). Sociability and preference for social novelty in five inbred strains: an approach to assess autistic-like behavior in mice. Genes Brain Behav. *3*, 287–302. https://doi.org/10.1111/j.1601-1848.2004.00076.x.

77. Larrieu, T., Cherix, A., Duque, A., Rodrigues, J., Lei, H., Gruetter, R., and Sandi, C. (2017). Hierarchical Status Predicts Behavioral Vulnerability and Nucleus Accumbens Metabolic Profile Following Chronic Social Defeat Stress. Current Biology *27*, 2202-2210.e4. https://doi.org/10.1016/j.cub.2017.06.027.

78. Füzesi, T., Daviu, N., Wamsteeker Cusulin, J.I., Bonin, R.P., and Bains, J.S. (2016). Hypothalamic CRH neurons orchestrate complex behaviours after stress. Nat Commun *7*, 11937. https://doi.org/10.1038/ncomms11937.

79. Lee, W., Fu, J., Bouwman, N., Farago, P., and Curley, J.P. (2019). Temporal microstructure of dyadic social behavior during relationship formation in mice. PLoS One *14*. https://doi.org/10.1371/journal.pone.0220596.

80. Tejada, J., Bosco, G.G., Morato, S., and Roque, A.C. (2010). Characterization of the rat exploratory behavior in the elevated plus-maze with Markov chains. Journal of Neuroscience Methods *193*, 288–295. https://doi.org/10.1016/j.jneumeth.2010.09.008.

81. Dougalis, A.G., Matthews, G.A.C., Bishop, M.W., Brischoux, F., Kobayashi, K., and Ungless, M.A. (2012). Functional properties of dopamine neurons and co-expression of vasoactive intestinal polypeptide in the dorsal raphe nucleus and ventro-lateral periaqueductal grey. European Journal of Neuroscience *36*, 3322–3332. https://doi.org/10.1111/j.1460-9568.2012.08255.x.

82. Huang, K.W., Ochandarena, N.E., Philson, A.C., Hyun, M., Birnbaum, J.E., Cicconet, M., and Sabatini, B.L. (2019). Molecular and anatomical organization of the dorsal raphe nucleus. eLife *8*, e46464. https://doi.org/10.7554/eLife.46464.

83. Motoike, T., Long, J.M., Tanaka, H., Sinton, C.M., Skach, A., Williams, S.C., Hammer, R.E., Sakurai, T., and Yanagisawa, M. (2016). Mesolimbic neuropeptide W coordinates stress responses under novel environments. Proc Natl Acad Sci U S A *113*, 6023–6028. https://doi.org/10.1073/pnas.1518658113.

84. McCullough, K.M., Daskalakis, N.P., Gafford, G., Morrison, F.G., and Ressler, K.J. (2018). Cell-type-specific interrogation of CeA Drd2 neurons to identify targets for pharmacological modulation of fear extinction. Transl Psychiatry *8*. https://doi.org/10.1038/s41398-018-0190-y.

85. McCullough, K.M., Morrison, F.G., Hartmann, J., Carlezon, W.A., and Ressler, K.J. (2018). Quantified Coexpression Analysis of Central Amygdala Subpopulations. eNeuro *5*. https://doi.org/10.1523/ENEURO.0010-18.2018.

86. Dougalis, A.G., Matthews, G.A.C., Liss, B., and Ungless, M.A. (2017). Ionic currents influencing spontaneous firing and pacemaker frequency in dopamine neurons of the ventrolateral periaqueductal gray and dorsal raphe nucleus (vlPAG/DRN): A voltage-clamp and computational modelling study. J Comput Neurosci *42*, 275–305. https://doi.org/10.1007/s10827-017-0641-0.

87. Poulin, J.-F., Caronia, G., Hofer, C., Cui, Q., Helm, B., Ramakrishnan, C., Chan, C.S., Dombeck, D., Deisseroth, K., and Awatramani, R. (2018). Mapping projections of molecularly defined dopamine neuron subtypes using intersectional genetic approaches. Nat Neurosci *21*, 1260–1271. https://doi.org/10.1038/s41593-018-0203-4.

88. Kash, T.L., Nobis, W.P., Matthews, R.T., and Winder, D.G. (2008). Dopamine Enhances Fast Excitatory Synaptic Transmission in the Extended Amygdala by a CRF-R1-Dependent Process. J. Neurosci. *28*, 13856–13865. https://doi.org/10.1523/JNEUROSCI.4715-08.2008.

89. Krawczyk, M., Georges, F., Sharma, R., Mason, X., Berthet, A., Bézard, E., and Dumont, É.C. (2010). Double-Dissociation of the Catecholaminergic Modulation of Synaptic Transmission in the Oval Bed Nucleus of the Stria Terminalis. Journal of Neurophysiology *105*, 145–153. https://doi.org/10.1152/jn.00710.2010.

90. Kröner, S., Rosenkranz, J.A., Grace, A.A., and Barrionuevo, G. (2005). Dopamine Modulates Excitability of Basolateral Amygdala Neurons In Vitro. Journal of Neurophysiology *93*, 1598–1610. https://doi.org/10.1152/jn.00843.2004.

91. Marowsky, A., Yanagawa, Y., Obata, K., and Vogt, K.E. (2005). A Specialized Subclass of Interneurons Mediates Dopaminergic Facilitation of Amygdala Function. Neuron *48*, 1025–1037. https://doi.org/10.1016/j.neuron.2005.10.029.

92. Naylor, J.C., Li, Q., Kang-Park, M., Wilson, W.A., Kuhn, C., and Moore, S.D. (2010). Dopamine attenuates evoked inhibitory synaptic currents in central amygdala neurons. Eur. J. Neurosci. *32*, 1836–1842. https://doi.org/10.1111/j.1460-9568.2010.07457.x.

93. Rosenkranz, J.A., and Grace, A.A. (1999). Modulation of basolateral amygdala neuronal firing and afferent drive by dopamine receptor activation in vivo. J. Neurosci. *19*, 11027–11039.

94. Rosenkranz, J.A., and Grace, A.A. (2002). Cellular mechanisms of infralimbic and prelimbic prefrontal cortical inhibition and dopaminergic modulation of basolateral amygdala neurons in vivo. J. Neurosci. *22*, 324–337.

95. Silberman, Y., and Winder, D.G. (2013). Corticotropin releasing factor and catecholamines enhance glutamatergic neurotransmission in the lateral subdivision of the central amygdala. Neuropharmacology *70*, 316–323. https://doi.org/10.1016/j.neuropharm.2013.02.014.

96. Beckstead, M.J., Grandy, D.K., Wickman, K., and Williams, J.T. (2004). Vesicular dopamine release elicits an inhibitory postsynaptic current in midbrain dopamine neurons. Neuron *42*, 939–946. https://doi.org/10.1016/j.neuron.2004.05.019.

97. Marcott, P.F., Gong, S., Donthamsetti, P., Grinnell, S.G., Nelson, M.N., Newman, A.H., Birnbaumer, L., Martemyanov, K.A., Javitch, J.A., and Ford, C.P. (2018). Regional heterogeneity of D2-receptor signaling in the dorsal striatum and nucleus accumbens. Neuron *98*, 575-587.e4. https://doi.org/10.1016/j.neuron.2018.03.038.

98. Bettler, B., Kaupmann, K., Mosbacher, J., and Gassmann, M. (2004). Molecular structure and physiological functions of GABA(B) receptors. Physiol Rev *84*, 835–867. https://doi.org/10.1152/physrev.00036.2003.

99. Destexhe, A., and Sejnowski, T.J. (1995). G protein activation kinetics and spillover of gamma-aminobutyric acid may account for differences between inhibitory responses in the hippocampus and thalamus. Proc Natl Acad Sci U S A *92*, 9515–9519.

100. Mackay, J.P., Bompolaki, M., DeJoseph, M.R., Michaelson, S.D., Urban, J.H., and Colmers, W.F. (2019). NPY2 Receptors Reduce Tonic Action Potential-Independent GABAB Currents in the

Basolateral Amygdala. J Neurosci *39*, 4909–4930. https://doi.org/10.1523/JNEUROSCI.2226-18.2019.

101. Cauli, B., Porter, J.T., Tsuzuki, K., Lambolez, B., Rossier, J., Quenet, B., and Audinat, E. (2000). Classification of fusiform neocortical interneurons based on unsupervised clustering. Proc Natl Acad Sci U S A *97*, 6144–6149. https://doi.org/10.1073/pnas.97.11.6144.

102. Guthman, E.M., Garcia, J.D., Ma, M., Chu, P., Baca, S.M., Smith, K.R., Restrepo, D., and Huntsman, M.M. (2020). Cell-type-specific control of basolateral amygdala neuronal circuits via entorhinal cortex-driven feedforward inhibition. eLife. https://doi.org/10.7554/eLife.50601.

103. Hou, W.-H., Kuo, N., Fang, G.-W., Huang, H.-S., Wu, K.-P., Zimmer, A., Cheng, J.-K., and Lien, C.-C. (2016). Wiring Specificity and Synaptic Diversity in the Mouse Lateral Central Amygdala. J. Neurosci. *36*, 4549–4563. https://doi.org/10.1523/JNEUROSCI.3309-15.2016.

104. Chieng, B.C.H., Christie, M.J., and Osborne, P.B. (2006). Characterization of neurons in the rat central nucleus of the amygdala: cellular physiology, morphology, and opioid sensitivity. The Journal of Comparative Neurology *497*, 910–927. https://doi.org/10.1002/cne.21025.

105. Dumont, E.C., Martina, M., Samson, R.D., Drolet, G., and Paré, D. (2002). Physiological properties of central amygdala neurons: species differences. The European Journal of Neuroscience *15*, 545–552. https://doi.org/10.1046/j.0953-816x.2001.01879.x.

106. Lopez de Armentia, M., and Sah, P. (2004). Firing properties and connectivity of neurons in the rat lateral central nucleus of the amygdala. Journal of Neurophysiology *92*, 1285–1294. https://doi.org/10.1152/jn.00211.2004.

107. Vander Weele, C.M., Siciliano, C.A., Matthews, G.A., Namburi, P., Izadmehr, E.M., Espinel, I.C., Nieh, E.H., Schut, E.H.S., Padilla-Coreano, N., Burgos-Robles, A., et al. (2018). Dopamine enhances signal-to-noise ratio in cortical-brainstem encoding of aversive stimuli. Nature *563*, 397. https://doi.org/10.1038/s41586-018-0682-1.

108. Kingsbury, L., Huang, S., Wang, J., Gu, K., Golshani, P., Wu, Y.E., and Hong, W. (2019). Correlated Neural Activity and Encoding of Behavior across Brains of Socially Interacting Animals. Cell *178*, 429-446.e16. https://doi.org/10.1016/j.cell.2019.05.022.

109. Li, Y., Mathis, A., Grewe, B.F., Osterhout, J.A., Ahanonu, B., Schnitzer, M.J., Murthy, V.N., and Dulac, C. (2017). Neuronal Representation of Social Information in the Medial Amygdala of Awake Behaving Mice. Cell *171*, 1176-1190.e17. https://doi.org/10.1016/j.cell.2017.10.015.

110. Choi, J.E., Choi, D.I., Lee, J., Kim, J., Kim, M.J., Hong, I., Jung, H., Sung, Y., Kim, J., Kim, T., et al. (2022). Synaptic ensembles between raphe and D1R-containing accumbens shell neurons underlie postisolation sociability in males. Science Advances *8*, eabo7527. https://doi.org/10.1126/sciadv.abo7527.

111. Fadok, J.P., Markovic, M., Tovote, P., and Lüthi, A. (2018). New perspectives on central amygdala function. Curr Opin Neurobiol *49*, 141–147. https://doi.org/10.1016/j.conb.2018.02.009.

112. Gungor, N.Z., and Paré, D. (2016). Functional Heterogeneity in the Bed Nucleus of the Stria Terminalis. J Neurosci *36*, 8038–8049. https://doi.org/10.1523/JNEUROSCI.0856-16.2016.

113. Tovote, P., Esposito, M.S., Botta, P., Chaudun, F., Fadok, J.P., Markovic, M., Wolff, S.B.E., Ramakrishnan, C., Fenno, L., Deisseroth, K., et al. (2016). Midbrain circuits for defensive behaviour. Nature *534*, 206–212. https://doi.org/10.1038/nature17996.

114. Padilla, S.L., Qiu, J., Soden, M.E., Sanz, E., Nestor, C.C., Barker, F.D., Quintana, A., Zweifel, L.S., Rønnekleiv, O.K., Kelly, M.J., et al. (2016). AgRP Neural Circuits Mediate Adaptive Behaviors in the Starved State. Nat Neurosci *19*, 734–741. https://doi.org/10.1038/nn.4274.

115. Gulledge, A.T., and Jaffe, D.B. (2001). Multiple effects of dopamine on layer V pyramidal cell excitability in rat prefrontal cortex. J Neurophysiol *86*, 586–595. https://doi.org/10.1152/jn.2001.86.2.586.

116. White, C.M., Ji, S., Cai, H., Maudsley, S., and Martin, B. (2010). Therapeutic potential of vasoactive intestinal peptide and its receptors in neurological disorders. CNS & neurological disorders drug targets *9*, 661.

117. Nagata-Kuroiwa, R., Furutani, N., Hara, J., Hondo, M., Ishii, M., Abe, T., Mieda, M., Tsujino, N., Motoike, T., Yanagawa, Y., et al. (2011). Critical Role of Neuropeptides B/W Receptor 1 Signaling in Social Behavior and Fear Memory. PLoS One *6*. https://doi.org/10.1371/journal.pone.0016972.

118. Tanaka, H., Yoshida, T., Miyamoto, N., Motoike, T., Kurosu, H., Shibata, K., Yamanaka, A., Williams, S.C., Richardson, J.A., Tsujino, N., et al. (2003). Characterization of a family of endogenous neuropeptide ligands for the G protein-coupled receptors GPR7 and GPR8. PNAS *100*, 6251–6256. https://doi.org/10.1073/pnas.0837789100.

119. Chen, Y., Essner, R.A., Kosar, S., Miller, O.H., Lin, Y.-C., Mesgarzadeh, S., and Knight, Z.A. (2019). Sustained NPY signaling enables AgRP neurons to drive feeding. Elife *8*. https://doi.org/10.7554/eLife.46348.

120. Watanabe, N., Wada, M., Irukayama-Tomobe, Y., Ogata, Y., Tsujino, N., Suzuki, M., Furutani, N., Sakurai, T., and Yamamoto, M. (2012). A single nucleotide polymorphism of the neuropeptide B/W receptor-1 gene influences the evaluation of facial expressions. PLoS ONE *7*, e35390. https://doi.org/10.1371/journal.pone.0035390.

121. Kingsbury, M.A., and Wilson, L.C. (2016). The Role of VIP in Social Behavior: Neural Hotspots for the Modulation of Affiliation, Aggression, and Parental Care. Integr Comp Biol *56*, 1238–1249. https://doi.org/10.1093/icb/icw122.

122. Reiner, A., Perkel, D.J., Bruce, L.L., Butler, A.B., Csillag, A., Kuenzel, W., Medina, L., Paxinos, G., Shimizu, T., Striedter, G., et al. (2004). Revised nomenclature for avian telencephalon and some related brainstem nuclei. J Comp Neurol *473*, 377–414. https://doi.org/10.1002/cne.20118.

123. Wilson, L.C., Goodson, J.L., and Kingsbury, M.A. (2016). Seasonal Variation in Group Size Is Related to Seasonal Variation in Neuropeptide Receptor Density. BBE *88*, 111–126. https://doi.org/10.1159/000448372.

124. Schindelin, J., Arganda-Carreras, I., Frise, E., Kaynig, V., Longair, M., Pietzsch, T., Preibisch, S., Rueden, C., Saalfeld, S., Schmid, B., et al. (2012). Fiji: an open-source platform for biological-image analysis. Nature Methods *9*, 676–682. https://doi.org/10.1038/nmeth.2019.

125. McQuin, C., Goodman, A., Chernyshev, V., Kamentsky, L., Cimini, B.A., Karhohs, K.W., Doan, M., Ding, L., Rafelski, S.M., Thirstrup, D., et al. (2018). CellProfiler 3.0: Next-generation image processing for biology. PLOS Biology *16*, e2005970. https://doi.org/10.1371/journal.pbio.2005970.

126. Paxinos, G., and Franklin, K.B.J. (2004). The mouse brain in stereotaxic coordinates 2nd ed.,Compact ed. (Academic).

127. Paxinos, G., and Franklin, K.B.J. (2019). Paxinos and Franklin's The mouse brain in stereotaxic coordinates Fifth edition. (Academic Press, an imprint of Elsevier).

128. Bogovic, J.A., Hanslovsky, P., Wong, A., and Saalfeld, S. (2016). Robust Registration of Calcium Images by Learned Contrast Synthesis. 2016 IEEE 13th International Symposium on Biomedical Imaging (ISBI), 1123–1126. https://doi.org/10.1109/ISBI.2016.7493463.

129. Conte, W.L., Kamishina, H., and Reep, R.L. (2009). Multiple neuroanatomical tract-tracing using fluorescent Alexa Fluor conjugates of cholera toxin subunit B in rats. Nat Protoc *4*, 1157–1166. https://doi.org/10.1038/nprot.2009.93.

130. Hunter, J.D. (2007). Matplotlib: A 2D Graphics Environment. Computing in Science Engineering *9*, 90–95. https://doi.org/10.1109/MCSE.2007.55.

131. Pedregosa, F., Varoquaux, G., Gramfort, A., Michel, V., Thirion, B., Grisel, O., Blondel, M., Prettenhofer, P., Weiss, R., Dubourg, V., et al. (2011). Scikit-learn: Machine Learning in Python. J. Mach. Learn. Res. *12*, 2825–2830.

132. Gottman, J.M., and Roy, A.K. (1990). Sequential Analysis: A Guide for Behavioral Researchers (Cambridge University Press).

133. Novák, P., and Zahradník, I. (2006). Q-Method for High-Resolution, Whole-Cell Patch-Clamp Impedance Measurements Using Square Wave Stimulation. Ann Biomed Eng *34*, 1201–1212. https://doi.org/10.1007/s10439-006-9140-6.

134. Virtanen, P., Gommers, R., Oliphant, T.E., Haberland, M., Reddy, T., Cournapeau, D., Burovski, E., Peterson, P., Weckesser, W., Bright, J., et al. (2020). SciPy 1.0: fundamental algorithms for scientific computing in Python. Nature Methods *17*, 261–272. https://doi.org/10.1038/s41592-019-0686-2.

135. Ward, J.H. (1963). Hierarchical Grouping to Optimize an Objective Function. null *58*, 236–244. https://doi.org/10.1080/01621459.1963.10500845.

136. Michael Waskom, Olga Botvinnik, Maoz Gelbart, Joel Ostblom, Paul Hobson, Saulius Lukauskas, David C Gemperline, Tom Augspurger, Yaroslav Halchenko, Jordi Warmenhoven, et al. (2020). mwaskom/seaborn: v0.11.0 (Sepetmber 2020) (Zenodo) https://doi.org/10.5281/zenodo.4019146.

137. Stamatakis, A.M., Schachter, M.J., Gulati, S., Zitelli, K.T., Malanowski, S., Tajik, A., Fritz, C., Trulson, M., and Otte, S.L. (2018). Simultaneous Optogenetics and Cellular Resolution Calcium Imaging During Active Behavior Using a Miniaturized Microscope. Front. Neurosci. *12*. https://doi.org/10.3389/fnins.2018.00496.

138. Pereira, T.D., Tabris, N., Matsliah, A., Turner, D.M., Li, J., Ravindranath, S., Papadoyannis, E.S., Normand, E., Deutsch, D.S., Wang, Z.Y., et al. (2022). SLEAP: A deep learning system for multi-animal pose tracking. Nat Methods *19*, 486–495. https://doi.org/10.1038/s41592-022-01426-1.

139. Pnevmatikakis, E.A., and Giovannucci, A. (2017). NoRMCorre: An online algorithm for piecewise rigid motion correction of calcium imaging data. J Neurosci Methods *291*, 83–94. https://doi.org/10.1016/j.jneumeth.2017.07.031.

140. Zhou, P., Resendez, S.L., Rodriguez-Romaguera, J., Jimenez, J.C., Neufeld, S.Q., Giovannucci, A., Friedrich, J., Pnevmatikakis, E.A., Stuber, G.D., Hen, R., et al. (2018). Efficient and accurate extraction of in vivo calcium signals from microendoscopic video data. eLife *7*, e28728. https://doi.org/10.7554/eLife.28728.

141. Sheintuch, L., Rubin, A., Brande-Eilat, N., Geva, N., Sadeh, N., Pinchasof, O., and Ziv, Y. (2017). Tracking the Same Neurons across Multiple Days in Ca2+ Imaging Data. Cell Rep *21*, 1102–1115. https://doi.org/10.1016/j.celrep.2017.10.013.

Methods

Animals and housing

All procedures involving animals were conducted in accordance with NIH guidelines and approved by the MIT Committee on Animal Care or the Salk Institute Institutional Animal Care and Use Committee. DAT::IRES-Cre (B6.SJL-Slc6a3$^{tm1.1(cre)Bkmn}$/J) [31] were purchased from the Jackson Laboratory (stock no. 006660; the Jackson Laboratory, ME, USA) and bred in-house to generate heterozygous male offspring for experiments. Wild-type C57BL/6J male mice were purchased from Charles River Laboratories (MA, USA). Mice were housed on a 12h:12h reverse light dark cycle (MIT: lights off 9am-9pm; Salk Institute: lights off 9.30am-9.30pm) with food and water available *ad libitum*. Mice were housed in groups of 2-4 with same-sex siblings. For photoinhibition and CeA calcium imaging experiments, mice were additionally tested following 24 hours of social isolation. Only mice with acceptable histological placements were included in final datasets.

Surgery and viral constructs

Mice (>7 weeks of age) were anaesthetized with isoflurane (inhalation: 4% for induction, ~2% for maintenance, oxygen flow rate 1 L/min) before being placed in a digital small animal stereotax (David Kopf Instruments, CA, USA). Surgeries were performed under aseptic conditions with body temperature maintained by a heating pad throughout. Injections of recombinant adeno-associated viral (AAV) vectors, herpes simplex virus (HSV), or cholera toxin subunit-B (CTB) were performed using a beveled 33 gauge microinjection needle with a 10 µL microsyringe (Nanofil; WPI, FL, USA). Virus or CTB was delivered at a rate of 0.1 µL/min using a microsyringe pump (UMP3; WPI, FL, USA) connected to a Micro4 controller (WPI, FL, USA). Following injection, the needle was maintained in place for ~2 min, then raised up by 0.05 mm and held for ~10 min (to permit diffusion from the injection site) before being slowly withdrawn. Skull measurements were made relative to Bregma for all injections and implants. Implants were secured to the skull by a layer of adhesive cement (C&B Metabond; Parkell Inc., NY, USA) followed by a layer of black cranioplastic cement (Ortho-Jet; Lang, IL, USA). Mice were given pre-emptive analgesia (1 mg/kg buprenorphine slow-release; sub-cutaneous; delivered concurrent with warmed Ringer's solution to prevent dehydration), supplemented with meloxicam (1.5 mg/kg; sub-cutaneous) where necessary, and were monitored on a heating pad until recovery from anesthesia.

AAV_5-EF1α-DIO-ChR2-eYFP, AAV_5-EF1α-DIO-eYFP, AAV_5-EF1 α -fDIO-eYFP , and AAV_8-Syn-ChrimsonR-tdTomato were packaged by the University of North Carolina Vector Core (NC, USA) and received the AAV_5-EF1a-fDIO-eYFP construct from Karl Deisseroth and Charu Ramakrishnan. HSV-LS1L-mCherry-IRES-flpo was packaged by Dr. Rachael Neve at the Viral Gene Transfer Core Facility at MIT (now located at Massachusetts General Hospital). AAV_5-EF1α-DIO-eNpHR3.0-eYFP and AAV_1-syn-jGCaMP7f was packaged by Addgene (MA, USA), and AAV_1-CAG-TdTomato was packaged by the UPenn vector core (PA, USA).

Immunohistochemistry and confocal microscopy

Mice were deeply anaesthetized with sodium pentobarbital (200 mg/kg, intraperitoneal; IP) or euthasol (150 mg/kg; IP) followed by transcardial perfusion with 10 mL ice-cold Ringer's solution and 15 mL ice-cold 4% paraformaldehyde (PFA). The brain was carefully dissected from the cranial cavity and immersed in 4% PFA for ~6-18 h before transfer to 30% sucrose solution in phosphate-buffered saline (PBS) at 4°C. After at least 48 hr, brains were sectioned at 40 µm on a freezing sliding microtome

(HM430; Thermo Fisher Scientific, MA, USA) and sections stored at 4°C in 1X PBS. For immunohistochemistry, sections were blocked in PBS containing 0.3% Triton X-100 (PBS-T; Sigma-Aldrich, MO, USA) with 3% normal donkey serum (NDS; Jackson Immunoresearch, PA, USA) for 30-60 min at room temperature. This was followed by incubation in primary antibody solution chicken anti-TH (1:1000; AB9702; EMD Millipore, MA, USA) in 0.3% PBS-T with 3% NDS) overnight at 4°C. Sections were then washed in 1X PBS four times (10 min each) before incubation in secondary antibody solution containing donkey anti-chicken 488 or 647 (1:1000; Jackson Immunoresearch, PA, USA) and a DNA-specific fluorescent probe (DAPI; 1:50000; Invitrogen, Thermo Fisher Scientific, MA, USA) in 0.2% PBS-T with 3% NDS for 1.5-2 hr at room temperature. Sections were again washed four times in 1X PBS (10 min each) before being mounted on glass slides and coverslipped using warmed PVA-DABCO (Sigma-Aldrich, MO, USA).

Images were captured on a laser scanning confocal microscope (Olympus FV1000, Olympus, PA, USA) using Fluoview software version 4.0 (Olympus, PA, USA). Images were collected through a 10X/0.40 NA objective for injection site and optic fiber placement verification, a 20X/0.75 objective for terminal fluoresence quantification, and an oil-immersion 40X/1.30 NA objective for neurobiotin-filled neurons and RNAscope analysis (see individual Methods sections for more detail). FIJI [124], CellProfiler 3.1 (Broad Institute, MA, USA)[125], and Adobe Photoshop CC (Adobe Systems Incorporated, CA, USA) were used for subsequent image processing and analysis.

Downstream fluorescence quantification

In DAT::Cre mice, AAV_5-EF1α-DIO-ChR2-eYFP (300 nL) was injected into the DRN (ML:1.20, AP:-4.10, DV:-2.90; needle at a 20° angle from the midline, bevel facing medial) or VTA (ML:0.85, AP:-2.70, DV:-4.50), and after 8 weeks mice underwent perfusion-fixation. Brains were subsequently sectioned at 40 µm, processed with immunohistochemistry for TH and DAPI, and serial z-stack images (3 µm optical thickness) collected at 20X on a confocal microscope. (See *'Immunohistochemistry and confocal microscopy'* section above for details). A maximum projection was generated in FIJI and background subtraction based on the 'rolling ball' algorithm (radius = 50 pixels) was applied to correct for uneven illumination. The appropriate brain atlas slice [126,127] was overlaid onto the fluorescent image using the BigWarp plugin (https://imagej.net/BigWarp) [128] in FIJI, by designating major anatomical landmarks based on DAPI staining and TH expression. Regions of interest (ROIs) were then annotated from the overlaid atlas, and mean fluorescence within each ROI quantified using FIJI. The PFC was examined from AP: 2.22 to 1.34, the striatum from AP 1.70 to 0.74, the BNST from AP 0.37 to -0.11, the CeA from AP -0.82 to -1.94, and the amygdala from AP -0.82 to -2.92. Average images in Figure 1D, 5A, 5E, and 5I were created by aligning individual images (from the middle AP region of the BNST, CeA, or BLP), using the line ROI registration plugin (https://imagej.net/Align_Image_by_line_ROI) in FIJI. An average projection was then performed across all images and the 'royal' LUT applied to visualize relative fluorescence intensity.

Retrograde tracing and intersectional viral expression

C57BL/6 mice were injected with 150-250 nL CTB conjugated to Alexa Fluor-555 (CTB-555) or Alexa Fluor-647 (CTB-647; Molecular Probes, OR, USA [129]) in two of three locations: the BNST (ML:1.10, AP:0.50, DV: -4.30; needle bevel facing back), CeA (ML:2.85, AP: -1.20; DV:-4.75; needle bevel facing back), or BLP (ML:3.35, AP:-2.20, DV:-5.25; needle bevel facing back). To assess retrograde CTB co-

expression following injection of both fluorophore-conjugates of CTB into the same region (Figure 1—figure supplement 2A-C), injections were either performed sequentially, or CTB-555 and CTB-647 were mixed prior to a single injection. After 7 days to allow for retrograde transport, mice were deeply anaesthetized with sodium pentobarbital (200 mg/kg) and perfused-fixed for subsequent histology. Brain sections containing injection sites and the DRN were prepared at 40 µm and processed with immunohistochemistry for TH and DAPI. (See *'Immunohistochemistry and confocal microscopy'* section above for details). CTB injection sites were verified with images acquired on a confocal microscope through a 10X objective (serial z-stack with 5 µm optical thickness) and images of the DRN were acquired through a 40X objective (serial z-stack with 3 µm optical thickness). DRN cells co-expressing CTB and TH were counted manually using the ROI 'point' tool in Fluoview software version 4.0 (Olympus, PA, USA). Counted files were imported into FIJI, and images overlaid onto the appropriate brain atlas image of the DRN using the BigWarp plugin (https://imagej.net/BigWarp)[128]. The x-y coordinates of counted/marked CTB+/TH+ cells were extracted using the 'Measure' function in FIJI. These coordinates were then used to generate heatmaps of cell location (Figure 1—figure supplement 2D-E) by creating a 2D histogram using the Matplotlib package [130] in Python .

Intersectional labelling of the dopaminergic projection from the DRN to the CeA was achieved by injecting HSV-LS1L-mCherry-IRES-flpo (300 nL) into the CeA (ML:2.85, AP:-1.45, DV:-4.55; needle bevel facing medial) and AAV_5-fDIO-eYFP (300 nL) into the DRN (ML:1.20, AP:-4.10, DV:-2.90; needle at a 20° angle from the midline, bevel facing medial) of a DAT::Cre mouse. After 8 weeks, mice were perfused-fixed with 4% PFA, and the brain sectioned on a freezing microtome at 40 µm before immunohistochemical processing with TH and DAPI. Images of eYFP-expressing cells in the DRN and terminals in the CeA and BNST were captured on a confocal microscope through a 20X objective with a serial z-section thickness of 3 µm.

Behavioral assays and optogenetic manipulations

DAT::Cre mice were injected with 300 nL AAV_5- EF1α-DIO-ChR2-eYFP or AAV_5-EF1α-DIO-eYFP in the DRN (ML:1.20; AP:-4.10; DV:-2.90; needle at a 20° angle from the right side, bevel facing medial) and optic fibers (300 µm core, NA=0.37; Thorlabs, NJ, USA), held within a stainless steel ferrule (Precision Fiber Products, CA, USA), were implanted unilaterally or bilaterally over the BNST (unilateral: ML:1.10, AP:0.40, DV:-3.50; bilateral: ML:1.65, AP:0.40, DV:-3.35; 10° angle from midline), CeA (ML:2.85, AP:-1.35, DV:-4.00), or BLP (ML:3.30, AP:-2.20, DV:-4.30). Behavioral experiments commenced 7-8 weeks following surgery. Mice were handled and habituated to patch cable connection once per day for at least 3 days before beginning optical manipulations. Behavioral testing was performed in dimly-lit soundproofed room during the mice's active dark phase (~10am-5pm). On each testing day, mice were given at least 1 hr to acclimate to the testing room before experiments began. For optical manipulations, optic fiber implants were connected to a patch cable via a ceramic sleeve (Precision Fiber Products, CA, USA), which itself was connected to a commutator (rotary joint; Doric, Québec, Canada) using an FC/PC adapter, to permit uninhibited movement. The commutator, in turn, was connected via a second patch cable (with FC/PC connectors) to a 473 nm diode-pumped solid state (DPSS) laser (OEM Laser Systems, UT, USA). To control the output of the laser, a Master-8 pulse stimulator (AMPI, Israel) was used, and the light power set to 10 mW.

Tube test: Cages of mice (same-sex groups of 2-4) were assayed for social dominance using the tube test [68,69]. Mice were individually trained to pass through a clear Plexiglas tube (30 cm length, 3.2 cm inner diameter) over 4 days. Each training trial involved releasing the mouse into the tube from one end,

and ensuring it traveled through and out the other side. Mice which attempted to reverse, or were reluctant to exit at the other end of the tube, were gently encouraged forwards by light pressure from a plastic stick pressing on their hind region. Between trials mice freely explored the open arena outside tube (76 x 60 cm) for ~30-60 s. Mice performed 8 training trials (4 from each end) on days 1 and 2, and 3 trials (alternating ends) on days 3 and 4. On days 5-8 mice competed against cagemates in a round-robin design. For each contest, mice were released simultaneously into opposite ends of the tube so that they met face-to-face in the center of the tube. The mouse which retreated from the confrontation was designated as the 'loser' and his opponent designated the 'winner'. Across testing days, the side from which animals were released and the order in which they were tested against cagemates was counterbalanced. An animal's 'relative dominance' score reflected their proportion of 'wins' across all contests from 3-4 days of testing.

Open field test (OFT): The open field was composed of a square arena (51 x 51 cm) made of transparent Plexiglas with 25 cm high walls. Mice freely explored the arena for 15 min, and blue light (8 pulses with 5 ms pulse-width, at 30 Hz, every 5 s) was delivered during the middle 5 min epoch of the session. Animals were recorded using a video camera positioned above the arena, and Ethovision XT software used to track mouse location (Noldus, Netherlands). To assess anxiety-related behavior, for analysis, the chamber was divided into a 'center' square region and a 'periphery', with equal area.

Three chamber sociability assay: The apparatus consisted of a 57.5l x 22.5w x 16.5h cm chamber, with transparent Plexiglas walls and opaque grey plastic floors. The chamber was divided into unmarked left and right compartments (each 23 x 22.5 cm) and a smaller center compartment (11.5 x 22.5 cm). An upturned wire mesh cup was placed in the left and right compartments. Each mouse first underwent a habituation session (10 min) where they freely explored the chamber. They were then briefly (~1 min) confined to the center compartment by the insertion of clear Plexiglas walls, while a novel object was placed under one of the two upturned cups, and a juvenile C57BL/6 mouse (3.5-5 weeks of age) was placed under the other upturned cup. The mice were then allowed to freely explore the chamber for a further 10 min. The task was repeated on the second day, with the chamber rotated by 90˚ relative to external spatial cues, and with a different novel object and novel juvenile mouse. The 10 min test epoch was paired with blue light delivery (8 pulses with 5 ms pulse-width, at 30 Hz, every 5 s) on one of the two days, counterbalanced across animals. Mice were excluded if they showed a strong preference (>70% time spent) for one side of the chamber in the habituation phase, or if they spent more than 1 min on top of the upturned cups during any session. For photoinhibition experiments, the protocol was exactly the same as the ChR2 experiment, except the 10 min test epoch was paired with constant yellow light (589nm) delivery for one day in the 'group-housed' and also during the additional 'isolated' condition. Animals were recorded using a video camera positioned above the chamber and movement tracked using Ethovision XT (Noldus, Netherlands). The social:object ratio reflected the time spent in the 'social' side of the chamber (containing a novel juvenile mouse) divided by the time spent in the 'object' side of the chamber (containing a novel object).

Juvenile intruder assay: Mice were tested individually in their home cage. They freely explored alone for 5 min after which a novel juvenile mouse was placed in the cage for a further 3 min. The task was repeated on the second day with a different novel juvenile mouse. One of the two sessions was paired with blue light delivery (8 pulses with 5 ms pulse-width, at 30 Hz, every 5 s) which commenced after 2 min and continued until the end of the task (6 min total). The behavior of the mouse during the 3 min with the juvenile was scored manually using ODLog software (Macropod Software, Australia). Video

files were scored twice (by two different observers, blinded to the experimental conditions) and the average of their counts was used for analysis. (See also *'First order Markov analysis'* section).

Elevated plus maze (EPM): The EPM was made of grey plastic and consisted of two closed arms (30l x 5w x 30h cm) and two open arms (30l x 5w cm), radiating at 90˚ from a central platform (5 x 5 cm) and raised from the ground by 75 cm. Mice freely explored for 15 min, with blue light (8 pulses with 5 ms pulse-width, at 30 Hz, every 5 s) delivered during the middle 5 min epoch of the session. A video camera position above the EPM was used to record animals, and movement was tracked using Ethovision XT (Noldus, Netherlands).

Real-time place preference (RTPP): Mice were placed in a 52l x 52w x 26.5h cm transparent Plexiglas chamber, with clear panels separating left and right sides to leave a 11.5 cm gap for mice to pass through. Mice freely explored for 30 min, during which entry into one side of the chamber resulted in delivery of blue light (15 pulses with 5 ms pulse-width, at 30 Hz, every 5 s), which continued until mice exited the zone. Entry into the opposite side did not result in blue light delivery. The side paired with blue light delivery was counterbalanced across animals. A video camera positioned above the arena recorded animals, and mouse movement was tracked using Ethovision XT (Noldus, Netherlands).

Intra-cranial self-stimulation (ICSS): Mice were food deprived for 16-20 hr prior to each day of ICSS, in order to encourage behavioral responding. Testing was conducted in an operant chamber (Med Associates, VT, USA) within a custom sound-attenuating outer box. The operant chamber contained two illuminated nose-poke ports, each with an infrared beam, and a cue light positioned above each port. White noise was delivered continuously throughout the session, and successful nose-pokes (signaled by a beam break) resulted in an auditory tone (1 s duration, 1 or 1.5 kHz) and illumination of the respective cue light. A nose-poke at the 'active' port also triggered delivery of blue light (90 pulses with 5 ms pulse-width, at 30 Hz) while a nose-poke at the 'inactive' port did not trigger light delivery. The physical location of the active and inactive nose-poke ports, and the auditory tone frequency associated with each port, was counterbalanced across animals. On day 1 (training), mice completed a 2 hr session in the operant chamber in which both nose-poke ports were baited with a small amount of palatable food, in order to encourage investigation. On day 2 (testing), mice completed an identical 2 hr session, except the nose-poke ports were not baited. Nose-poke activity was recorded with MedPC software (Med Associates, VT, USA) and subject-averaged cumulative distribution plots were generated using MATLAB (Mathworks, MA, USA). Only data from day 2 was used for analysis.

Analysis of baseline behavior: The baseline behavior of all mice (i.e without stimulation) was evaluated to uncover any relationships between specific types of behavior assessed in different tasks. These analyses used relative dominance from the tube test, the first 5 min of the OFT and EPM, and the OFF trial from the three-chamber sociability and juvenile intruder assays. Correlation matrices were generated in GraphPad Prism 8 (GraphPad Software, CA, USA) to show the Pearson's correlation coefficient for each pair of variables.

Dimensionality reduction was performed on baseline behavior data using principal component analysis (PCA) with the scikit-learn module [131] in Python. The eight input measures from behavioral assays were (1) percent time moving in the OFT, (2) time in the center of the OFT, (3) time in the open arms of the EPM, (4) social:object ratio in the three chamber assay, and (5) time spent face sniffing, (6) anogenital sniffing, (7) rearing, and (8) grooming in the juvenile intruder assay. The data was first normalized to generate a covariance matrix and then the first 5 PCs were extracted. Relative dominance

was concatenated with the resulting PC values for each mouse to color-code individual points in the PC1 vs PC2 plot.

First order Markov analysis: Behavioral videos from the juvenile intruder assay were manually annotated so that each second of the 180 s session was assigned a code(s) from 15 behavioral categories:

- Social behaviors: face sniff (reciprocated), face sniff (non-reciprocated), flank sniff, anogenital sniff (reciprocated), anogenital sniff (non-reciprocated), close follow, approach, dominant climb, attack.
- Nonsocial behaviors: groom, dig, rear, climb, still, ambulate.

We designed a 2-state Markov model, in which behaviors were assigned to either the 'social' or 'nonsocial' categories. For each animal, we created a transition probability matrix from each sequence by counting the number of transitions that occurred and dividing by the total number of occurrences of that behavior. To compute the overall transition probability matrix for the eYFP and ChR2 groups, we took the mean of the transition probability across all individuals in that group. Difference scores between the stimulation OFF and ON sessions were calculated by taking the difference across pairs of transition probability matrices corresponding to each individual, then calculating the mean across eYFP or ChR2-expressing mice.

To verify that a first order Markov model was an appropriate fit for our data we computed the log likelihood chi squared statistic [132]:

$$G = 2\sum_{j}\sum_{i} O_{ij} \ln \frac{O_{ij}}{E_{ij}},$$

where $O_{ij} \geq 0$ is the observed number of transitions from state i to j, $E_{ij} \geq 0$ is the expected number of transitions from state i to state j assuming a zeroth order Markov (i.e., no time dependence). We found that G was statistically significant for all subjects in both the 15 state and 2 state models, thus rejecting the null hypothesis of randomly transitioning between states.

We also tested whether a non-stationary model was a better fit for the data than a stationary model. To do this, we divided each subject's behavioral sequence into two segments of equal duration and computed transition probability matrices for each segment. We then computed a variation on the likelihood ratio chi square statistic [132]:

$$LRX = 2\sum_{s}\sum_{j}\sum_{i} f_{ijs} \ln \frac{\bar{p}_{ijs}}{p_{ij}},$$

where *s* represents the segment, p_{ij} is the probability of transition from state *i* to *j* taken over the entire sequence, $\bar{p}_{ijs}$ is the probability of transition from *i* to *j* for each segment, and f_{ijs} is the number of transitions from state *i* to *j* for each segment. Since not all subjects had a significant difference, we determined that a stationary model was the most appropriate model to fit all our data.

Ex vivo electrophysiology

DAT::Cre mice received an injection of 300 nL AAV_5-DIO-ChR2-eYFP or AAV_9-FLEX-ChrimsonR-TdTomato in the DRN (ML:1.20, AP:-4.10, DV:-2.90; needle at a 20° angle from the midline, bevel facing medial), and after at least 8 weeks for transgene expression, mice were deeply anaesthetized with sodium pentobarbital (200 mg/kg) or euthasol (150 mg/kg; IP). They were then transcardially perfused with ice-cold (~4°C) modified artificial cerebrospinal fluid (ACSF; composition in mM: NaCl 87, KCl 2.5, NaH2PO4*H20 1.3, MgCl2*6H2O 7, NaHCO3 25, sucrose 75, ascorbate 5, CaCl2*2H2O 0.5, in ddH20; osmolarity 320-330 mOsm, pH 7.30-7.40), saturated with carbogen gas (95% oxygen, 5% carbon dioxide) before the brain was rapidly and carefully extracted from the cranial cavity. Thick coronal (300 µm) slices containing the BNST, CeA, BLP, and DRN were prepared on a vibrating blade vibratome (VT1200; Leica Biosystems, Germany), in ice-cold modified ACSF saturated with carbogen gas. Brain slices were hemisected with a scalpel blade before transfer to a holding chamber containing ACSF (composition in mM: NaCl 126, KCl 2.5, NaH2PO4*H20 1.25, MgCl2*6H2O 1, NaHCO3 26, glucose 10, CaCl2*H2O 2.4; osmolarity 298-302 mOsm, pH 7.30-7.40) saturated with carbogen, in a warm water bath (~30°C).

Electrophysiological recordings were commenced after the slices had rested for at least 45 min. During recording, the brain slice was maintained in a bath with continuously perfused ACSF, saturated with carbogen, at 31±1°C using a peristaltic pump (Minipuls3; Gilson, WI, USA). Slices were visualized through an upright microscope (Scientifica, UK) equipped with infrared-differential interference contrast (IR-DIC) optics and a Q-imaging Retiga Exi camera (Q Imaging, Canada). In the BNST, CeA, and BLP, recordings were performed in the region containing fluorescent DRN^{DAT} terminals (expressing ChR2-eYFP or Chrimson-TdTomato) with neurons visualized through a 40X/0.80 NA water immersion objective. Terminal expression was confirmed by brief illumination from a 470 nm LED light source (pE-100; CoolLED, NY, USA) for ChR2-eYFP, or a metal halide lamp (Lumen 200; Prior Scientific Inc., UK), for ChrimsonR-TdTomato, combined with the appropriate filter set. Borosilicate glass capillaries were shaped on a P-97 puller (Sutter Instrument, CA, USA) to produce pipettes for recording that had resistance values of 3.5-5 MOhm when filled with internal solution (composition in mM: potassium gluconate 125, NaCl 10, HEPES 20, MgATP 3, and 0.1% neurobiotin, in ddH20 (osmolarity 287 mOsm; pH 7.3). Whole-cell patch-clamp recordings were made using pClamp 10.4 software (Molecular Devices, CA, USA), with analog signals amplified using a Multiclamp 700B amplifier, filtered at 3 kHz, and digitized at 10 kHz using a Digidata 1550 (Molecular Devices, CA, USA). A 5 mV, 250 ms hyperpolarizing step was used to monitor cell health throughout the experiment, and recordings were terminated if significant changes (>20%) occurred to series resistance (R_s), input resistance (R_{in}), or holding current.

Passive cell properties (capacitance, membrane resistance) were estimated from the current response to hyperpolarizing 5 mV, 250 ms steps, delivered in voltage-clamp from a holding potential of -70 mV, using custom MATLAB code written by Praneeth Namburi, based on MATLAB implementation of the Q-Method[133]. To examine the membrane potential response to current injection, cells were recorded in current-clamp mode, and a series of 1 s steps were delivered, in 20 pA increments, from -120 pA to 260 pA. The voltage sag amplitude (attributable to the hyperpolarization-activated cation current; I_h) was measured as the difference between the peak instantaneous and steady-state membrane potential elicited during a -120 pA step (see Figure 6L). The ramp ratio was calculated by dividing the average membrane potential between 900-1000 ms by the membrane potential between 100-200 ms following step onset, using the largest current step that elicited a subthreshold response (i.e. did not evoke action potentials). The firing delay was taken as the time between current step onset and the first elicited action

potential, on delivery of the first current step that was elicited a suprathreshold response (i.e. rheobase current). The max instantaneous firing frequency (max freq.$_{inst}$) was taken as the maximum firing frequency attained during the first 100 ms of the depolarizing current steps.

To photostimulate ChR2-expressing DRN^{DAT} terminals in the BNST, CeA, and BLP, 470 nm light was delivered through the 40X/0.8 NA objective from an LED light source (pE-100; CoolLED, NY, USA). Neurons were recorded at their resting membrane potential in current-clamp mode, and 470 nm light (8 pulses at 30 Hz, 5ms pulse-width) was delivered every 30 s. In a minority of cells which showed spontaneous activity at the resting potential, negative current was injected to hold the cell at a subthreshold potential (typically ~-60 mV). The peak amplitude of the optically-evoked excitatory post-synaptic potential (EPSP) or trough amplitude of the inhibitory post-synaptic potential (IPSP) was measured from the average trace using Clampfit 10.7 (Molecular Devices, CA, USA), using the 5 s prior to stimulation as baseline. Tau for the decay phase of the IPSP was estimated by fitting the IPSP with a single exponential, from the IPSP trough until return to baseline. Total voltage area was calculated from 0-5.5 s following the onset of the first light pulse. In cells where optical stimulation evoked only an EPSP the response was classed as an 'excitation', only an IPSP was classed as an 'inhibition', and a combined optically-evoked EPSP and IPSP was classed as 'mixed'. To assess the effect of photostimulation on firing activity, constant positive current was injected to elicit consistent spontaneous action potentials, and 470 nm light (8 pulses at 30 Hz, 5 ms pulse-width) was delivered every 30 s. The interevent interval (IEI) between action potentials was calculated for 5 s before and 5 s after the first pulse of blue light using Clampfit 10.7 (Molecular Devices, CA, USA). A decrease in IEI (indicating an increase in firing rate) was classed as an 'excitation' and an increase in IEI (indicating a decrease in firing rate) was classed as an 'inhibition'.

Following recording, images showing the location of the recording pipette within the slice were captured through a 4X/0.10 NA objective. Images were subsequently overlaid onto the appropriate brain atlas image [126,127], recorded cell locations were annotated, and then converted into x-y coordinates in FIJI. Python was used to generate a scatter plot of cell location, with points color-coded by the overall membrane potential response to photostimulation (Figure 6—figure supplement 1A-C).

Unsupervised agglomerative hierarchical clustering was used to classify cells according to their baseline electrophysiological properties. This approach organizes objects (in this case cells) into clusters, based on their similarity. The electrophysiological properties used as input features for clustering CeA cells were ramp ratio, max firing frequency, firing delay, and voltage sag, which are characteristics that have been previously shown to distinguish between subtypes of CeA neuron [103]. For clustering BLP cells, we replaced ramp ratio with capacitance, as this measure is often used to distinguish between pyramidal neurons and GABAergic interneurons, which are the two main cell types in this region. Data for each cell property was max-min normalized to produce a 4 x *n* matrix of input features (where *n* = total number of cells). Clustering was performed using the 'linkage' function of SciPy [134] in Python, using Ward's linkage method [135] and Euclidean distance. Briefly, this approach begins with each cell assigned to a single cluster. Cells that are in closest proximity (i.e. have highest similarity) are then linked to form a new cluster. Then the next closest clusters are linked, and so on. This process is repeated until all cells are included in a single cluster. The output of this analysis is plotted as a hierarchical tree (dendrogram), in which each cell is a 'leaf' and the Euclidean distance on the y-axis indicates the linkage between cells (larger distance indicates greater dissimilarity). To annotate the photostimulation response of cells on the dendrogram (Figure 6N, 6P, and Figure 6—figure supplement 1M), the response was designated as

‘excitation’ if action potential IEI decreased with optical stimulation and ‘inhibition’ if action potential IEI increased on stimulation. If firing data was not available, cells were designated as showing an ‘excitation’ if only an EPSP was evoked on optical stimulation, and ‘inhibition’ if only an IPSP was evoked. In cells where a mixed EPSP/IPSP was elicited, the response was designated as an ‘excitation’ if the overall voltage area (0-5.5 s following light onset) was positive, and an ‘inhibition’ if the overall voltage area was negative.

At the end of recording, brain slices were fixed in 4% PFA overnight and then washed in 1X PBS (4 x 10 min each). Slices were blocked in 0.3% PBS-T (Sigma-Aldrich, MO, USA) with 3% NDS (Jackson Immunoresearch, PA, USA) for 30-60 min at room temperature. They were then incubated in PBS-T 0.3% with, 3% NDS, and CF405- or CF633-conjugated streptavidin (1:1000; Biotium, CA, USA) for 90 min at room temperature to reveal neurobiotin labelling. Slices were finally washed four times in 1X PBS (10 min each) before being mounted on glass slides and coverslipped using warmed PVA-DABCO (Sigma-Aldrich, MO, USA).

Single molecule fluorescent in situ hybridization (smFISH) with RNAscope

C57BL/6 mice were deeply anesthetized with 5% isoflurane and brains were rapidly extracted and covered with powdered dry ice for ~2 min. Frozen brains were stored in glass vials at -80°C before sectioning at 20 µm using a cryostat (CM3050 S; Leica Biosystems, Germany) at -16°C. Coronal sections were thaw-mounted onto a glass slide, by gentle heating from the underside using the tip of a finger to encourage adhesion of the section to the slide. They were then stored at -80°C until processing.

Fluorescent *in situ* hybridization (FISH) was performed using the RNAscope Multiplex Fluorescent assay v2 (Advanced Cell Diagnostics, CA, USA). The following products were used: RNAscope Multiplex Fluorescent Reagent Kit V2 (Catalog #323110), Fluorescent Multiplex Detection Reagents (#323110), target probes for *Mus musculus* genes – *Drd1a* (#406491-C1), *Drd2* (#406501-C3), *Npbwr1* (#547181-C1), and *Vipr2* (465391-C2) – and the Tyramide Signal Amplification (TSA) Plus Fluorescence Palette Kit (NEL760001KT; PerkinElmer Inc., MA, USA) with fluorophores diluted to 1:1000-1:5000. The protocol was performed as recommended by the manufacturer, with some modifications to prevent tissue degradation and optimize labelling specificity in our regions of interest. Fresh frozen slices were fixed in 4% PFA for 1 hr at 4°C. Slices were dehydrated in an ethanol series (50%, 70%, 100%, and 100% ethanol, 5 min each) and then incubated in hydrogen peroxide for 8 min at room temperature. Protease treatment was omitted in order to prevent tissue degradation. Slides were then incubated with the desired probes (pre-warmed to 40°C and cooled to room temperature) for 2 hr at 40°C in a humidified oven. Following washing (2 x 30 s in 1X RNAscope wash buffer), signal amplification molecules (Amp 1, 2, and 3) were hybridized to the target probes in sequential steps, with 30 min incubation for Amp 1 and 2 and 15 min incubation for Amp 3 at 40°C, all in a 40°C humidified oven followed by washing (2 x 30 s in wash buffer). For fluorescent labelling of each amplified probe, slides were incubated in channel-specific HRP for 10 min, followed by incubation with TSA fluorophore (PerkinElmer, MA, USA) for 20 min, and then incubation in HRP-blocker for 10 minutes (with 2 x 30 s washes between each step). Probes for *Drd1a*, *Drd2*, *Npbwr1*, and *Vipr2* were each labelled with green (TSA Plus Fluorescein), red (TSA Plus Cyanine 3), or far red (TSA Plus Cyanine 5) fluorophores in counterbalanced combinations. Slides were then incubated in DAPI (Advanced Cell Diagnostics, CA, USA) for 10 min, washed in 1X RNAscope wash buffer, dried for 20 min, coverslipped with warmed PVA-DABCO, (Sigma-Aldrich, St. Louis, MO) and left to dry overnight before imaging.

Images were captured on a confocal laser scanning microscope (Olympus FV1000; Olympus, PA, USA) using a 40X/1.30NA oil immersion objective. Serial Z-stack images were acquired using FluoView software version 4.0 (Olympus, PA, USA) at an optical thickness of 1.5 µm. All images were acquired with identical settings for laser power, detector gain, and amplifier offset. A maximum Z-projection was performed in FIJI followed by rolling ball background subtraction to correct for uneven illumination. Image brightness and contrast were moderately adjusted using FIJI, with consistent adjustments made across images for each probe-fluorophore combination. Regions of interest were annotated on each image by overlaying the appropriate brain atlas image [126,127] with guidance from DAPI staining and using the BigWarp plugin (https://imagej.net/BigWarp) [128] in FIJI. These ROI outlines were used to generate binary masks in order to regionally-restrict subsequent image analysis. Automated cell identification and analysis of fluorescent mRNA labelling was performed in CellProfiler [125] using a modified version of the 'Colocalization' template pipeline (https://cellprofiler.org/examples). The pipeline was optimized to identify DAPI labelling (20-40 pixels in diameter), in order to define cell outlines. This was followed by identification of fluorescent mRNA puncta (2-10 pixels in diameter) for each probe. Puncta that were localized within DAPI-identified cells (classified using the 'relate objects' module) were assigned to that cell for subsequent analysis. Quantification and further analysis/data visualization was performed using a custom-written Python code. Violin plots were made using the violin plot function in the Seaborn library [136] of Python (with smoothing set to 0.2), and colocalization matrices were generated using the Seaborn heatmap function.

In vivo microendoscopic calcium imaging

DAT::Cre mice received an injection of 300 nL AAV_9-Syn-FLEX-ChrimsonR-TdTomato in the DRN (ML:1.20, AP:-4.10, DV:-2.90; needle at a 20° angle from the midline, bevel facing medial), and 250 nL AAV_1-Syn-GCaMP6f or AAV_1-Syn-GCaMP67f in the CeA (ML:2.85, AP:-1.20, DV:-4.75, needle bevel facing posterior). After ~4 weeks mice underwent a second surgery to implant an integrated 0.6 mm diameter, 7.3 mm long gradient refractive index (GRIN) lens with attached baseplate (Inscopix, CA, USA) over the CeA (ML: 2.85, AP:-1.50, DV:-4.60). The lens was lowered slowly into the cleaned craniotomy by hand. The GRIN lens was adhered to the skull by a layer of adhesive cement (C&B Metabond; Parkell Inc., NY, USA) followed by a layer of black cranioplastic cement (Ortho-Jet; Lang, IL, USA), and protected by a small PCR tube cap, held in place by cement. The nVoke miniaturized microscope (Inscopix, CA, USA) consists of a 455±8 nm blue LED for GCaMP excitation, and a 620±30 nm red LED for simultaneous optogenetic manipulation [137].

Behavioral experimentation commenced at least 1 week after baseplate surgery. Mice were first habituated to handling and connection of the microscope for a minimum of 3 consecutive days. For recording, mice were connected to the nVoke miniature microscope by tightening a small set screw on the baseplate. The microscope data cable was connected to a commutator (Inscopix, CA, USA), to allow unrestricted movement, and the commutator was itself connected to a data acquisition (DAQ) box. Grayscale images were acquired at a rate of 20 frames/s (fps; ~50 ms exposure time) with the blue LED delivering 0.2-0.3 mW light power and analog gain on the image sensor set to 2. For the social approach task, mice were placed in the three-chamber apparatus (57.5l x 22.5w x 16.5h chamber with clear walls and grey floors). Following microscope connection, mice freely explored the chamber for 5 min. They were then confined to the center portion of the chamber, by the insertion of clear Plexiglas panels, during which a novel juvenile mouse was placed under one cup and a novel object was placed under the other cup. The panels were removed, and the test mouse allowed to freely explore for a further 10 min. One

‘group-housed’ session was conducted without red-light delivery, and another ‘group-housed’ session was conducted with red 620 nm light delivery (8 pulses with 5 ms pulse-width, at 30 Hz, every 1 s; 10 mW) through the objective lens of the microscope, to activate ChrimsonR-expressing DRN^{DAT} terminals. The order of ‘group-housed’ sessions was counterbalanced. 2-3 weeks later, mice were isolated for 24 hours, and another session (‘isolated’) commenced without red-light delivery. A top-down SLEAP[138] (v1.3.1) model was trained using 774 labeled frames, annotating a skeleton composed of 15 keypoints (comprised of (1) nose, (2) head, (3) left ear, (4) right ear, (5) neck, (6) left forelimb, (7) right forelimb, (8) trunk, (9) left hindlimb, (10) right hindlimb, (11) tail base, (12-14) points along the length of the tail, and (15) tail tip). Pose estimation using the trained model was then performed on the behavior videos to determine if there was a social or object cup interaction. To determine if there was a social or object cup interaction, the nose of the mouse must be within 1.3x the diameter of the cup, and the cup must be within a 90° cone in front of the mouse’s head.

Raw videos of GCaMP fluorescence were first pre-processed in Inscopix Data Processing Software 1.3.0 (Inscopix, CA, USA) by cropping the region outside the GRIN lens, applying 2x spatial downsampling, and a 3x3 median filter to fix defective pixels. A spatial band-pass filter was applied (0.005 to 0.5 oscillations/pixel) to remove high and low spatial frequency content, and rigid motion correction was performed (to account for small lateral displacements) by registering to a stable reference frame with a prominent landmark (e.g. blood vessel). Processed recordings were then exported as TIFF stacks for additional piecewise non-rigid motion correction using the NoRMCorre algorithm[139] in overlapping 64 x 64 pixel grids using a MATLAB implementation. Constrained non-negative matrix factorization for endoscopic recordings (CNMF-E) was then used to extract the spatial shapes and calcium signals from individual cells in the imaging field of view[140] using a MATLAB implementation (key parameters: minimum local correlation for seeding pixels = 0.9, minimum peak-to-noise ratio for seeding pixels =12). The extracted calcium signals were inspected, and non-neuronal objects were manually excluded. All following downstream analyses used raw CNMF-E traces.

Calcium traces were aligned to detected behavioral events (interaction to the social and object cups, as determined by feature thresholds extracted from SLEAP keypoints). Single cell responses to social and object cup interaction were determined using an ROC (receiver operating characteristic) analysis, which has been previously been described to determine neural responses to social behavior[108,109]. A binary behavior vector of social or object cup interaction (calculated in 40ms time bins) was compared to a binary neural activity vectors generated by applying thresholds that span 100 steps from the minimum to maximum z-score value of each calcium trace to determine a true positive rate (TPR) and false positive rate (FPR) at each step. From these values yielded an ROC curve for each neuron that corresponded to the performance of that single neuron in predicting social or object cup interactions. The area under the ROC curve (auROC) was used to determine how strongly modulated each neuron was to the social and object stimuli. To determine the significance of single-cell responses, a null distribution of 1,000 auROC values was generated by randomly circularly shifting the binary behavior vectors and again comparing it to the binary neural activity signal. A neuron was considered having a significant excitatory response to the social or object stimulus if the auROC value exceeded the 97.5^{th} percentile of the 1,000 shuffled auROC values, and was considered having a significant inhibitory response if the auROC value was less than the 2.5^{th} percentile of the 1,000 shuffled auROC values.

Co-registration of active neurons during imaging sessions was performed using CellReg[141]. In short, the spatial footprint matrices from each imaging session (as determined by CNMF-E) were used

to align different imaging sessions within each animal to a reference session through translational and rotational shifts. Spatial correlation and centroid distance between cells were used to probabilistically register active cells across sessions.

Agglomerative hierarchical clustering was performed by averaging each neuron's response to the onset of social or object cup interaction throughout the trial. A social or object cup interaction was classified a trial if it (a) lasted a minimum of 1s, (b) if there had been at least 5s that elapsed since the last interaction, and (c) if there was less than 1.5s pause in interaction with the social or object cups. The z-scored averaged traces (5s before and after the onset of social or object cup interaction) were concatenated, such that each row corresponds to one neuronal unit. Agglomerative hierarchical clustering was performed using MATLAB's "cluster" function. Each neuron was initially designated as an individual cluster. Those that were in closest proximity were merged to form a new cluster, then the next closest were merged etc. until a hierarchical tree was formed with all neurons contained within a single cluster. A threshold at 0.770 × max(linkage) was set to prune branches from the hierarchical tree, so that all neurons below each cut were assigned to a single cluster. After the dendrogram was constructed, the average traces (were displayed as a heatmap alongside their corresponding leaf. The traces of all neurons belonging to a single cluster were then averaged, and the number of neurons that corresponded to each behavior group was calculated for each cluster.

Statistical analyses

Statistical tests were performed using GraphPad Prism 8 (GraphPad Software, CA, USA). Normality was evaluated using the D'Agostino-Pearson test, and data are expressed as mean±standard error of the mean (SEM), unless otherwise noted. Data which followed a Gaussian distribution were compared using a paired or unpaired t-test (non-directional) for two experimental groups, and a one-way or two-way ANOVA with repeated measures for three or more experimental groups. Data for two experimental groups which did not follow a Gaussian distribution were compared using a Mann-Whitney *U* test. Correlation between two variables was assessed using the Pearson's product-moment correlation coefficient. Threshold for significance was set at $*p<0.05$, $**p<0.01$ and $***p<0.001$.

Figure Legends

Figure 1. DRN^{DAT} and VTA^{DAT} afferents target distinct downstream regions.

(A) Example images of downstream regions showing TH expression from immunohistochemistry.

(B) eYFP expression in the prefrontal cortex (PFC), nucleus accumbens (NAc), bed nucleus of the stria terminalis (BNST), central amygdala (CeA), and posterior basolateral amygdala (BLP) following injection into the DRN (upper panels) and the VTA (lower panels).

(C) Quantification of mean eYFP fluorescence in subregions from each structure (PFC: *n*=18 and 14 sections, striatum: *n*=20 and 21 sections, BNST: *n*=14 and 13 sections, CeA: *n*=24 and 27 sections, amygdala: *n*=45 and 51 sections from DRN and VTA injections, respectively, from 6 mice). eYFP fluorescence was significantly greater following VTA injection in all striatal subregions (unpaired t-test: CPu: t_{39}=13.23, p<0.0001; NAc core: t_{39}=13.56, p<0.0001; NAc lateral shell: t_{31}=13.01, p<0.0001; NAc medial shell: t_{37}=4.49, p<0.0001), and significantly greater following DRN injection in the BNST oval nucleus (unpaired t-test: t_{22}=3.95, p=0.0007) and CeA lateral division (unpaired t-test: t_{34}=3.18, p=0.0031).

(D) Images from three selected downstream targets showing average terminal density in the middle anteroposterior (AP) region following eYFP expression in DRN^{DAT} (left) or VTA^{DAT} (right) neurons.

(E) The retrograde tracer cholera toxin subunit-B (CTB) conjugated to Alexa Fluor 555 (CTB-555, pseudo-colored magenta) or Alexa-Fluor 647 (CTB-647, pseudo-colored cyan) was injected into two downstream targets.

(F) Confocal images showing representative injection sites for dual BNST and CeA injections (left panels), BNST and BLP (center panels), and CeA and BLP (right panels).

(G) High magnification images of DRN cells expressing CTB-555 (magenta), CTB-647 (cyan), and TH (green) following injection into the BNST and CeA. White arrows indicate triple-labelled cells.

(H) Venn diagrams showing the proportion of CTB+/TH+ cells in the DRN following dual injections placed in the BNST and CeA (left), BNST and BLP (center), or CeA and BLP (right). When injections were placed in the BNST and CeA, dual CTB-labelled TH+ cells constituted 46% of all BNST projectors and 55% of all CeA projectors. In contrast, when injections were placed in the BNST and BLP, or CeA and BLP, the proportion of dual-labelled cells was considerably lower (7.6% of BNST projectors and 9.7% of CeA projectors).

Bar graphs show mean ±SEM. *p<0.05, **p<0.01, ***p<0.001, ****p<0.0001. PFC: Cg=cingulate cortex, PL=prelimbic cortex, IL= infralimbic cortex; striatum: CPu=caudate putamen, NAc core=nucleus accumbens core, NAc l.sh.=nucleus accumbens lateral shell, NAc m.sh.=nucleus accumbens medial shell; BNST: oval nuc.= BNST oval nucleus, lat.=BNST lateral division, med.=BNST medial division, vent.=BNST ventral part; CeL=central amygdala lateral division, CeM=central amygdala medial division, CeC=central amygdala capsular division; amygdala: LA=lateral amygdala, BLA=basolateral amygdala, BLP=basolateral amygdala posterior.

Source data 1. Mean DRN^{DAT} eYFP fluorescence in downstream regions, as shown in ***Figure 1C***.

Source data 2. Colocalization counts of CTB+/TH+ cells in the DRN, as shown in ***Figure 1H***.

Figure supplement 2—source data 1. Colocalization counts of CTB+/TH+ cells in the DRN, as shown in ***Figure 1—figure supplement 2C***.

Figure 1—figure supplement 1. DRN^{DAT} and VTA^{DAT} eYFP virus injection sites.

(A-D) Confocal images at different AP locations through the VTA and DRN showing the typical spread of eYFP expression (green) following an injection of AAV$_5$-DIO-ChR2-eYFP into (A) the DRN and (C) the VTA. Tyrosine hydroxylase (TH; the ratelimiting enzyme in dopamine synthesis) expression from immunohistochemistry is shown in red. (b,d) Insets showing high magnification images of the substantia nigra pars compacta (SNc), VTA, rostral linear nucleus (RLi), caudal linear nucleus (CLi), and DRN. Viral injection in the DRN typically resulted in eYFP-expressing cells within the DRN, ventrolateral periaqueductal grey (vlPAG), and CLi nuclei, with minimal expression in the RLi, and none in the VTA or substantia nigra pars compacta (SNc). In contrast, viral injection in the VTA produced robust eYFP expression in SNc and VTA cell bodies, with some RLi expression, and none in the CLi, vlPAG, or DRN.

Figure 1—figure supplement 2. Verification of dual-retrograde tracing strategy and intersectional approach to reveal axon collaterals.

(A) Two retrograde tracers (CTB-555 and CTB-647) were injected into the same location, followed by sectioning and immunohistochemistry after 7 days. Right panels show example injection site for CTB-555 and CTB-647 in the BNST.

(B) CTB-expressing cells in the DRN with TH (green) revealed by immunohistochemistry. White arrows indicate triple-labelled cells.

(C) Within the TH+ cells in the DRN, injection of both retrograde tracers into the same location resulted in 97% CTB-647+ cells co-labelled with CTB-555, and 100% CTB-555+ cells co-labelled with CTB-647.

(D) Heatmaps indicating the relative density of TH+ CTB+ cells throughout the DRN/CLi for each projector population and (E) dual-labelled cells. Color intensity represents average number of cells per slice. The total number of TH+ BNST and CeA projectors per slice was similar (n=27.9 BNST projectors and n=27.2 CeA projectors per slice), whereas TH+ BLP projectors were significantly fewer in number (n=6.4 BLP projectors per slice; Kruskal-Wallis statistic = 83.5, $p<0.0001$; Dunn's posthoc tests: BNST vs. CeA $p>0.05$, BNST vs BLP $p<0.001$, CeA vs BLP $p<0.001$). TH+ BNST and CeA projectors, and dual-labelled cells, were broadly distributed throughout the DRN, vlPAG, and CLi, with a higher concentration in the dorsal aspect of the DRN, whereas BLP projectors tended to be relatively denser in ventral DRN/CLi.

(F) Injection strategy to enable eYFP expression selectively in the DRN^{DAT}-CeA projection. A retrogradely-travelling HSV construct encoding mCherry-flpo, expressed in a Cre-dependent manner (HSV-LS1L-mCherry-IRES-flpo), was injected into the CeA of a DAT::Cre mouse, and an AAV, expressed in a flpo-dependent manner, encoding eYFP (AAV$_5$-fDIO-eYFP) was injected into the DRN.

(G) After 7 weeks, this resulted in eYFP-expressing TH+ cells in the DRN, and (H) eYFP-expressing processes in both the CeA (upper panels) and BNST (lower panels).

(I) Injection of only AAV$_5$-fDIO-eYFP into the DRN of a DAT::Cre mouse did not result in eYFP expression.

Figure 2. DRN^{DAT}-BLP (but not DRN^{DAT}-BNST or DRN^{DAT}-CeA) photostimulation promotes place avoidance.

(A) AAV_5-DIO-ChR2-eYFP or AAV_5-DIO-eYFP was injected into the DRN of DAT::Cre mice and optic fibers implanted over the BNST, CeA, or BLP to photostimulate DRN^{DAT} terminals. After >7 weeks for viral expression cages of mice were assayed for social dominance using the tube test, prior to other behavioral tasks.

(B-D) Left panels: example tracks of DRN^{DAT}-BNST:ChR2, DRN^{DAT}-CeA:ChR2, and DRN^{DAT}-BLP:ChR2 mice in the real-time place preference (RTPP) assay. Right panels: bar graphs showing the difference in % time spent in the stimulated ('ON') and unstimulated ('OFF') zones. There were no significant RTPP differences detected in (B) DRN^{DAT}-BNST:ChR2 (DRN^{DAT}-BNST:ChR2: *N*=29 mice, DRN^{DAT}-BNST:eYFP: *N*=14 mice; unpaired t-test: t_{41}=1.44, p=0.156) and (C) DRN^{DAT}-CeA:ChR2 mice (DRN^{DAT}-CeA:ChR2: *N*=28 mice, DRN^{DAT}-CeA:eYFP: *N*=13 mice; unpaired t-test: t_{39}=0.828, p=0.413) compared to their respective eYFP control mice groups. However, (D) DRN^{DAT}-BLP:ChR2 mice spent proportionally less time in the stimulated zone relative to DRN^{DAT}-BLP:eYFP mice (DRN^{DAT}-BLP:ChR2: *N*=14 mice, DRN^{DAT}-BLP:eYFP: *N*=8 mice; unpaired t-test: t_{20}=2.13, p=0.0455).

(E-G) Time spent in the ON zone across the 30 min session. (G) DRN^{DAT}-BLP:ChR2 mice spent significantly less time in the ON zone relative to DRN^{DAT}-BLP:eYFP mice (DRN^{DAT}-BLP:ChR2: *N*=14 mice, DRN^{DAT}-BLP:eYFP: *N*=8 mice; repeated measures two-way ANOVA: $F_{1,20}$ = 4.53, main effect of opsin p=0.046).

(H-J) Scatter plots showing relative dominance plotted against the difference in zone time (insets show mean values for subordinate, intermediate, and dominant mice) for (H) DRN^{DAT}-BNST, (I) DRN^{DAT}-CeA, or (J) DRN^{DAT}-BLP mice.

Bar and line graphs display mean ±SEM. *p<0.05.

Source data 1. DRN^{DAT}-BNST:ChR2 RTPP percent time difference (ON-OFF), as shown in ***Figure 2B***.

Source data 2. DRN^{DAT}-CeA:ChR2 RTPP percent time difference (ON-OFF), as shown in ***Figure 2C***.

Source data 3. DRN^{DAT}-BLP:ChR2 RTPP percent time difference (ON-OFF), as shown in ***Figure 2D***.

Source data 4. DRN^{DAT}-BNST:ChR2 RTPP percent time in ON (binned), as shown in ***Figure 2E***.

Source data 5. DRN^{DAT}-CeA:ChR2 RTPP percent time in ON (binned), as shown in ***Figure 2F***.

Source data 6. DRN^{DAT}-BLP:ChR2 RTPP percent time in ON (binned), as shown in ***Figure 2G***.

Source data 7. DRN^{DAT}-BNST:ChR2 RTPP percent time difference (ON-OFF) x relative dominance, as shown in ***Figure 2H***.

Source data 8. DRN^{DAT}-CeA:ChR2 RTPP percent time difference (ON-OFF) x relative dominance, as shown in ***Figure 2I***.

Source data 9. DRN^{DAT}-BLP:ChR2 RTPP percent time difference (ON-OFF) x relative dominance, as shown in ***Figure 2J***.

Figure supplement 1—source data 1. Social rank stability, as shown in ***Figure 2—figure supplement 1H***.

Figure supplement 2—source data 1. DRN^{DAT}-BNST:ChR2 ICSS number of nose pokes, as shown in ***Figure 2—figure supplement 2A***.

Figure supplement 2—source data 2. DRN^{DAT}-CeA:ChR2 ICSS number of nose pokes, as shown in ***Figure 2—figure supplement 2B***.

Figure supplement 2—source data 3. DRN^{DAT}-BLP:ChR2 ICSS number of nose pokes, as shown in ***Figure 2—figure supplement 2C***.

Figure 2—figure supplement 1. Fiber placement in DRN^{DAT} downstream regions and stability of social dominance within cages.

(A-C) Example confocal images showing ChR2-expressing DRN^{DAT} terminals in (A) the BNST, (B) CeA, and (C) BLP.

(D-F) Fiber placement over (D) the BNST, (E) CeA, and (F) BLP. Colored lines indicate ChR2 subjects whereas grey colored lines indicate eYFP subjects. Lighter shade lines indicate unilateral implants, whereas darker shade lines indicate bilateral implants.

(G) The tube test for social dominance was performed prior to optogenetic manipulations.

(H) Proportion of wins for an individual cage tested across four days, and average for all cages used in optogenetic manipulation experiments, separated by number of mice per cage (red=dominant, orange=intermediate, yellow=subordinate).

Graphs show mean ±SEM.

Figure 2—figure supplement 2. Photostimulation of DRN^{DAT} projections does not modify operant intra-cranial self-stimulation behavior.

(A-C) Photostimulation of (A) the DRN^{DAT}-BNST, (B) DRN^{DAT}-CeA, or (C) DRN^{DAT}-BLP projection did not support intra-cranial self-stimulation (ICSS) as shown by a lack of preference for the active nosepoke (paired with blue light delivery) over the inactive nosepoke (unpaired t-test: DRN^{DAT}-BNST: DRN^{DAT}-BNST:ChR2: N=28 mice, DRN^{DAT}-BNST:eYFP: N=16 mice; t_{42}=0.225, p=0.823; DRN^{DAT}-CeA: DRN^{DAT}-CeA:ChR2: N=26 mice, DRN^{DAT}-CeA:eYFP: N=17 mice; t_{41}=0.225, p=0.823; DRN^{DAT}-BLP: DRN^{DAT}-BLP:ChR2: N=14 mice, DRN^{DAT}-BLP:eYFP: N=8 mice; t_{20}=0.152, p=0.881).

Figure 3. DRN^{DAT}-BNST (but not DRN^{DAT}-CeA or DRN^{DAT}-BLP) photostimulation promotes non-social exploratory behavior.

(A-C) Left panels: example tracks in the elevated plus maze (EPM) from a (A) DRN^{DAT}-BNST:ChR2, (B), DRN^{DAT}-CeA:ChR2, and (C), DRN^{DAT}-BLP:ChR2 mouse. Upper right panels: time spent in the open arms of the EPM across the 15-minute session. Photostimulation had no significant effect on time spent in the open arms of the EPM (two-way ANOVA, light x group interaction, BNST – $F_{2,50}$=2.008, p=0.145, CeA – $F_{2,72}$=0.118, p=0.889, BLP – $F_{2,40}$=0.354, p=0.704) for (A) DRN^{DAT}-BNST, (B), DRN^{DAT}-CeA, or (C) DRN^{DAT}-BLP mice. Bottom right panels: difference in time spent in open arms of the EPM between the stimulation ON and first OFF epochs. Photostimulation had no significant effect on time spent in the open arms of the EPM for (A) DRN^{DAT}-BNST (DRN^{DAT}-BNST:ChR2: *N*=19 mice, DRN^{DAT}-BNST:eYFP: *N*=10 mice; unpaired t-test: t_{27}=1.39, p=0.177), (B) DRN^{DAT}-CeA (DRN^{DAT}-CeA:ChR2: *N*=23 mice, DRN^{DAT}-CeA:eYFP: *N*=14 mice; unpaired t-test: t_{35}=0.639, p=0.527), or (C) DRN^{DAT}-BLP mice (DRN^{DAT}-BLP:ChR2: *N*=14 mice, DRN^{DAT}-BLP:eYFP: *N*=8 mice; unpaired t-test: t_{20}=0.759, p=0.457).

(D-F) Scatter plots showing relative dominance plotted against the difference in the open arm zone time (insets show mean values for subordinate, intermediate, and dominant mice) for (D) DRN^{DAT}-BNST, (E) DRN^{DAT}-CeA, or (F) DRN^{DAT}-BLP mice.

(G-I) Home-cage behavior was assessed in the juvenile intruder assay across two counterbalanced sessions, one paired with photostimulation ('ON') and one without ('OFF') for (G) DRN^{DAT}-BNST, (H) DRN^{DAT}-CeA, or (I) DRN^{DAT}-BLP mice. DRN^{DAT}-BNST photostimulation increased time spent rearing (DRN^{DAT}-BNST:ChR2: *N*=24 mice, DRN^{DAT}-BNST:eYFP: *N*=13 mice; paired t-test: t_{23}=2,32, p=0.0298), but DRN^{DAT}-CeA and DRN^{DAT}-BLP photostimulation did not.

(J-L) Scatter plots showing relative dominance plotted against the difference in rearing time with optical stimulation (ON-OFF) (insets show mean values for subordinate, intermediate, and dominant mice) for (J) DRN^{DAT}-BNST, (K) DRN^{DAT}-CeA, or (L) DRN^{DAT}-BLP mice.

Bar and line graphs display mean ±SEM. *p<0.05

Figure 3—figure supplement 1. Photostimulation of DRN^{DAT} projections does not modify locomotor or anxiety-like behavior.

(A-C) Example tracks in the open field test from a (A) DRN^{DAT}-BNST:ChR2, (B) DRN^{DAT}-CeA:ChR2, and (C) DRN^{DAT}-BLP:ChR2 mouse. Photostimulation had no significant effect on time spent in the center of the open field (two-way ANOVA, light x group interaction, BNST – $F_{2,90}$=0.2105, p=0.811; CeA – $F_{2,92}$=0.528, p=0.592; BLP – $F_{2,40}$=0.181, p=0.835) or distance travelled (two-way RM ANOVA, light x group interaction, BNST – $F_{2,90}$=0.209, p=0.812; CeA – $F_{2,92}$=0.108, p=0.898; BLP – $F_{2,40}$=0.252, p=0.771) for DRN^{DAT}-BNST, DRN^{DAT}-CeA, or DRN^{DAT}-BLP mice.

Line and bar graphs show mean±SEM.

Figure 4. DRN^{DAT}-CeA (but not DRN^{DAT}-BNST or DRN^{DAT}-BLP) photostimulation promotes sociability in a rank-dependent manner.

(A-C) Heatmaps showing the relative location of ChR2-expressing mice in the three chamber sociability assay, with optic fibers located over the (A) BNST, (B) CeA, or (C) BLP. The task was repeated across two days, with one session paired with photostimulation ('ON') and one without ('OFF').

(D-F) Bar graphs showing social preference in three chamber sociability assay. (D) Photostimulation of DRN^{DAT}-BNST terminals (8 pulses of 5 ms pulse-width 473 nm light, delivered at 30 Hz every 5 s) in ChR2-expressing mice (DRN^{DAT}-BNST:ChR2) had no significant effect on time spent in the social zone relative to the object zone (DRN^{DAT}-BNST:ChR2: *N*=27 mice, DRN^{DAT}-BNST:eYFP: *N*=14 mice; 'social:object ratio'; paired t-test: t_{26}=0.552, p=0.586), (E) but increased social:object ratio for DRN^{DAT}-CeA:ChR2 mice (DRN^{DAT}-CeA:ChR2: *N*=29 mice, DRN^{DAT}-CeA:eYFP: *N*=13 mice; paired t-test: t_{28}=2.91; corrected for multiple comparisons: p=0.021) (F) and had no significant effect for DRN^{DAT}-BLP:ChR2 mice (DRN^{DAT}-BLP:ChR2: *N*=14 mice, DRN^{DAT}-BLP:eYFP: *N*=7 mice; paired t-test: t_{13}=1.62, p=0.130).

(G-I) Scatter plots displaying relative dominance plotted against the change in social zone time with optical stimulation (ON-OFF) for (G) DRN^{DAT}-BNST, (H) DRN^{DAT}-CeA, or (I) DRN^{DAT}-BLP mice, showing significant positive correlation in DRN^{DAT}-CeA:ChR2 mice (Pearson's correlation: r=0.549, p=0.002, *N*=29 mice). Inset bar graphs show mean values for subordinate, intermediate, and dominant mice.

(J-L) Home-cage behavior was assessed in the juvenile intruder assay across two counterbalanced sessions, one paired with photostimulation ('ON') and one without ('OFF') for (J) DRN^{DAT}-BNST, (K) DRN^{DAT}-CeA, or (L) DRN^{DAT}-BLP mice. DRN^{DAT}-CeA photostimulation in ChR2-expressing mice increased time spent engaged in face investigation with the juvenile mouse (DRN^{DAT}-CeA:ChR2: *N*=22 mice, DRN^{DAT}-CeA:eYFP: *N*=14 mice; paired t-test: t_{22}=2.36, p=0.027).

(M-O) Scatter plots showing relative dominance plotted against the difference in face investigation time with optical stimulation (ON-OFF) (insets show mean values for subordinate, intermediate, and dominant mice) for (M) DRN^{DAT}-BNST, (N) DRN^{DAT}-CeA, or (O) DRN^{DAT}-BLP mice.

(P) A two-state Markov model was used to examine behavioral transitions during the juvenile intruder assay for DRN^{DAT}-CeA mice.

(Q-R) Bar graphs showing the difference in transition probability (ON-OFF) for (Q) within-state transitions and (R) across-state transitions, for DRN^{DAT}-CeA:ChR2 and $ChR2^{eYFP}$ mice. There was no significant difference between ChR2 and eYFP groups for the change in within-state transition probability (DRN^{DAT}-CeA:ChR2: *N*=22 mice, DRN^{DAT}-CeA:eYFP: *N*=14 mice; two-way ANOVA: opsin x transition interaction, $F_{1,68}$=3.385, p=0.0702), (R) but there was a significant interaction between opsin and across-state transition probability (DRN^{DAT}-CeA:ChR2: *N*=22 mice, DRN^{DAT}-CeA:eYFP: *N*=14 mice; two-way ANOVA: opsin x transition interaction, $F_{1,68}$=4.452, p=0.0385) with photostimulation.

Bar and line graphs display mean ±SEM. *p<0.05, **p<0.01.

Source data 1. DRN^{DAT}-BNST:ChR2 three-chamber social:object ratio, as shown in ***Figure 4D***.

Source data 2. DRN^{DAT}-CeA:ChR2 three-chamber social:object ratio, as shown in ***Figure 4E***.

Source data 3. DRN^{DAT}-BLP:ChR2 three-chamber social:object ratio, as shown in ***Figure 4F***.

Source data 4. DRN^{DAT}-BNST:ChR2 time spent in social zone (ON-OFF) x relative dominance, as shown in ***Figure 4G***.

Source data 5. DRN^{DAT}-CeA:ChR2 time spent in social zone (ON-OFF) x relative dominance, as shown in ***Figure 4H***.

Source data 6. DRN^{DAT}-BLP:ChR2 time spent in social zone (ON-OFF) x relative dominance, as shown in ***Figure 4I***.

Source data 7. DRN^{DAT}-BNST:ChR2 juvenile intruder time spent in face investigation, as shown in ***Figure 4J***.

Source data 8. DRN^{DAT}-CeA:ChR2 juvenile intruder time spent in face investigation, as shown in ***Figure 4K***.

Source data 9. DRN^{DAT}-BLP:ChR2 juvenile intruder time spent in face investigation, as shown in ***Figure 4L***.

Source data 10. DRN^{DAT}-BNST:ChR2 juvenile intruder time spent in face investigation (ON-OFF) x relative dominance, as shown in ***Figure 4M***.

Source data 11. DRN^{DAT}-CeA:ChR2 juvenile intruder time spent in face investigation (ON-OFF) x relative dominance, as shown in ***Figure 4N***.

Source data 12. DRN^{DAT}-BLP:ChR2 juvenile intruder time spent in face investigation (ON-OFF) x relative dominance, as shown in ***Figure 4O***.

Source data 13. DRN^{DAT}-CeA:ChR2 juvenile intruder markov model (transition within state), as shown in ***Figure 4Q***.

Source data 14. DRN^{DAT}-CeA:ChR2 juvenile intruder markov model (transition across states), as shown in ***Figure 4R***.

Figure supplement 1—source data 1. DRN^{DAT}-BNST:ChR2 juvenile intruder rearing time x face investigation time (ON-OFF), as shown in ***Figure 4—figure supplement 1A***.

Figure supplement 1—source data 2. DRN^{DAT}-BNST:ChR2 juvenile intruder rearing time x face investigation time (ON-OFF), as shown in ***Figure 4—figure supplement 1B***.

Figure supplement 1—source data 3. DRN^{DAT}-BNST:ChR2 juvenile intruder rearing time x face investigation time (ON-OFF), as shown in ***Figure 4—figure supplement 1C***.

Figure supplement 1—source data 4. Baseline behavioral measures correlation matrix (r-values), as shown in ***Figure 4—figure supplement 1D***.

Figure supplement 1—source data 5. Baseline behavioral measures correlation matrix (p-values), as shown in ***Figure 4—figure supplement 1D***.

Figure supplement 1—source data 6. Baseline behavioral measures (raw values), as shown in ***Figure 4—figure supplement 1D-E***.

Figure 4—figure supplement 1. Photostimulation of DRN^{DAT} projections effects on juvenile behavior, and analysis of baseline behavioral traits.

(A-C) Scatter plots displaying the change in face investigation against the change in rearing with photostimulation (ON-OFF) for (A) DRN^{DAT}-BNST:ChR2, (B) DRN^{DAT}-CeA:ChR2, (C) and DRN^{DAT}-BLP:ChR2 mice in the juvenile intruder assay. Outer plots are probability density curves, using kernel density estimation, to show the distribution of each behavior.

(D) Correlation matrix indicating the relationship between baseline behavioral measures for all mice used in Figures 2-4 and associated supplement figures. For the open field test (OFT) and elevated-plus maze (EPM) the first 5 min of the task were used and for the juvenile intruder and 3 chamber assays the data from the 'OFF' session was used.

(E) Principal component analysis (PCA) of behavioral measures with point color representing the social dominance score for each animal. Inset, scree plot showing % variance explained by the first 5 PCs.

Line and bar graphs show mean±SEM.

Figure 5. Spatial segregation of dopamine and neuropeptide receptor populations within DRN^{DAT} terminal fields.

(A) Mean projection of terminal density in the middle anteroposterior (AP) region of the BNST, following eYFP expression in DRN^{DAT} (left) or VTA^{DAT} (right) neurons.

(B) Mean projection showing fluorescent puncta in the BNST indicating detection of *Drd1* (red), *Drd2* (yellow), *Vipr2* (green), or *Npbwr1* (blue) mRNA transcripts.

(C) Line graphs showing the percent of cells expressing each receptor (≥5 puncta) across AP locations for the oval nucleus, dorsolateral BNST, and dorsomedial BNST (two-way ANOVA, oval nucleus: probe x AP interaction, $F_{9,160}$=6.194, p<0.0001, dorsolateral BNST: probe x AP interaction, $F_{12,167}$=3.410, p=0.0002, dorsomedial BNST: probe x AP interaction, $F_{12,161}$=2.268, p=0.0110). *Drd1*: *n*=51,55,53 *Drd2*: *n*=52,55,53 *Vipr2*: *n*=37,39,37 *Npbwr1*: *n*=36,38,38 sections, for oval nucleus, dorsolateral BNST, and dorsomedial BNST, respectively, from 4 mice.

(D) Matrices indicating overlap between mRNA-expressing cells: square shade indicates the percent of cells expressing the gene in the column from within cells expressing the gene in the row.

(E) Mean projection of terminal density in the middle AP region of the CeA, following eYFP expression in DRN^{DAT} (left) or VTA^{DAT} (right) neurons.

(F) Mean projection showing fluorescent puncta in the CeA indicating mRNA expression.

(G) Line graphs showing the % of cells expressing each receptor (≥5 puncta) across AP locations for the CeL, CeM, and CeC (two-way ANOVA, CeL: probe x AP interaction, $F_{12,220}$=8.664, p<0.0001, CeM: main effect of probe, $F_{3,186}$=60.30, p<0.0001, CeC: probe x AP interaction, $F_{12,218}$=4.883, p<0.0001). *Drd1*: *n*=47,40,47 *Drd2*: *n*=70,55,70 *Vipr2*: *n*=65,57,63 *Npbwr1*: *n*=62,50,60 sections, for CeL, CeM, and CeC, respectively, from 4 mice.

(H) Matrices indicating overlap between mRNA-expressing cells.

(I) Mean projection of terminal density in the middle AP region of the BLP, following eYFP expression in DRN^{DAT} (left) or VTA^{DAT} (right) neurons.

(J) Mean projection showing fluorescent puncta in the BLP indicating mRNA expression.

(K) Line graphs showing the percent of cells expressing each receptor (≥5 puncta) across AP locations for the BLP and BMP (two-way ANOVA, BLP: probe x AP interaction, $F_{15,176}$=2.165, p=0.0091, BMP: main effect of probe, $F_{3,141}$=56.92, p<0.0001). *Drd1*: *n*=55,44 *Drd2*: *n*=59,46 *Vipr2*: *n*=41,33 *Npbwr1*: *n*=45,34 sections, for BLP and BMP, respectively, from 4 mice.

(L) Matrices indicating overlap between mRNA-expressing cells. Line graphs show mean ±SEM.

Source data 1. BNST RNAScope sub-regional probe expression (percent), as shown in ***Figure 5C***.

Source data 2. BNST RNAScope sub-regional probe co-expression, as shown in ***Figure 5D***.

Source data 3. CeA RNAScope sub-regional probe expression (percent), as shown in ***Figure 5G***.

Source data 4. CeA RNAScope sub-regional probe co-expression, as shown in ***Figure 5H***.

Source data 5. BLA RNAScope sub-regional probe expression (percent), as shown in ***Figure 5K***.

Source data 6. BLA RNAScope sub-regional probe co-expression, as shown in ***Figure 5L***.

Figure supplement 1—source data 1. Number of puncta x pixels occupied for all RNAScope probes, as shown in ***Figure 5—figure supplement 1B***.

Figure supplement 1—source data 2. BNST RNAScope sub-regional probe expression (percent, threshold = 1 punctum/cell), as shown in ***Figure 5—figure supplement 1D***.

Figure supplement 1—source data 3. BNST RNAScope sub-regional probe expression (percent, threshold = 3 puncta/cell), as shown in ***Figure 5—figure supplement 1E***.

Figure supplement 1—source data 4. CeA RNAScope sub-regional probe expression (percent, threshold = 1 punctum/cell), as shown in ***Figure 5—figure supplement 1G***.

Figure supplement 1—source data 5. CeA RNAScope sub-regional probe expression (percent, threshold = 3 puncta/cell), as shown in ***Figure 5—figure supplement 1H***.

Figure supplement 1—source data 6. BLA RNAScope sub-regional probe expression (percent, threshold = 1 punctum/cell), as shown in ***Figure 5—figure supplement 1J***.

Figure supplement 1—source data 7. BLA RNAScope sub-regional probe expression (percent, threshold = 3 puncta/cell), as shown in ***Figure 5—figure supplement 1K***.

Figure 5—figure supplement 1. Analysis of mRNA expression using different thresholds qualitatively shows similar spatial pattern of dopamine and neuropeptide receptor expression in downstream regions.

(A) Workflow for RNAscope and image processing.

(B) Scatter plots showing a linear relationship between fluorescent pixels/cell and number of puncta/cell for three separate sections for each probe.

(C) Violin plots displaying puncta count per section for each receptor in the BNST (white circle indicates median; *Drd1*: *n*=51,55,53 *Drd2*: *n*=52,55,53 *Vipr2*: *n*=37,39,37 *Npbwr1*: *n*=36,38,38 sections, for oval nucleus, dorsolateral BNST, and dorsomedial BNST, respectively, from 4 mice).

(D) Line graphs for each BNST subregion showing the number of expressing cells when using a threshold of 1 punctum/cell and (E) 3 puncta per cell.

(F) Violin plots displaying puncta count per section for each receptor in the CeA (white circle indicates median; *Drd1*: *n*=47,40,47 *Drd2*: *n*=70,55,70 *Vipr2*: *n*=65,57,63 *Npbwr1*: *n*=62,50,60 sections, for CeL, CeM, and CeC, respectively, from 4 mice).

(G) Line graphs for each CeA subregion showing the number of expressing cells when using a threshold of 1 punctum/cell and (H) 3 puncta per cell.

(I) Violin plots displaying puncta count per section for each receptor in the amygdala (white circle indicates median; *Drd1*: *n*=55,44 *Drd2*: *n*=59,46 *Vipr2*: *n*=41,33 *Npbwr1*: *n*=45,34 sections, for BLP and BMP, respectively, from 4 mice).

(J) Line graphs for each amygdala subregion showing the number of expressing cells when using a threshold of 1 punctum/cell and (K) 3 puncta per cell. These lower thresholds yielded more expressing

cells than using 5 puncta/cell (compare with Fig. 3c,g,k), but with a similar expression pattern across subregions and AP location.

(L-M) Example images showing expression of *Vipr1* and *Vipr2* within the BNST and CeA. We typically observed greater *Vipr2* than *Vipr1* expression, and high co-localization, and therefore concentrated our detailed analyses on *Vipr2*.

Line graphs show mean±SEM.

Figure 6. DRN^{DAT} input distinctly influences downstream activity in each downstream target.

(A-C) In mice expressing ChR2 in DRN^{DAT} neurons, *ex vivo* electrophysiological recordings were made from (A) the BNST, (B), CeA, and (C), BLP.

(D-F) Photostimulation of DRN^{DAT} terminals with blue light (8 pulses delivered at 30 Hz) evoked both excitatory and inhibitory responses at resting membrane potentials in (D) the BNST, (E) CeA, and (F) BLP. Traces show single sweeps and pie charts indicate proportion of cells with no response ('none'), an EPSP only ('excitation'), an IPSP only ('inhibition'), or a mixed combination of EPSPs and IPSPs ('mix'). Recorded cells: BNST *n*=19, CeA *n*=36, BLP *n*=48.

(G-I) When constant current was injected to elicit spontaneous firing, (G) BNST cells responded to photostimulation with an increase in firing ('excitation'), while (H) CeA and (I) BLP cells responded with an increase or a decrease in firing ('inhibition'). Recorded cells: BNST *n*=5, CeA *n*=20, BLP *n*=17.

(J) Properties of the optically-evoked excitatory post-synaptic potential (EPSP) at resting membrane potentials – left: peak amplitude (Kruskal-Wallis statistic = 6.790, p=0.0335; Dunn's posts-hoc tests: CeA vs BLP p=0.0378); middle: change in amplitude across light pulses; right: violin plots showing distribution of onset latencies (white circle indicates median).

(K) Properties of the optically-evoked inhibitory post-synaptic potential (IPSP) at resting membrane potentials – left panel: trough amplitude (one-way ANOVA, $F_{2,31}$=8.150, p=0.0014, CeA vs BLP: **p=0.0014); middle panel: violin plot showing latency to trough peak; right panel: violin plot showing tau for the current decay (white circle indicates median).

(L) Workflow for agglomerative hierarchical clustering of CeA neurons and (M) BLP neurons. Four baseline electrical properties were used as input features (following max-min normalization) and Ward's method used to generate a cluster dendrogram, grouping cells based on Euclidean distance.

(N) Dendrogram for CeA cells indicating two major clusters, with their response to DRN^{DAT} input indicated below each branch (excitatio*n*=black; inhibitio*n*=grey; no response=open).

(O) Upper panels: cluster 1 showed baseline properties typical of 'late-firing' neurons and cluster 2 showed baseline properties typical of 'regular-firing' neurons. Lower panels: pie charts showing the response of cells in each cluster to DRN^{DAT} input.

(P) Dendrogram for BLP cells indicating two major clusters, with their response to DRN^{DAT} input indicated below each branch (excitatio*n*=black; inhibitio*n*=grey; no response=open).

(Q) Upper panels: cluster 1 showed baseline properties typical of pyramidal neurons and cluster 2 showed baseline properties typical of GABA interneurons. Lower panels: pie charts showing the response of cells in each cluster to DRN^{DAT} input.

Bar and line graphs show mean ±SEM. *p<0.05, **p<0.01.

Source data 1. BNST (resting) *ex vivo* responses to DRN^{DAT} optical stimulation, as shown in ***Figure 6D***.

Source data 2. CeA (resting) *ex vivo* responses to DRN^{DAT} optical stimulation, as shown in ***Figure 6E***.

Source data 3. BLP (resting) *ex vivo* responses to DRN^{DAT} optical stimulation, as shown in ***Figure 6F***.

Source data 4. BNST (firing) *ex vivo* responses to DRN^{DAT} optical stimulation, as shown in ***Figure 6G***.

Source data 5. CeA (firing) *ex vivo* responses to DRN^{DAT} optical stimulation, as shown in ***Figure 6H***.

Source data 6. BLP (firing) *ex vivo* responses to DRN^{DAT} optical stimulation, as shown in ***Figure 6I***.

Source data 7. BNST/CeA/BLP *ex vivo* EPSP peak amplitude in response to DRN^{DAT} optical stimulation, as shown in ***Figure 6J***.

Source data 8. BNST/CeA/BLP *ex vivo* EPSP normalized amplitude in response to DRN^{DAT} optical stimulation, as shown in ***Figure 6J***.

Source data 9. BNST/CeA/BLP *ex vivo* EPSP onset latency in response to DRN^{DAT} optical stimulation, as shown in ***Figure 6J***.

Source data 10. BNST/CeA/BLP *ex vivo* IPSP trough amplitude in response to DRN^{DAT} optical stimulation, as shown in ***Figure 6K***.

Source data 11. BNST/CeA/BLP *ex vivo* IPSP trough latency in response to DRN^{DAT} optical stimulation, as shown in ***Figure 6K***.

Source data 12. BNST/CeA/BLP *ex vivo* IPSP decay tau in response to DRN^{DAT} optical stimulation, as shown in ***Figure 6K***.

Source data 13. CeA *ex vivo* baseline cell properties used for hierarchical clustering, as shown in ***Figure 6L-O***.

Source data 14. BLP *ex vivo* baseline cell properties used for hierarchical clustering, as shown in ***Figure 6M-Q***.

Figure supplement 1—source data 1. BNST/CeA/BLP *ex vivo* EPSP/IPSP normalized peak amplitude in response to DRN^{DAT} optical stimulation with TTX/4AP application, as shown in ***Figure 6—figure supplement 1E***.

Figure supplement 1—source data 2. BNST/CeA/BLP *ex vivo* EPSP/IPSP peak/trough pre-stimulation membrane potential, as shown in ***Figure 6—figure supplement 1F***.

Figure supplement 1—source data 3. BNST/CeA/BLP action potential inter-event intervals, as shown in ***Figure 6—figure supplement 1G***.

Figure supplement 1—source data 4. CeA baseline cell properties by cluster, as shown in ***Figure 6—figure supplement 1H***.

Figure supplement 1—source data 5. BLP baseline cell properties by cluster, as shown in ***Figure 6—figure supplement 1I***.

Figure supplement 1—source data 6. Effect of DRN^{DAT} input on CeA cell properties by cluster (EPSPs/IPSPs), as shown in ***Figure 6—figure supplement 1J***.

Figure supplement 1—source data 7. Effect of DRN^{DAT} input on CeA total voltage area by cluster, as shown in ***Figure 6—figure supplement 1J***.

Figure supplement 1—source data 8. Effect of DRN^{DAT} input on BLP cell properties by cluster (EPSPs/IPSPs), as shown in ***Figure 6—figure supplement 1K***.

Figure supplement 1—source data 9. Effect of DRN^{DAT} input on BLP total voltage area by cluster, as shown in ***Figure 6—figure supplement 1K***.

Figure supplement 1—source data 10. CeA/BLP *ex vivo* baseline cell properties used for hierarchical clustering, as shown in ***Figure 6—figure supplement 1L-M***.

Figure 6—figure supplement 1. Effect of DRN^{DAT} photostimulation on downstream cellular excitability *ex vivo*.

(A-C) Example DIC image, and corresponding eYFP fluorescence, of a brain slice containing (A) the BNST, (B) CeA, or (C) BLP during *ex vivo* recording. Regional maps show the location of recorded cells, with color indicating the change in membrane potential elicited by optical stimulation of DRN^{DAT} terminals.

(D) Example traces showing the optically-evoked EPSP (upper panels) and slow component of the IPSP (lower panels) was maintained following application of TTX/4AP.

(E) Normalized peak amplitude of the EPSP and IPSP following TTX/4AP (EPSP, n=8; IPSP, n=3).

(F) Scatter plots showing the amplitude of the optically-evoked EPSP (left) and IPSP (right) recorded in downstream locations plotted against baseline membrane potential.

(G) Line graphs showing the action potential inter-event interval (IEI) in cells where constant current was injected to elicit firing. Raw (left) and normalized (right) IEI 5.5 s before and 5 s after optical stimulation of DRN^{DAT} terminals (blue shading) in BNST, CeA, and BLP cells. Cells which showed a reduction in IEI with optical stimulation were labelled ‘excited’ (excit., black) and cells which showed an increase in IEI with optical stimulation were defined as ‘inhibited’ (inhib., grey).

(H) Box-and-whisker plots comparing the baseline cell properties (used as input features for hierarchical clustering; Fig. 4P-U) of the two CeA clusters and (I) the two BLP clusters. Unpaired t-tests for CeA – ramp ratio: t_{24}=3.502, p=0.0018; max instantaneous firing frequency (max $freq_{inst.}$): t_{24}=4.698, p<0.0001, firing delay: t_{24}=5.050, p<0.0001, voltage sag: t_{24}=3.983, p=0.0006; unpaired t-tests for BLP – capacitance: t_{25}=4.803, p<0.0001, max $freq_{inst.}$: t_{25}=15.48, p<0.0001, firing delay: t_{25}=2.743, p=0.0111, voltage sag: t_{25}=2.705, p=0.0121.

(J) Box-and-whisker plots for the two CeA clusters and (K) the two BLP clusters showing the amplitude and latency of the EPSP and IPSP, and the combined total voltage area elicited by optical stimulation of DRN^{DAT} terminals. EPSP peak amplitude, CeA: unpaired t-test, t_{17}=1.40, p=0.180; BLP: unpaired t-test t_{22}=2.34, p=0.029. EPSP latency, CeA: unpaired t-test, t_{17}=0.673, p=0.510; BLP: Mann-Whitney U = 33.5, p=0.032. Total voltage area, CeA: Mann-Whitney U = 22, p=0.0023; BLP: Mann-Whitney U = 29, p=0.0019.

(L) Workflow for agglomerative hierarchical clustering of all CeA and BLP neurons combined. Five cell properties were used as input features, corresponding to the five used in Fig. 4P-U for separate clustering of CeA and BLP cells.

(M) Dendrogram indicating two major clusters, with the cell location and response to DRN^{DAT} input indicated by the colored bars below each branch (CeA – pink, BLP – blue; excitation=black; inhibition=grey; no response=open).

(N) Pie charts showing the response of cluster 1 and cluster 2 CeA cells (upper) and BLP cells (lower) to optical stimulation DRN^{DAT} input. *p<0.05, **p<0.01, ***p<0.001, ****p<0.0001.

Figure 7. Simultaneous calcium imaging of CeA neurons and optogenetic stimulation of DRN^{DAT} terminals in CeA.

(A) AAV_1-hSyn-GCaMP7f was injected into the CeA and AAV_8-hSyn-FLEX-ChrimsonR-TdTomato or AAV_1-CAG-FLEX-TdTomato was injected into the DRN of DAT-Cre mice, and a GRIN lens was implanted over CeA. Experiments were conducted 7 weeks following surgery to allow adequate virus expression in axon terminals.

(B) Example spatial correlation image and extracted ROIs of CeA neurons following calcium imaging processing.

(C) Three chamber sociability paradigm. While group-housed, mice explored a three-chamber apparatus with a novel male juvenile stimulus on one side and a novel object stimulus on the other. During one day of the imaging experiment, DRN^{DAT} terminals were not stimulated, and in another session, DRN^{DAT} terminals were stimulated with red light delivery. Mice underwent a third imaging session, without photostimulation, following 24 hours of social isolation.

(D) Mice first explored the three-chamber apparatus without social or object stimuli for a 5-minute habituation period, then with the social and object stimuli for a 10-minute test period.

(E) Social:object ratio (left) and total social cup interaction time (right) during GH stimulation and no stimulation sessions and 24 hours isolated session in mice expressing ChrimsonR in DRN^{DAT} neurons. Bar and line graphs represent mean ±SEM (*N*=12 mice; mixed-effects model: $F_{1.897,30.36}$=0.5767, p=0.5591).

(F) Representative traces from CeA calcium imaging during one three chamber imaging session.

(G) Scatter and distribution plots indicating the response strength (auROC) of recorded CeA neurons to social and object cups (GH off: *n*=429 cells, *N*=15 mice; GH on: *n*=441 cells, *N*=15 mice; SI off: *n*=484 cells, *N*=15 mice).

(H) Difference in response strength (Δ auROC) of CeA neurons to social and object cups (GH off: *n*=429 cells; GH on: *n*=441 cells; SI off: *n*= 484 cells) Kruskal-Wallis test: K-W statistic: 6.172, *p=0.0457; Dunn's multiple comparisons test: GH off vs GH on—p=0.0580, GH off vs SI off—p>0.9999).

(I) Venn diagrams showing overlap of social-encoding neurons (displaying an excitatory response, left, or an inhibitory response, right as defined with auROC) in GH off and GH on sessions (GH off and GH on co-registered neurons: *n*=202 cells). 16 co-registered GH off cells and 18 GH on cells exhibited an excitatory response to social stimulus with 2 cells having the same response across conditions, whereas 12 co-registered GH off and 11 GH on cells exhibited an inhibitory response with 2 cells having the same response across conditions.

(J) Proportion of CeA neurons responsive to social and object cups, further classified as an excitatory (green) or inhibitory (red) response to the stimulus as defined with auROC.

(K) Proportion of recorded neurons that have an excitatory or inhibitory response to the social cup and (L) to the object cup (*N*=12 mice).

(M) Correlation between social preference in three chamber task and the proportion of CeA neurons that have an excitatory response to the social cup. The proportion of socially excited neurons is positively correlated with soc:obj zone ratio only for the GH on condition (pearson correlation: r= 0.6785, p=0.0445, *N*=9 mice). Bar and line graphs show mean ±SEM. *p<0.05.

Source data 1. DRN^{DAT}-CeA:ChrimsonR three-chamber social:object ratio and social zone duration, as shown in ***Figure 7E.***

Source data 2. CeA response strength to social and object stimuli, as shown in ***Figure 7G.***

Source data 3. CeA response strength (change in auROC, social – object), as shown in ***Figure 7H.***

Source data 4. CeA response overlap of social-encoding neurons, as shown in ***Figure 7I.***

Source data 5. CeA response classification to social and object stimuli, as shown in ***Figure 7J.***

Source data 6. Percentage of CeA neurons excited/inhibited by social stimulus, as shown in ***Figure 7K.***

Source data 7. Percentage of CeA neurons excited/inhibited by object stimulus, as shown in ***Figure 7L.***

Source data 8. Proportion of CeA neurons excited by social stimulus x social:object ratio, as shown in ***Figure 7M.***

Figure supplement 1—source data 1. CeA *ex vivo* EPSP/IPSP voltage peak in response to 635nm or 470nm wavelength light, as shown in ***Figure 7—figure supplement 1E****.*

Figure supplement 1—source data 2. CeA *ex vivo* EPSP/IPSP voltage area in response to 635nm or 470nm wavelength light, as shown in ***Figure 7—figure supplement 1F****.*

Figure supplement 1—source data 3. CeA *ex vivo* EPSP/IPSP voltage peak in response to just 635nm or simultaneous 635nm and 470nm wavelength light, as shown in ***Figure 7—figure supplement 1H****.*

Figure supplement 1—source data 4. CeA *ex vivo* EPSP/IPSP voltage area in response to just 635nm or simultaneous 635nm and 470nm wavelength light, as shown in ***Figure 7—figure supplement 1I****.*

Figure supplement 1—source data 5. DRN^{DAT}-CeA:TdTomato three-chamber social:object ratio and social zone duration, as shown in ***Figure 7—figure supplement 1J-K.***

Figure supplement 1—source data 6. CeA response strength (change in auROC, social – object), as shown in ***Figure 7—figure supplement 1L.***

Figure supplement 1—source data 7. Proportion of CeA neurons excited by object stimulus x social:object ratio, as shown in ***Figure 7—figure supplement 1N.***

Figure supplement 1—source data 8. Proportion of CeA neurons inhibited by social stimulus x social:object ratio, as shown in ***Figure 7—figure supplement 1O.***

Figure 7—figure supplement 1. Ex vivo validation of simultaneous calcium imaging and photostimulation and behavioral and neural effects of DRN^{DAT}-CeA:TdTomato stimulation in CeA.

(A) Representative images of GCaMP-expressing cells in the CeA beneath the GRIN lens, and DRN^{DAT} terminals expressing ChrimsonR.

(B) ChrimsonR was expressed in DRN^{DAT} neurons by injection of AAV9-Syn-FLEX-ChrimsonR-Tdtomato into the DRN of DAT::Cre mice, and (C) after 7 weeks whole-cell patch-clamp electrophysiological recordings were made from CeA neurons.

(D) Example EPSP and IPSP evoked by delivery of 635 nm red light or 470 nm blue light (8 pulses, with 5 ms pulse-width, at 30Hz).

(E) Peak amplitude and (F) area of optically-evoked potential elicited by 635 nm (10 mW) and 470 nm (0.3 and 0.2 mW) light. Inset bar graphs show normalized data. Red light evoked a PSP with a significantly greater peak amplitude (repeated measures ANOVA, $F_{2,16}$=200.1, p<0.0001, red vs 0.3 mW blue: p<0.0001, red vs 0.2 mW blue: p<0.0001) and area (repeated measures ANOVA, $_{F2,16}$=404.2, p<0.0001, red vs 0.3 mW blue: p<0.0001, red vs 0.2 mW blue: p<0.0001) than either 0.3 mW or 0.2 mW blue light.

(G) Example EPSP and IPSP evoked by delivery of 635 nm red light alone (8 pulses, with 5 ms pulse-width, at 30Hz) or during constant 470 nm blue light (0.3 mW) to mimic in vivo recording conditions.

(H) Peak amplitude and (I) area of optically-evoked potential elicited by 635 nm light alone, or during constant 470 nm light. Inset bar graphs show normalized data. Red light evoked a significantly smaller PSP in the presence of continuous blue light (peak amplitude: paired t-test: t_{11}=5.172, p=0.0003; potential area: paired t-test: t_{11}=6.431, p<0.0001) similar to a previous report (Stamatakis et al., 2018). Note that the wavelength of imaging light here (470 nm) is higher than for the nVoke miniature microscope (455±8 nm), so this experiment may overestimate the constant blue light- induced suppression of red light-evoked potentials.

(J) Social:object ratio and (K) total social cup interaction time during GH stimulation and no stimulation sessions and 24 hours isolated session for DRN^{DAT}-CeA:TdTomato control animals (*N*=2 mice).

(L) Difference in response strength (Δ auROC) of CeA neurons to social and object cups in DRN^{DAT}-CeA:TdTomato control mice (GH off: *n*=39 cells, *N*=2 mice; GH on: *n*=61 cells, *N*=2 mice; SI off: *n*=76 cells, *N*=2 mice; one-way ANOVA: $F_{2,173}$=0.4183, p=0.6588)

(M) (top) ROC curves generated by aligning an example CeA neuron's calcium trace to interaction with the social (blue) or object (gold) cup in the three-chamber sociability task. This example neuron is classified as having an excitatory response to the social stimulus while having a neutral response to the object cup. (bottom) Calcium dynamics of example CeA neuron aligned to mouse's behavior. Blue shading indicates interaction with the social cup, while gold shading indicates interaction with the object cup.

(N) No correlation was found between social preference in three chamber task and the proportion of CeA neurons that have a significantly excitatory response to the object cup (Pearson's correlation: GH off – r=-0.3231, p=0.6328, *N*=9; GH on – r=-0.1152, p=0.7679, *N*=8; SI off – r=0.3438, p=0.3307, *N*=9).

(O) No correlation was found between social preference in three chamber task and the proportion of CeA neurons that have a significantly inhibitory response to the social cup (Pearson's correlation: GH off – r=0.1729, p=0.3625, *N*=9 mice; GH on – r=-0.3941, p=0.2939, *N*=8 mice; SI off – r=0.0116, p=0.9745, *N*=9 mice).

Bar and line graphs show mean ±SEM. ***p<0.001, ****p<0.0001.

Figure 7—figure supplement 2. Ex vivo validation of simultaneous calcium imaging and photostimulation and behavioral and neural effects of DRN^{DAT}-CeA:TdTomato stimulation in CeA.

(A) Agglomerative hierarchical clustering of trial-averaged CeA traces aligned to interaction with the social or object cup. The dendrogram (left) reveals 12 functional clusters of neurons, as displayed by the heatmap of trial-averaged neural activity (right).

(B) Cluster-averaged traces aligned to the onset of social cup (blue) or object cup (gold) interaction for each cluster. The percentage of neurons per condition is listed in each inset.

Line graphs show mean ±SEM.

Figure 8. DRN^{DAT}-CeA photoinhibition blocks isolation-induced sociability.

(A) AAV_5-DIO-NpHR-eYFP or AAV_5-DIO-eYFP was injected into the DRN of DAT::Cre mice and optic fibers implanted over the BNST, CeA, or BLP to photoinhibit DRN^{DAT} terminals.

(B) After >7 weeks for viral expression mice were assayed on the three-chamber sociability assay with delivery of continuous yellow light for photoinhibition, once when group-housed and once following 24 hours of social isolation (2-3 weeks after the initial session).

(C) Photoinhibition of DRN^{DAT}-BNST terminals in NpHR-expressing mice (DRN^{DAT}-BNST:NpHR) had no significant effect on time spent in the social zone relative to the object zone (DRN^{DAT}-BNST:NpHR: *N*=7 mice, DRN^{DAT}-BNST:eYFP: *N*=5 mice; 'social:object ratio'; two-way RM ANOVA: light x group interaction, $F_{1,10}$=1.005, p=0.3397), but reduced social:object ratio for isolated DRN^{DAT}-CeA:NpHR mice compared to isolated DRN^{DAT}-CeA:eYFP mice (DRN^{DAT}-CeA:NpHR: *N*=20 mice, DRN^{DAT}-CeA:eYFP: *N*=12 mice; 'social:object ratio'; two-way RM ANOVA: light x group interaction, $F_{1,30}$=4.909, p=0.0344; multiple comparisons test, DRN^{DAT}-CeA:$NpHR^{SI}$ vs DRN^{DAT}-CeA:$eYFP^{SI}$ adjusted **p=0.0017). In addition, terminal photoinhibition had no effect for DRN^{DAT}-BLP:NpHR mice (DRN^{DAT}-BLP:NpHR: *N*=6 mice, DRN^{DAT}-BLP:eYFP: *N*=8 mice; 'social:object ratio'; two-way RM ANOVA: light x group interaction, $F_{1,12}$=3.346, p=0.0923). Inset bar graphs show the difference in social:object ratio in isolated and grouped conditions. A significant difference between $NpHR^{CeA}$ and $eYFP^{CeA}$ groups was observed (unpaired t-test: t_{29}=2.177, p=0.0377).

(D) Scatter plots displaying relative dominance plotted against the change in social zone time (isolated-grouped), showing significant negative correlation in $NpHR^{CeA}$ mice (Pearson's correlation: r=-0.500, p=0.0414, *N*=20 mice).

Bar and line graphs show mean ±SEM. *p<0.05, **p<0.01.

Source data 1. DRN^{DAT}-ALL:NpHR three-chamber social:object ratio (GH on and SI on), as shown in ***Figure 8C.***

Source data 2. DRN^{DAT}-ALL:NpHR three-chamber social:object ratio (SI – GH) x relative dominance, as shown in ***Figure 8D.***

Figure supplement 1—source data 1. DRN^{DAT}-ALL:NpHR three-chamber social:object ratio (GH off and GH on), as shown in ***Figure 8—figure supplement 1B***.

Figure 8—figure supplement 1. Photoinhibition of DRN^{DAT}-BNST:NpHR, DRN^{DAT}-BNST:NPHR, DRN^{DAT}-BLP:NpHR terminals does not affect social preference in group housed mice.

(A) Schematic showing three-chamber behavior paradigm in group-housed DRN^{DAT}:NpHR or DRN^{DAT}:eYFP mice, with and without yellow light for photoinhibition.

(B) Photoinhibition had no significant effect on social:object ratio in group-housed mice (two-way ANOVA, light x group interaction, BNST – $F_{1,11}$ p=0.4571, DRN^{DAT}-BNST:NpHR: *N*=7 mice, DRN^{DAT}-BNST:eYFP: *N*=5 mice; CeA – $F_{1,31}$=0.1353, p=0.7154, DRN^{DAT}-CeA:NpHR: *N*=20 mice, DRN^{DAT}-CeA:eYFP: *N*=12 mice; BLP – $F_{1,14}$=2.517, p=0.1349, DRN^{DAT}-BLP:NpHR: *N*=6 mice, DRN^{DAT}-BLP:eYFP: *N*=8 mice).

Line and bar graphs show mean±SEM.

Figure 1

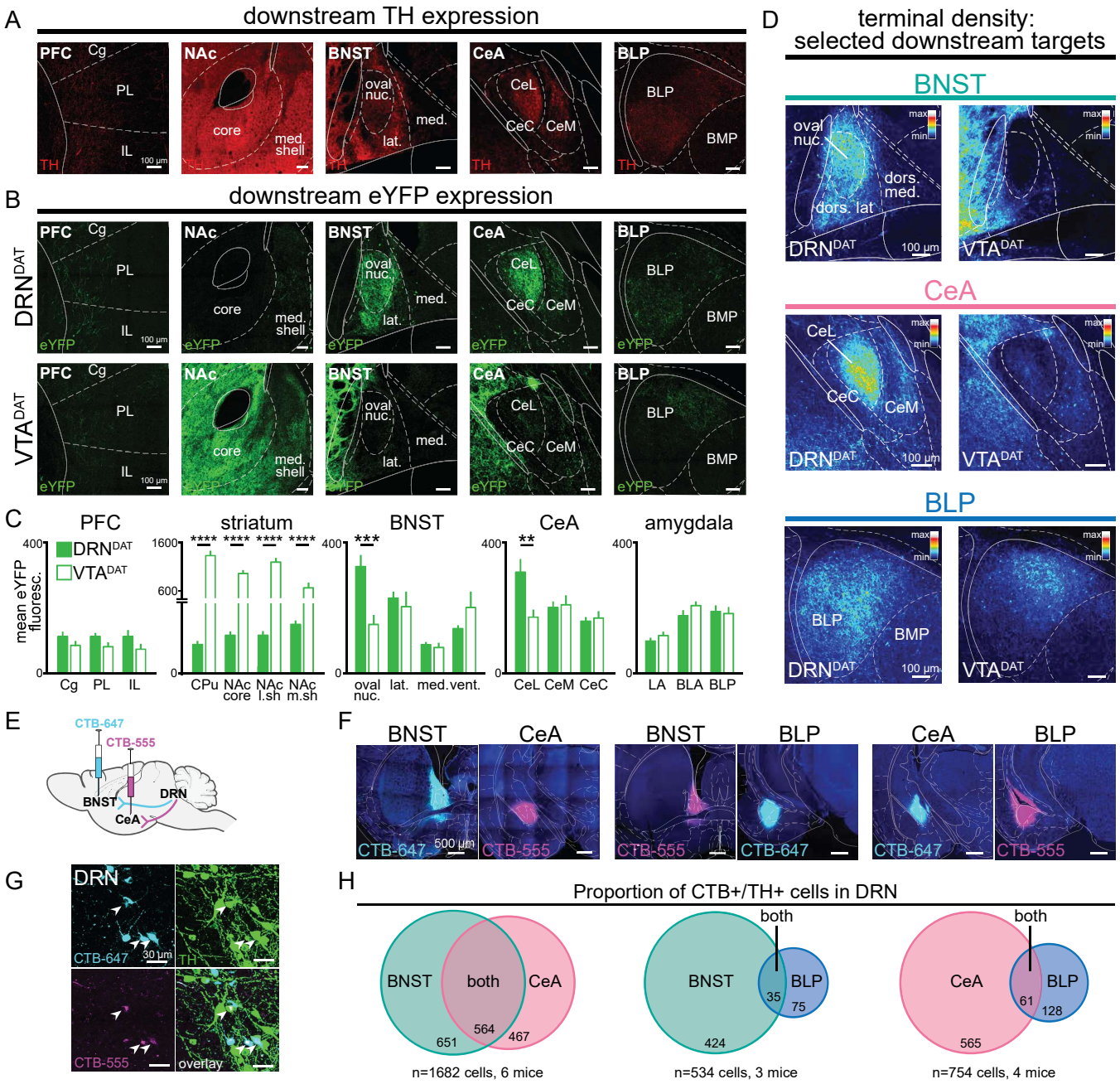
A
downstream TH expression
PFC
Cg
PL
IL
NAc
core
med. shell
BNST
oval nuc.
med.
lat.
CeA
CeL
CeC
CeM
BLP
BMP
TH
100 µm
B
downstream eYFP expression
DRN DAT
VTA DAT
eYFP
C
PFC
striatum
BNST
CeA
amygdala
mean eYFP fluoresc.
DRN DAT
VTA DAT
Cg PL IL
CPu NAc core NAc l.sh NAc m.sh
oval nuc. lat. med. vent.
CeL CeM CeC
LA BLA BLP
D
terminal density: selected downstream targets
BNST
CeA
BLP
max
min
dors. med.
dors. lat
100 µm
E
CTB-647
CTB-555
BNST
DRN
CeA
F
BNST
CeA
BLP
500 µm
G
DRN
CTB-647
30 µm
TH
CTB-555
overlay
H
Proportion of CTB+/TH+ cells in DRN
BNST
both
CeA
651
564
467
n=1682 cells, 6 mice
BLP
35
75
424
n=534 cells, 3 mice
61
128
565
n=754 cells, 4 mice

Figure 1--figure supplement 1

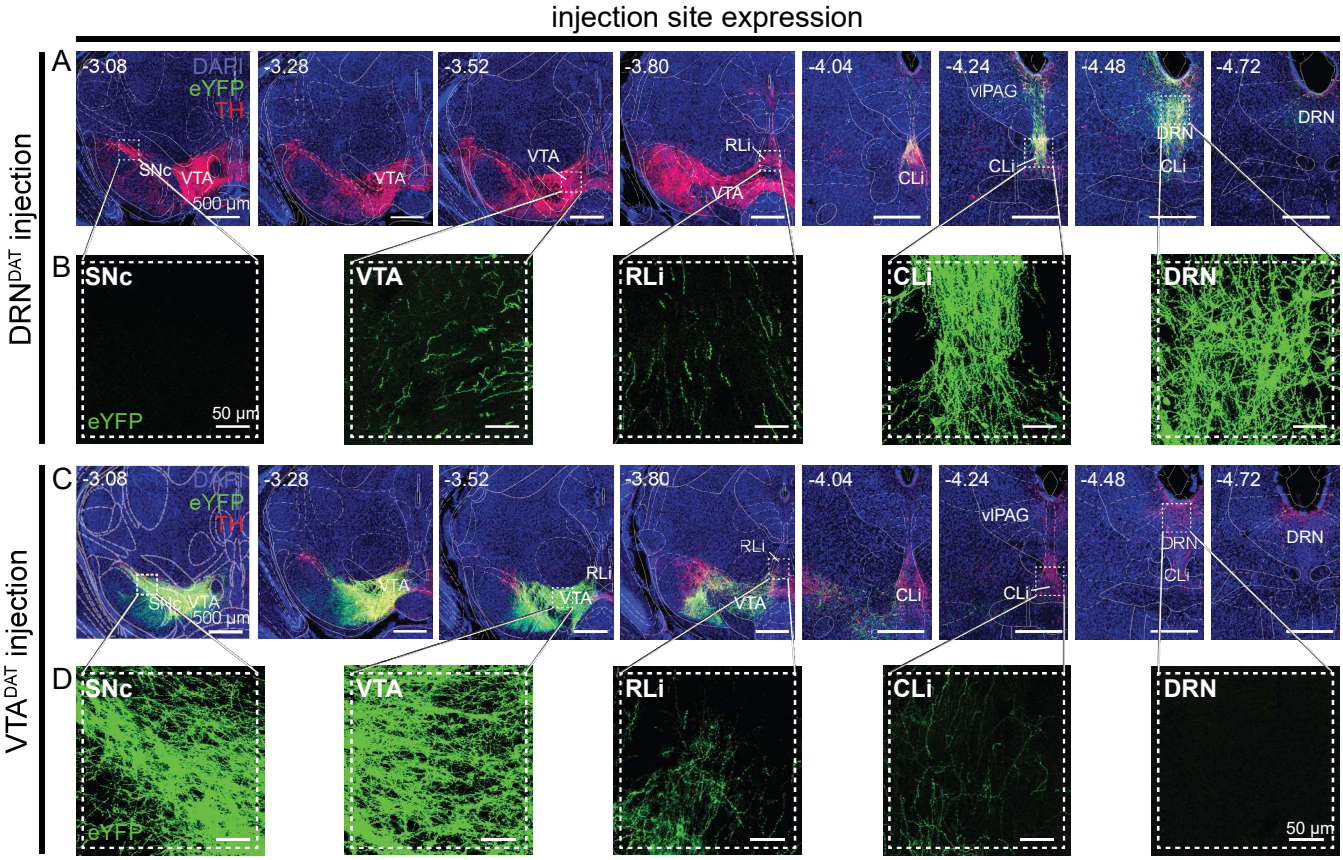

Figure 1--figure supplement 2

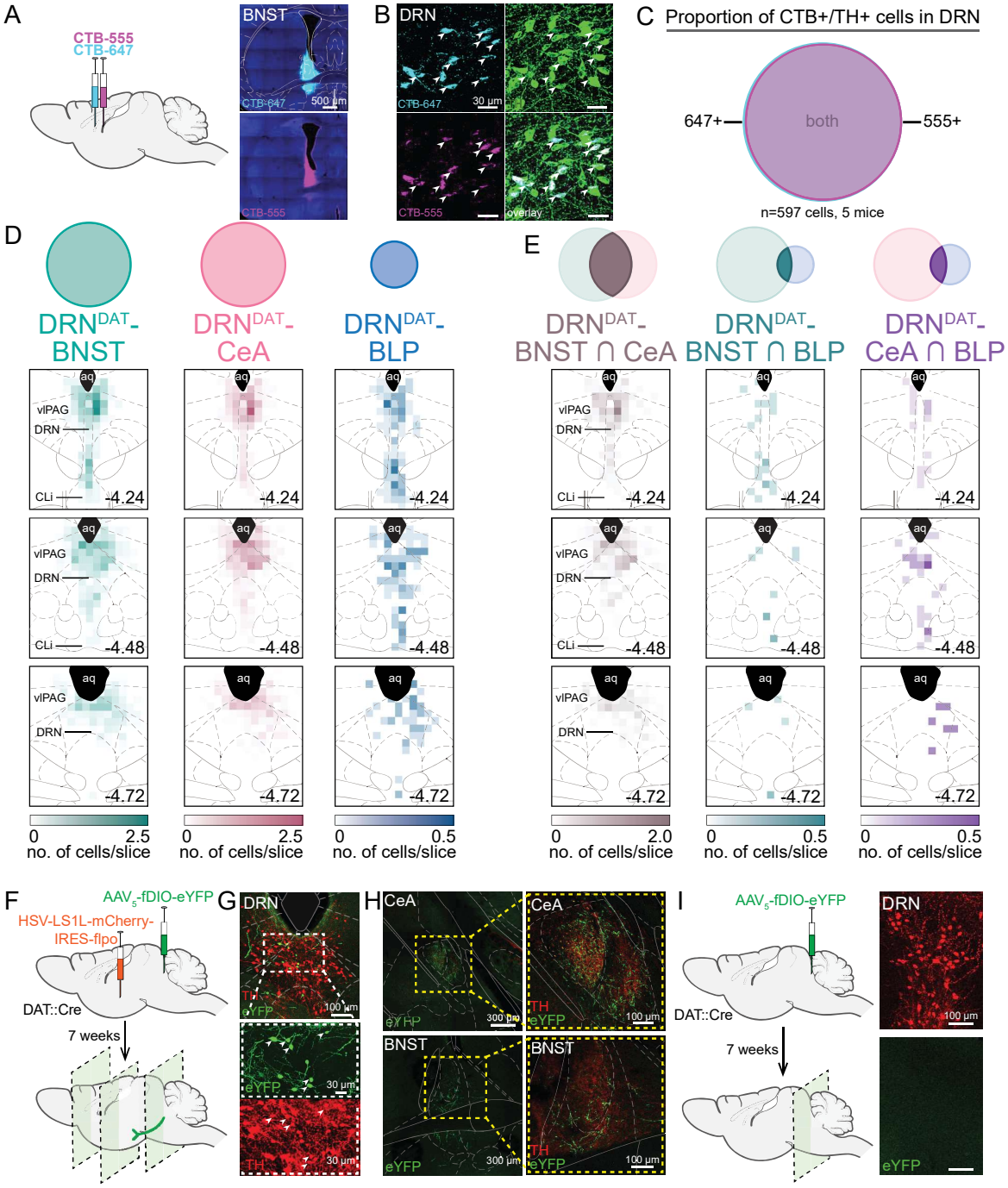

Figure 2

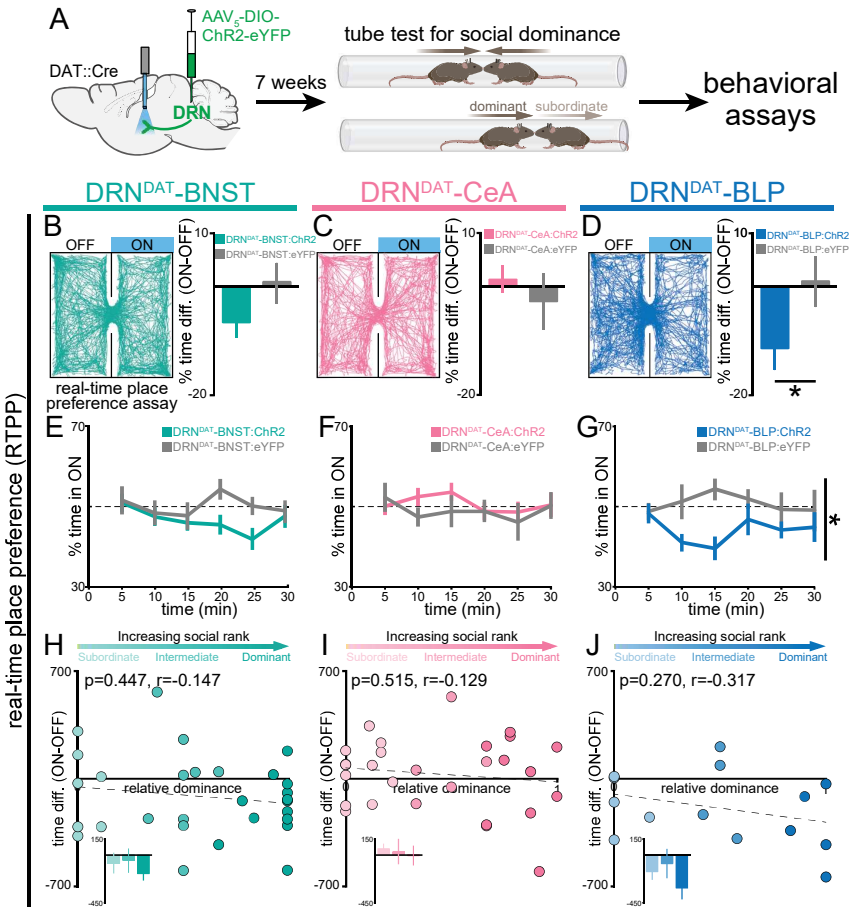
A
AAV5-DIO-ChR2-eYFP
DAT::Cre
DRN
7 weeks
tube test for social dominance
dominant
subordinate
behavioral assays
DRNDAT-BNST
DRNDAT-CeA
DRNDAT-BLP
B
C
D
OFF
ON
real-time place preference assay
% time diff. (ON-OFF)
DRNDAT-BNST:ChR2
DRNDAT-BNST:eYFP
DRNDAT-CeA:ChR2
DRNDAT-CeA:eYFP
DRNDAT-BLP:ChR2
DRNDAT-BLP:eYFP
E
F
G
% time in ON
time (min)
H
I
J
Increasing social rank
Subordinate
Intermediate
Dominant
p=0.447, r=-0.147
p=0.515, r=-0.129
p=0.270, r=-0.317
relative dominance
time diff. (ON-OFF)
real-time place preference (RTPP)

Figure 2--figure supplement 1

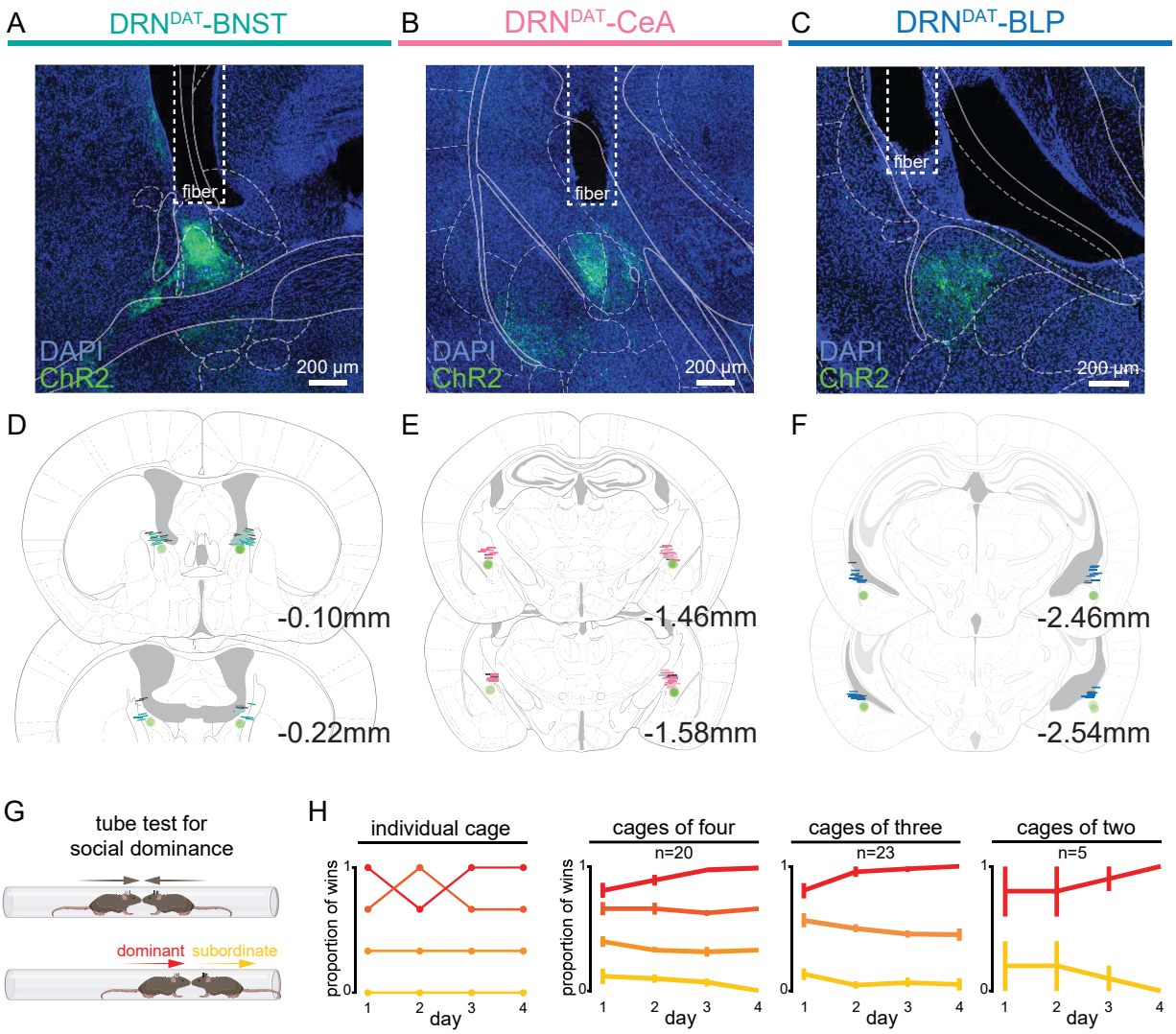

Figure 2--figure supplement 2

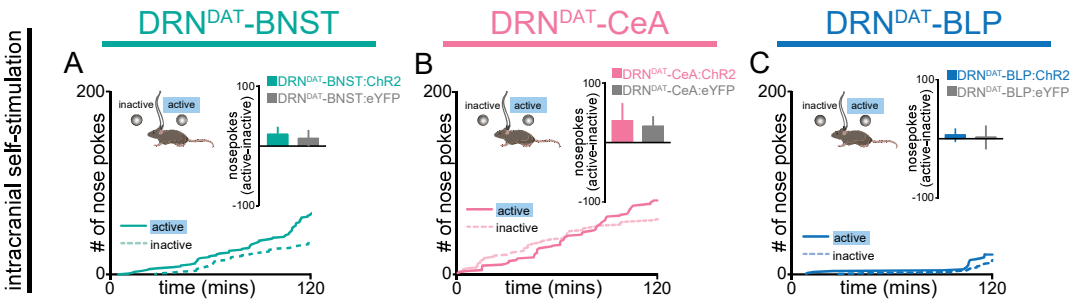

Figure 3

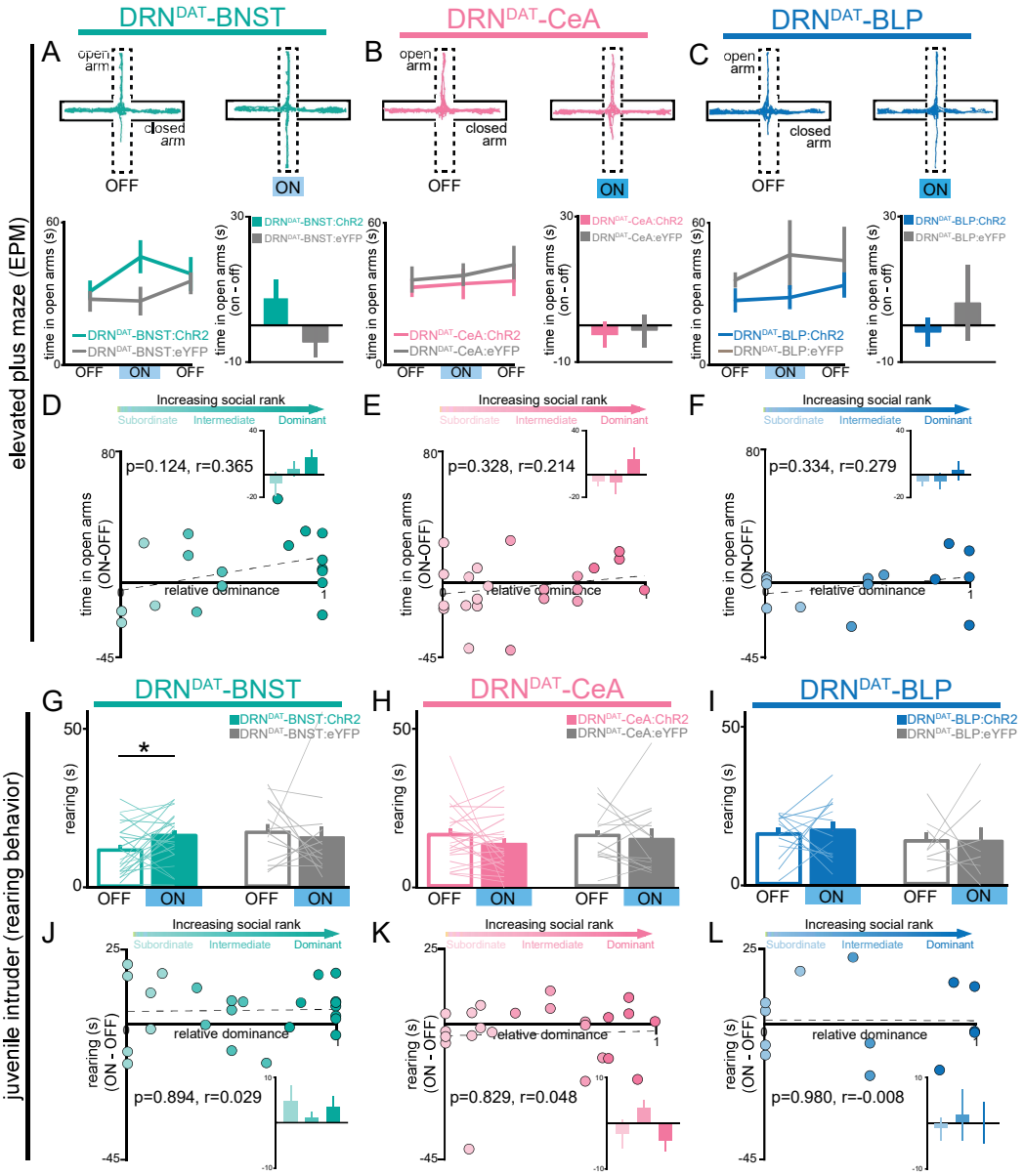
DRNDAT-BNST
DRNDAT-CeA
DRNDAT-BLP
elevated plus maze (EPM)
juvenile intruder (rearing behavior)
open arm
closed arm
OFF
ON
time in open arms (s)
time in open arms (on - off)
DRNDAT-BNST:ChR2
DRNDAT-BNST:eYFP
DRNDAT-CeA:ChR2
DRNDAT-CeA:eYFP
DRNDAT-BLP:ChR2
DRNDAT-BLP:eYFP
Increasing social rank
Subordinate
Intermediate
Dominant
p=0.124, r=0.365
p=0.328, r=0.214
p=0.334, r=0.279
time in open arms (ON-OFF)
relative dominance
rearing (s)
*
rearing (s) (ON - OFF)
p=0.894, r=0.029
p=0.829, r=0.048
p=0.980, r=-0.008

Figure 3--figure supplement 1

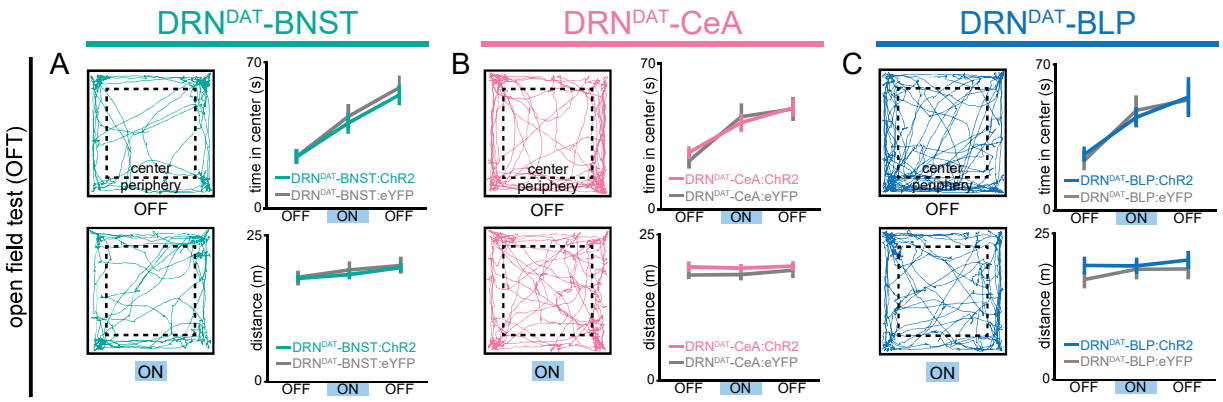

Figure 4

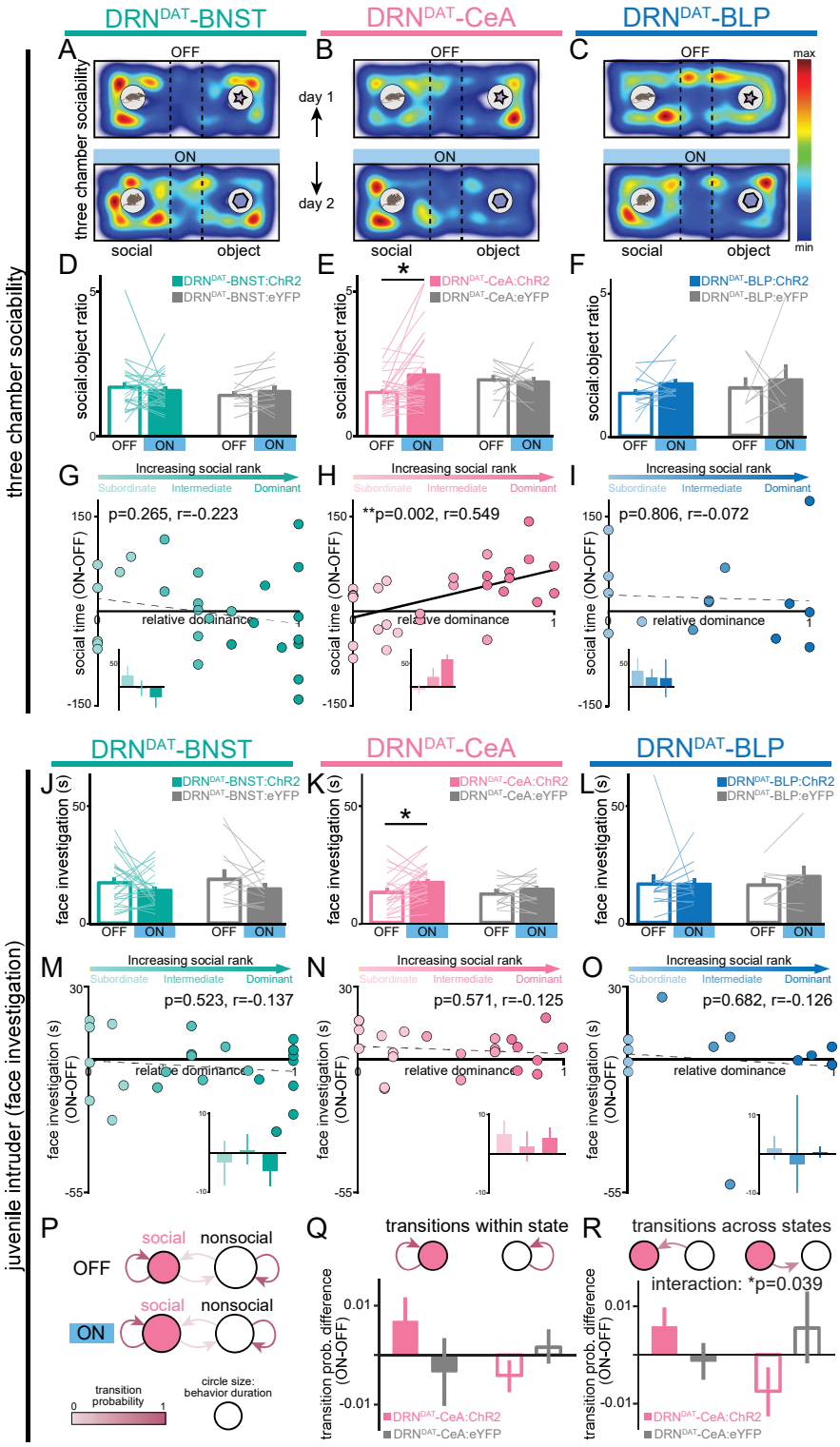
DRNDAT-BNST
DRNDAT-CeA
DRNDAT-BLP
three chamber sociability
A
B
C
OFF
ON
day 1
day 2
max
min
social
object
D
E
F
DRNDAT-BNST:ChR2
DRNDAT-BNST:eYFP
DRNDAT-CeA:ChR2
DRNDAT-CeA:eYFP
DRNDAT-BLP:ChR2
DRNDAT-BLP:eYFP
social:object ratio
G
H
I
Increasing social rank
Subordinate
Intermediate
Dominant
p=0.265, r=-0.223
**p=0.002, r=0.549
p=0.806, r=-0.072
social time (ON-OFF)
relative dominance
juvenile intruder (face investigation)
J
K
L
face investigation (s)
M
N
O
p=0.523, r=-0.137
p=0.571, r=-0.125
p=0.682, r=-0.126
face investigation (s) (ON-OFF)
P
social
nonsocial
transition probability
circle size: behavior duration
Q
transitions within state
R
transitions across states
interaction: *p=0.039
transition prob. difference (ON-OFF)

Figure 4--figure supplement 1

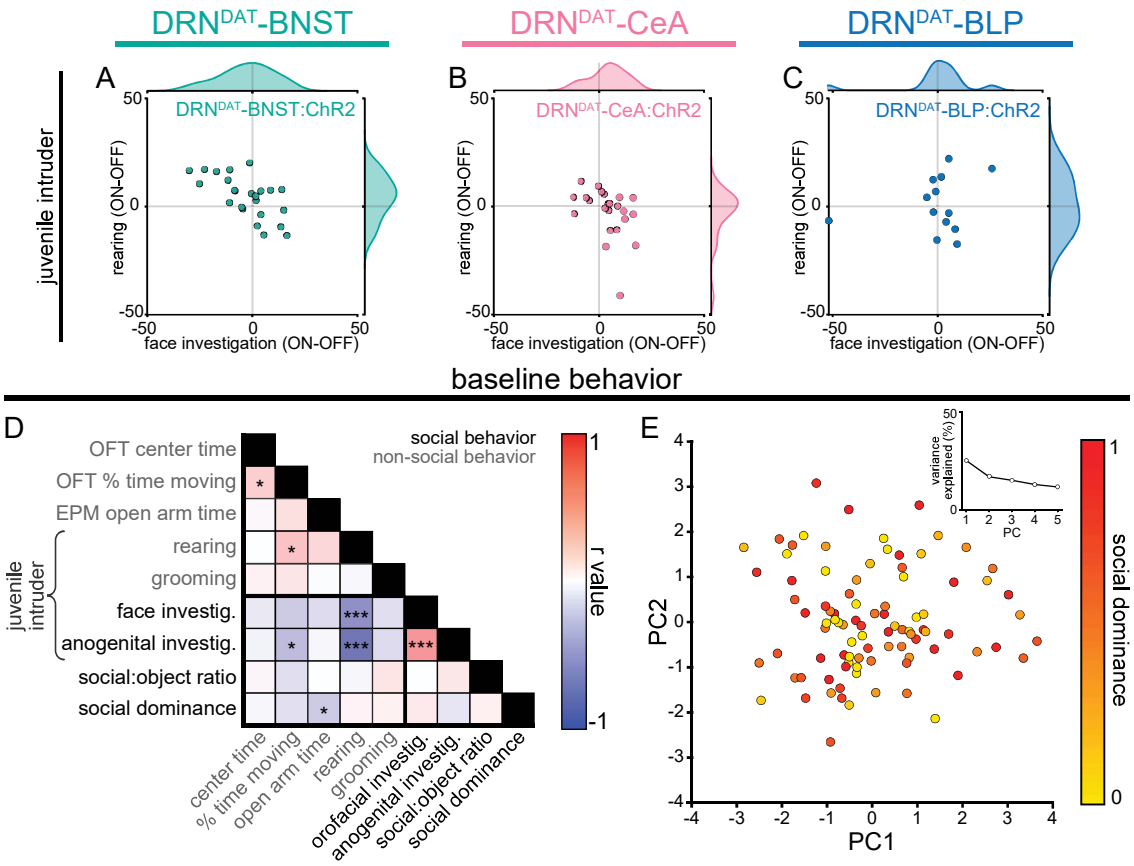

Figure 5

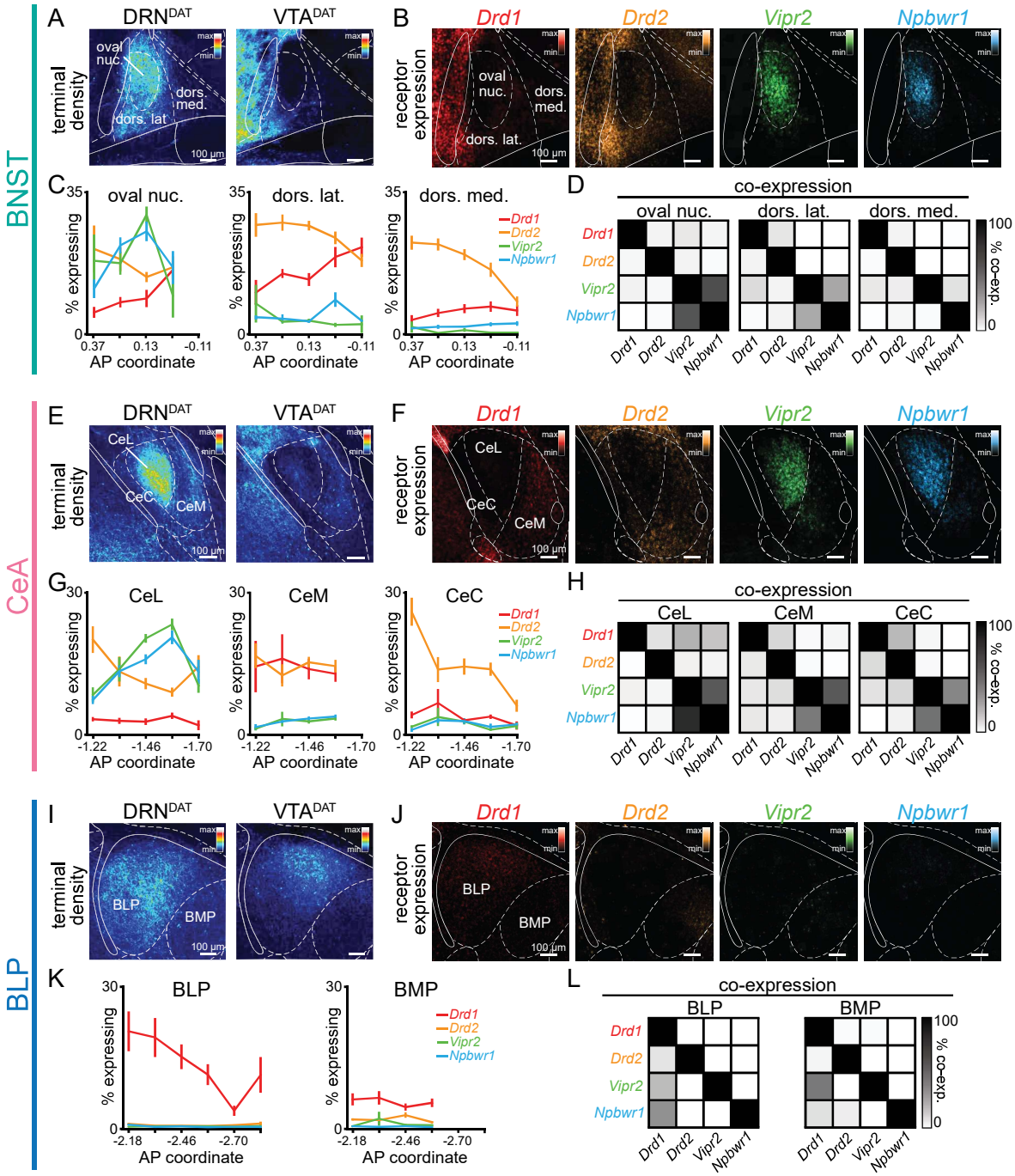
BNST
A
DRN^DAT
VTA^DAT
terminal density
oval nuc.
dors. med.
dors. lat.
100 µm
B
Drd1
Drd2
Vipr2
Npbwr1
receptor expression
C
oval nuc.
dors. lat.
dors. med.
% expressing
AP coordinate
D
co-expression
% co-exp.
CeA
E
CeL
CeC
CeM
F
G
H
BLP
I
BLP
BMP
J
K
L

Figure 5--figure supplement 1

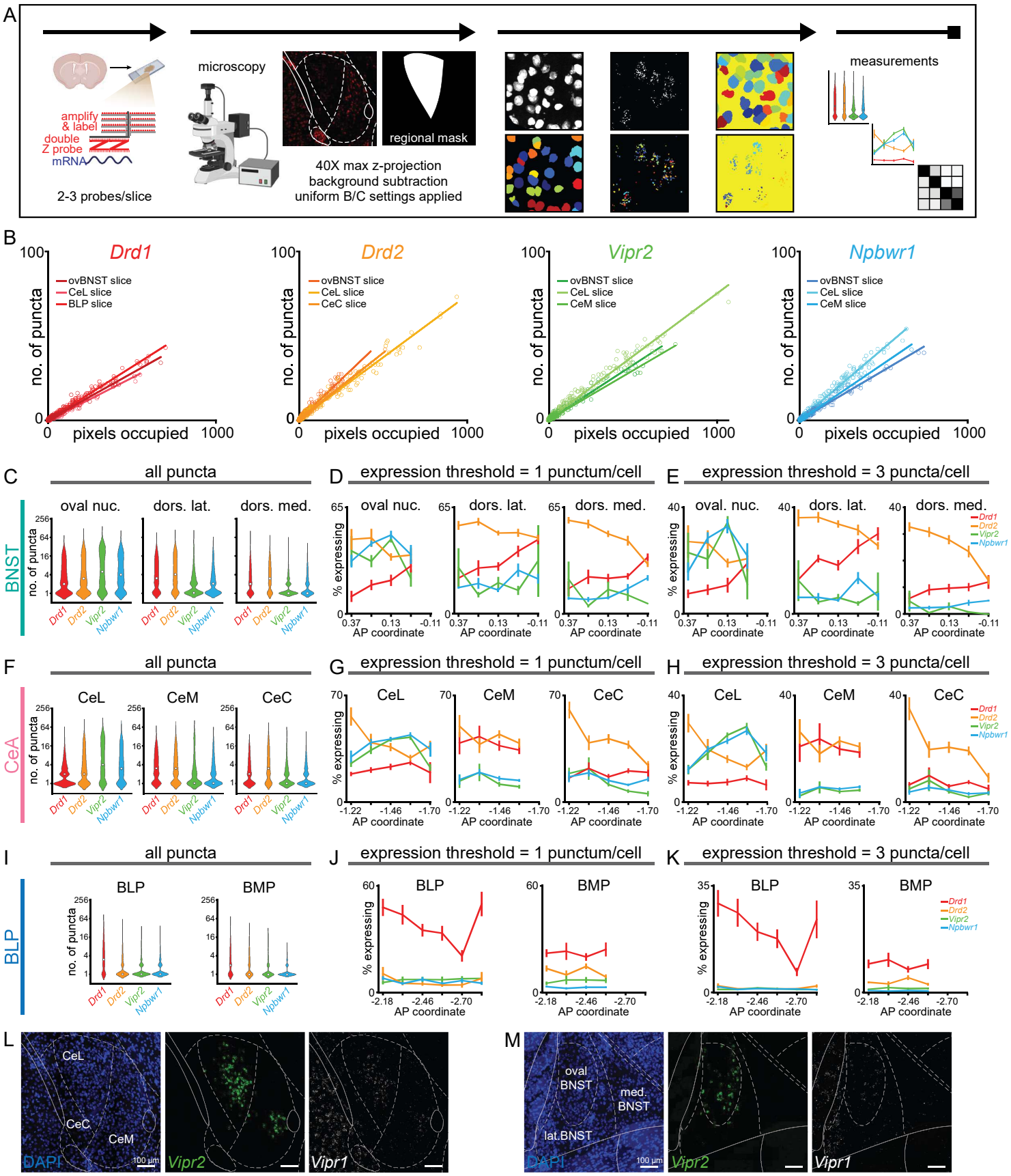

Figure 6

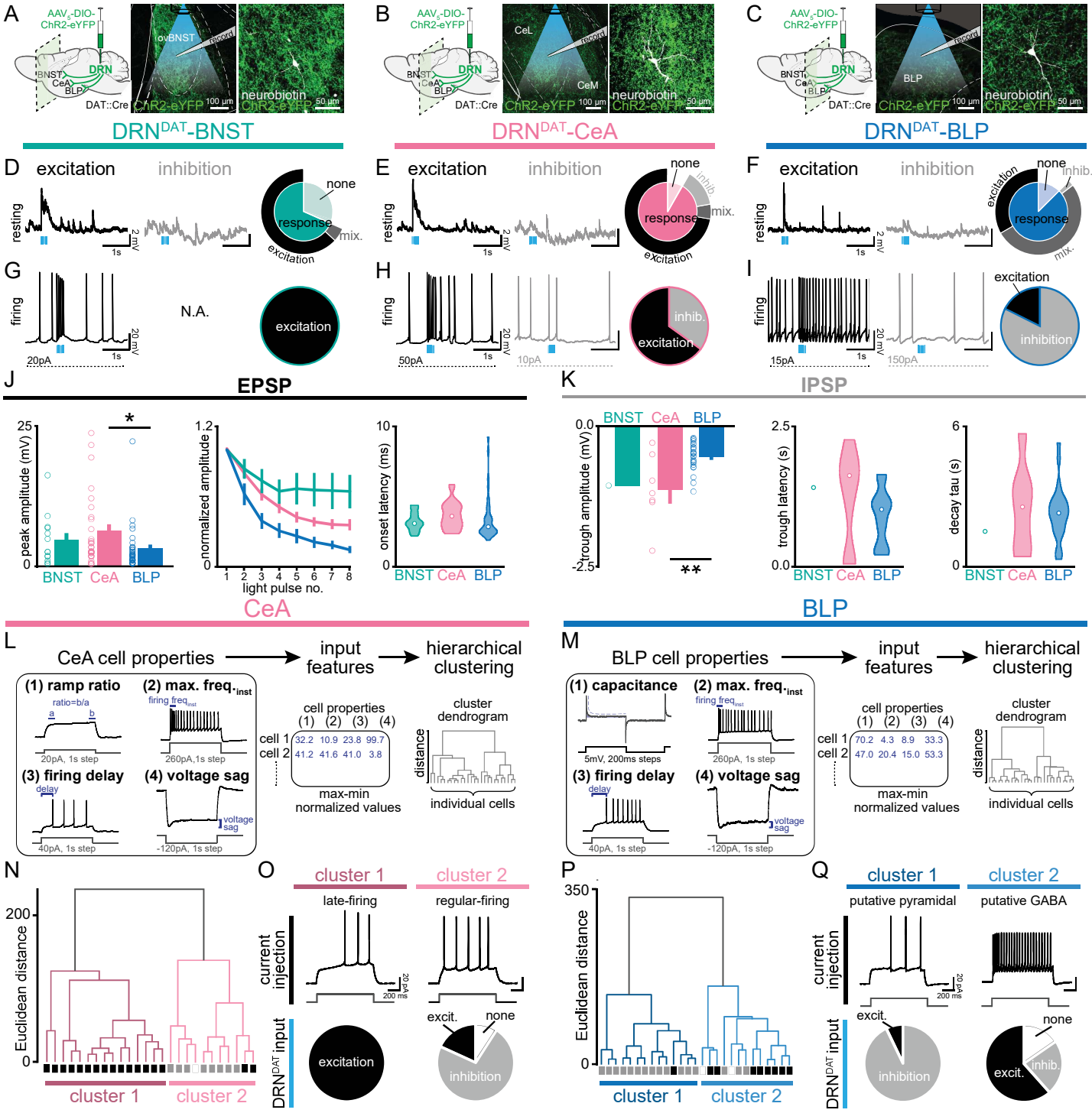
A
AAV5-DIO-ChR2-eYFP
BNST
CeA
BLP
DRN
DAT::Cre
ovBNST
record
ChR2-eYFP
100 µm
neurobiotin
50 µm
DRNDAT-BNST
B
CeL
CeM
DRNDAT-CeA
C
BLP
DRNDAT-BLP
D
excitation
inhibition
resting
1s
2 mV
none
response
mix.
excitation
E
F
G
firing
20 mV
20pA
N.A.
excitation
H
50pA
10pA
inhib.
I
15pA
150pA
J
EPSP
peak amplitude (mV)
BNST CeA BLP
normalized amplitude
light pulse no.
onset latency (ms)
CeA
K
IPSP
trough amplitude (mV)
trough latency (s)
decay tau (s)
BLP
L
CeA cell properties
input features
hierarchical clustering
(1) ramp ratio
ratio=b/a
(2) max. freq.inst
firing freqinst
20pA, 1s step
260pA,1s step
(3) firing delay
delay
(4) voltage sag
voltage sag
40pA, 1s step
-120pA, 1s step
cell properties
(1) (2) (3) (4)
cell 1 32.2 10.9 23.8 99.7
cell 2 41.2 41.6 41.0 3.8
max-min normalized values
cluster dendrogram
distance
individual cells
M
BLP cell properties
(1) capacitance
5mV, 200ms steps
cell 1 70.2 4.3 8.9 33.3
cell 2 47.0 20.4 15.0 53.3
N
Euclidean distance
cluster 1
cluster 2
O
late-firing
regular-firing
current injection
20 pA
200 ms
DRNDAT input
excit.
none
inhibition
P
Q
putative pyramidal
putative GABA

Figure 6--figure supplement 1

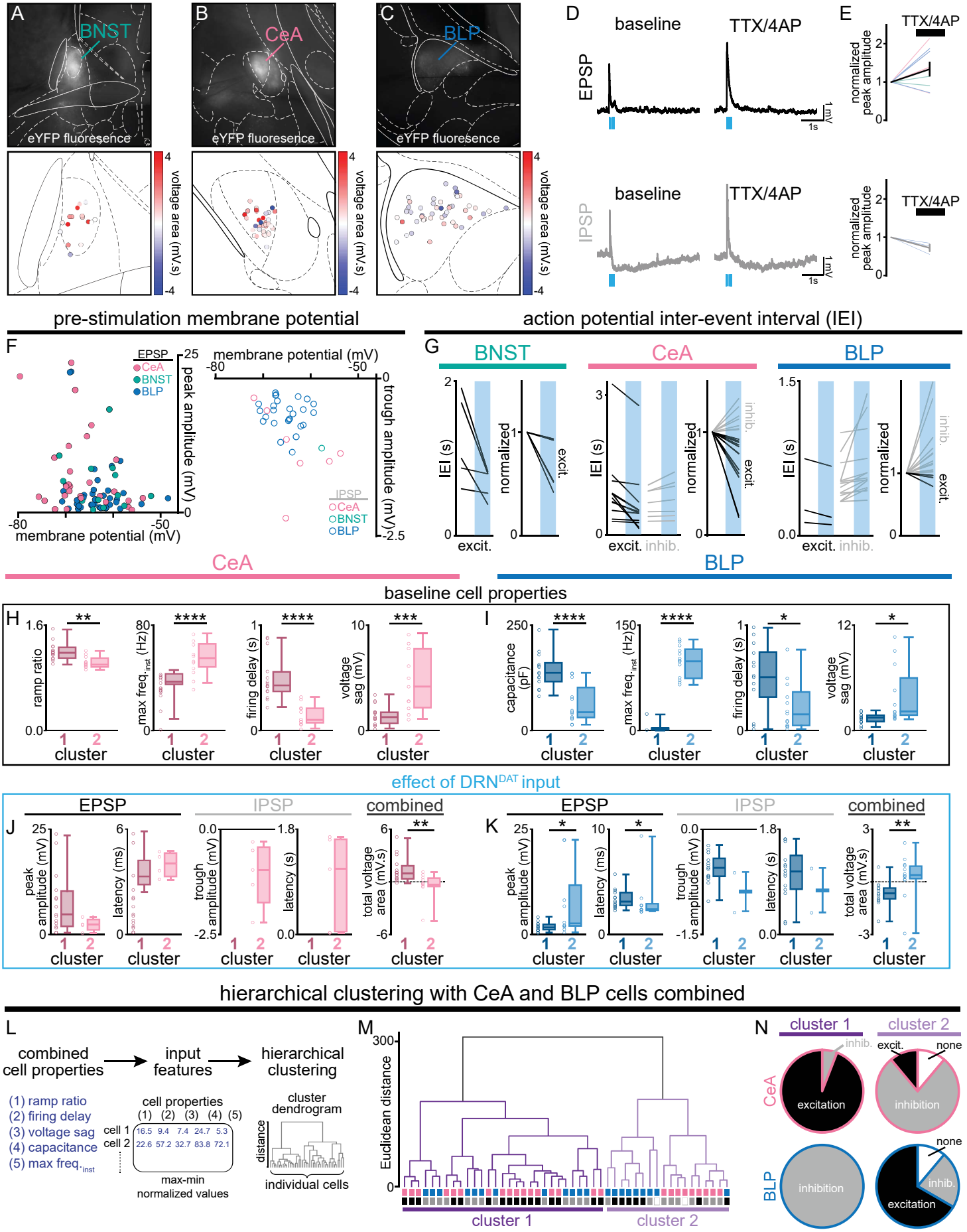

Figure 7

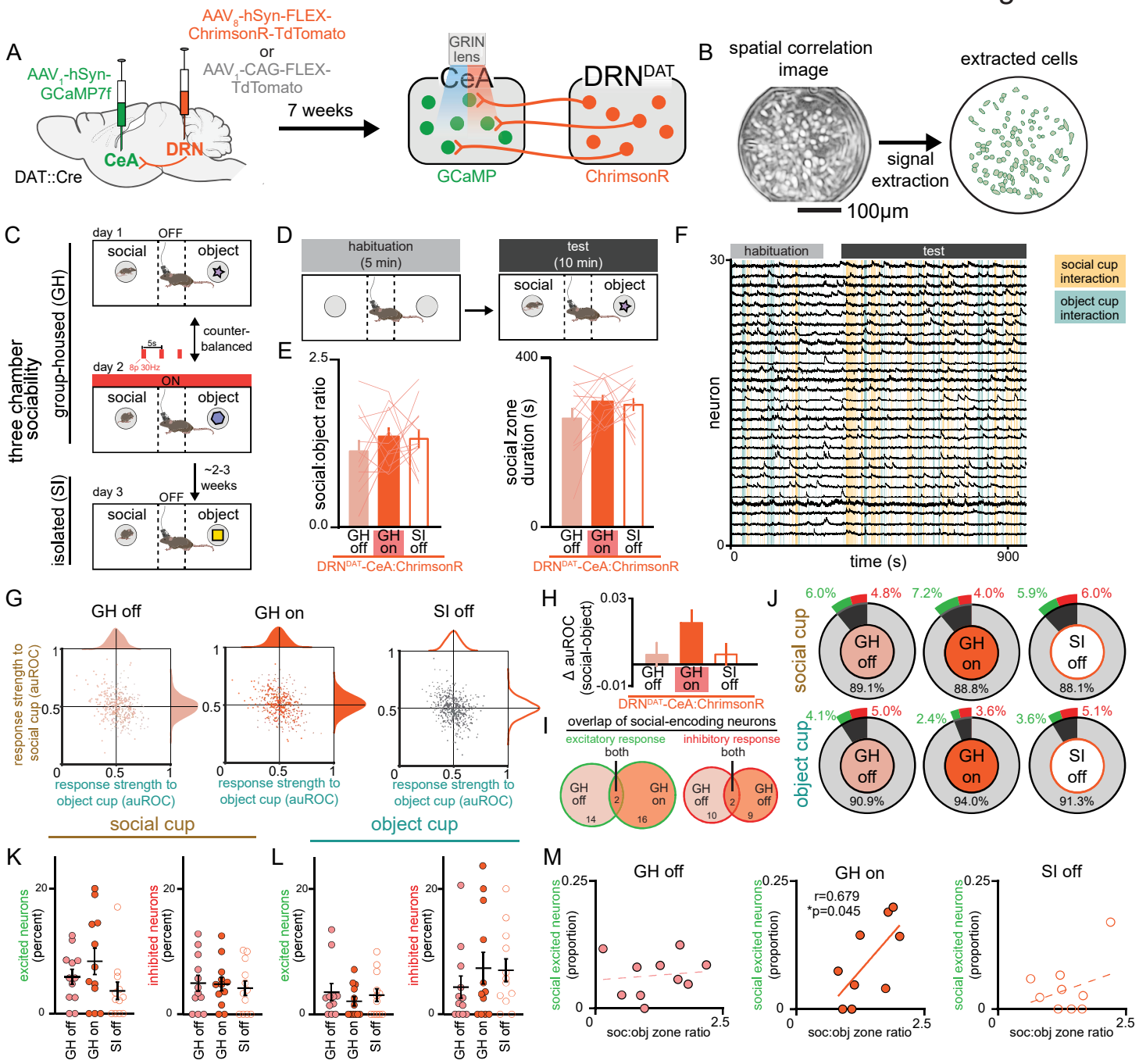
A
AAV8-hSyn-FLEX-ChrimsonR-TdTomato
or
AAV1-CAG-FLEX-TdTomato
AAV1-hSyn-GCaMP7f
CeA
DRN
DAT::Cre
7 weeks
GRIN lens
CeA
DRNDAT
GCaMP
ChrimsonR
B
spatial correlation image
extracted cells
signal extraction
100µm
C
three chamber sociability
group-housed (GH)
isolated (SI)
day 1
OFF
social
object
counter-balanced
day 2
ON
day 3
~2-3 weeks
D
habituation (5 min)
test (10 min)
E
social:object ratio
social zone duration (s)
GH off
GH on
SI off
DRNDAT-CeA:ChrimsonR
F
habituation
test
social cup interaction
object cup interaction
neuron
time (s)
G
GH off
GH on
SI off
response strength to social cup (auROC)
response strength to object cup (auROC)
H
Δ auROC (social-object)
I
overlap of social-encoding neurons
excitatory response
inhibitory response
both
J
social cup
object cup
K
excited neurons (percent)
inhibited neurons (percent)
L
M
social excited neurons (proportion)
soc:obj zone ratio
r=0.679
*p=0.045

Figure 7--figure supplement 1

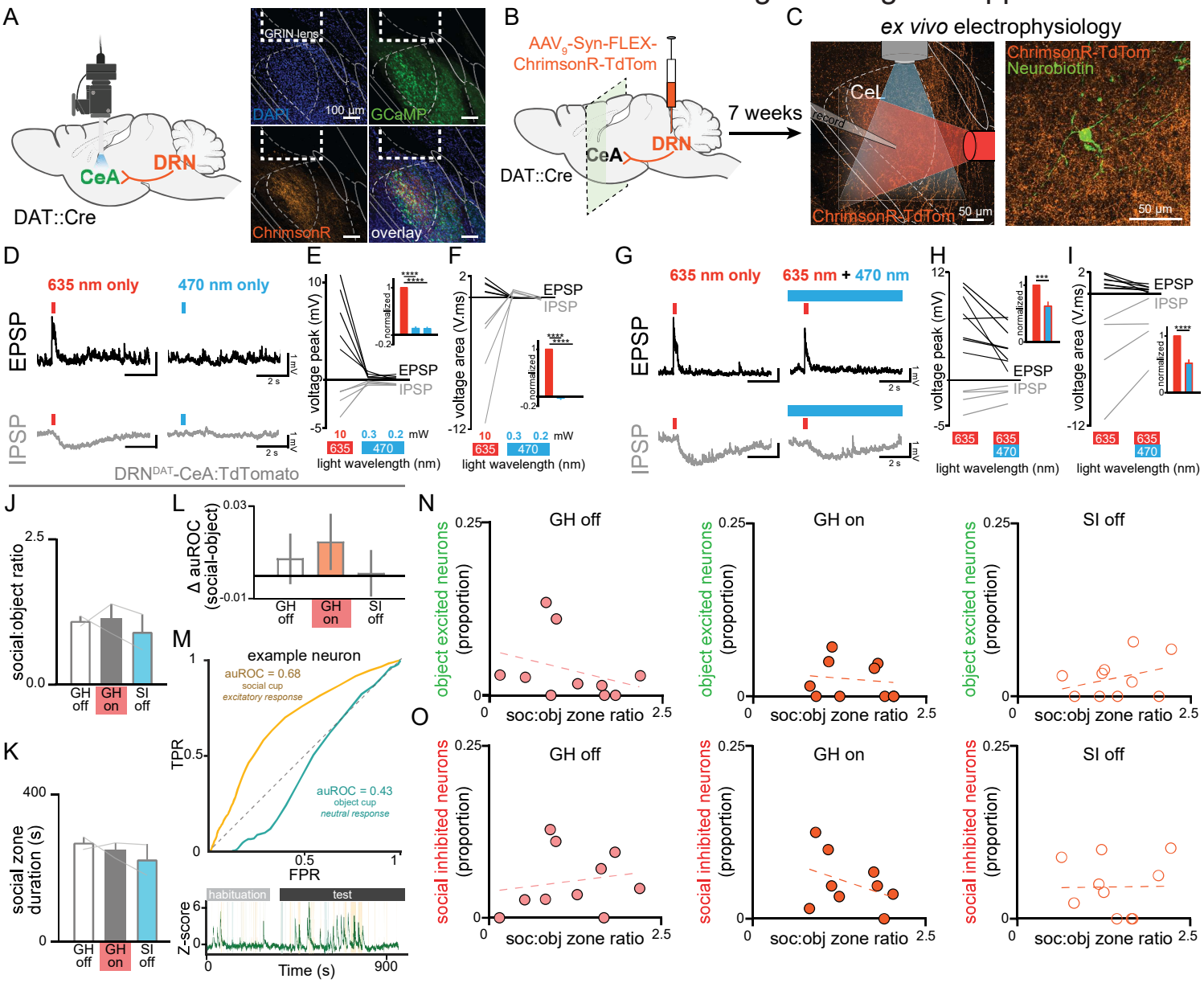

Figure 7--figure supplement 2

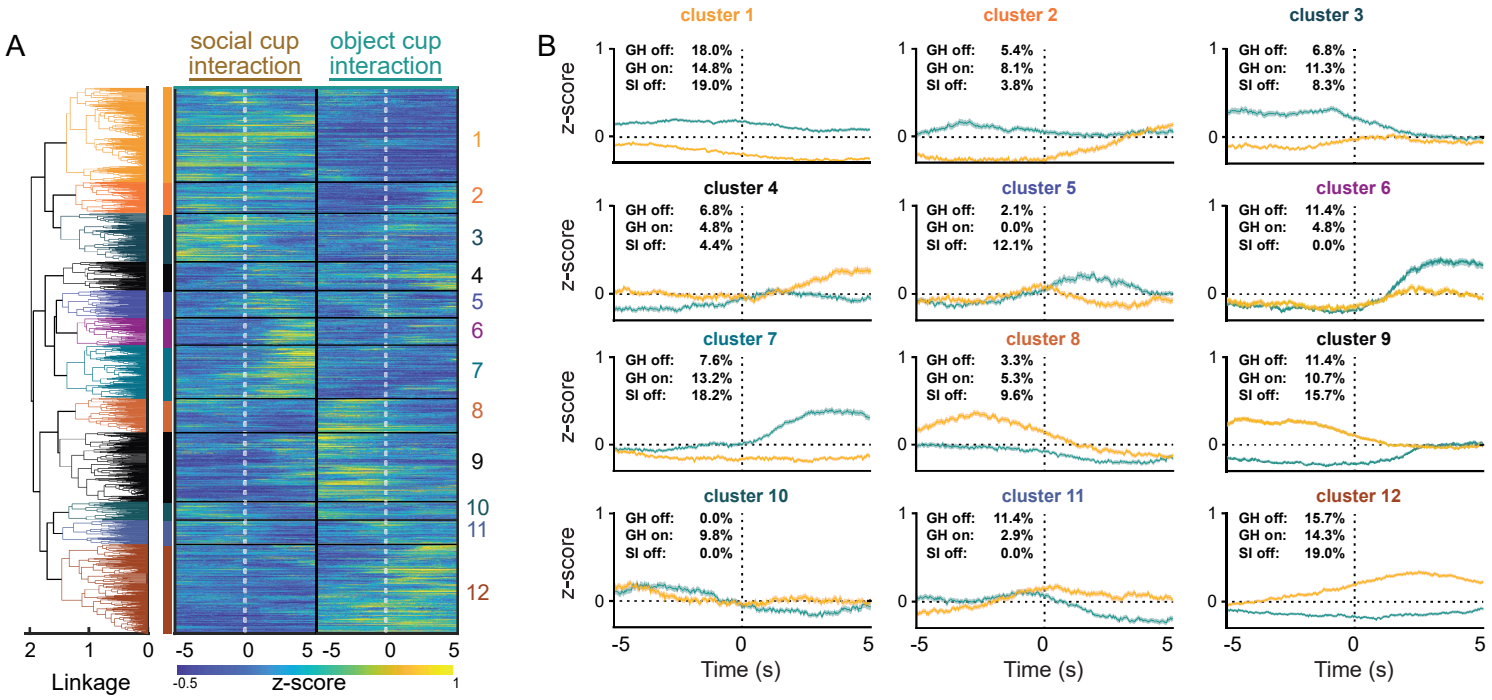

Figure 8

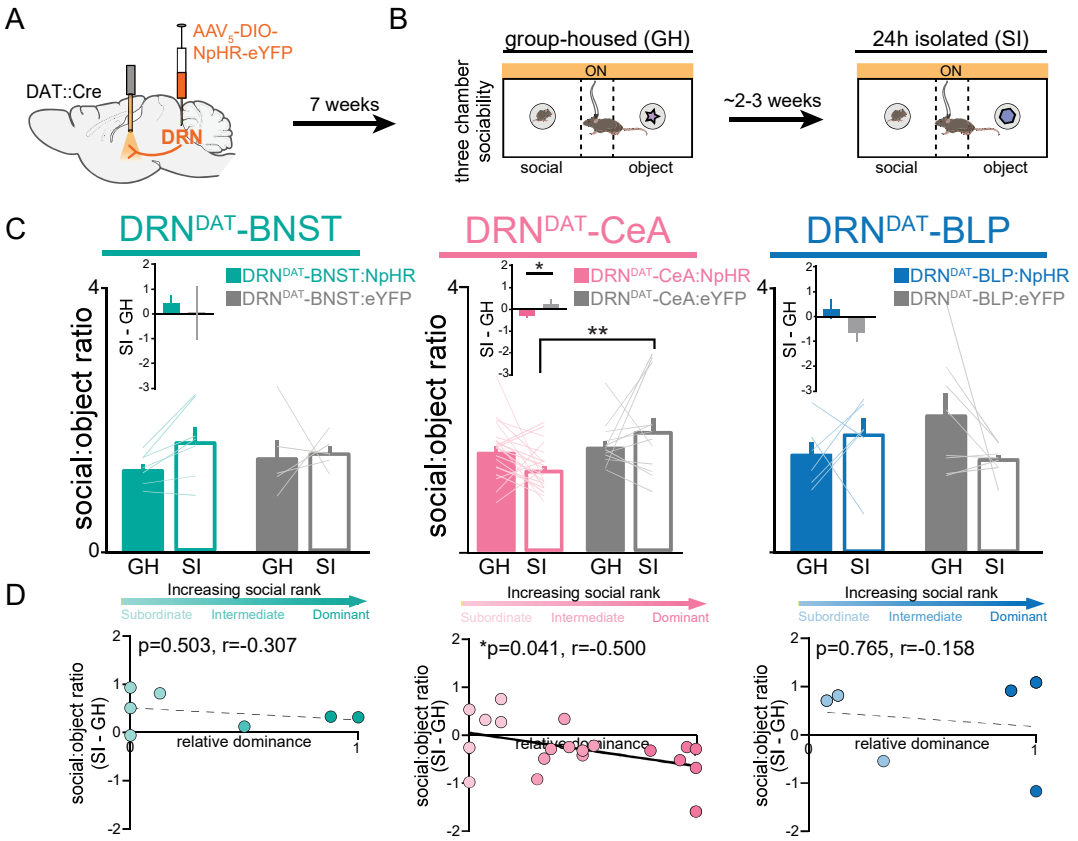
A
AAV5-DIO-NpHR-eYFP
DAT::Cre
DRN
7 weeks
B
group-housed (GH)
24h isolated (SI)
three chamber sociability
ON
social
object
~2-3 weeks
C
DRNDAT-BNST
DRNDAT-CeA
DRNDAT-BLP
DRNDAT-BNST:NpHR
DRNDAT-BNST:eYFP
DRNDAT-CeA:NpHR
DRNDAT-CeA:eYFP
DRNDAT-BLP:NpHR
DRNDAT-BLP:eYFP
social:object ratio
SI - GH
GH SI GH SI
Increasing social rank
Subordinate Intermediate Dominant
D
p=0.503, r=-0.307
*p=0.041, r=-0.500
p=0.765, r=-0.158
social:object ratio (SI - GH)
relative dominance
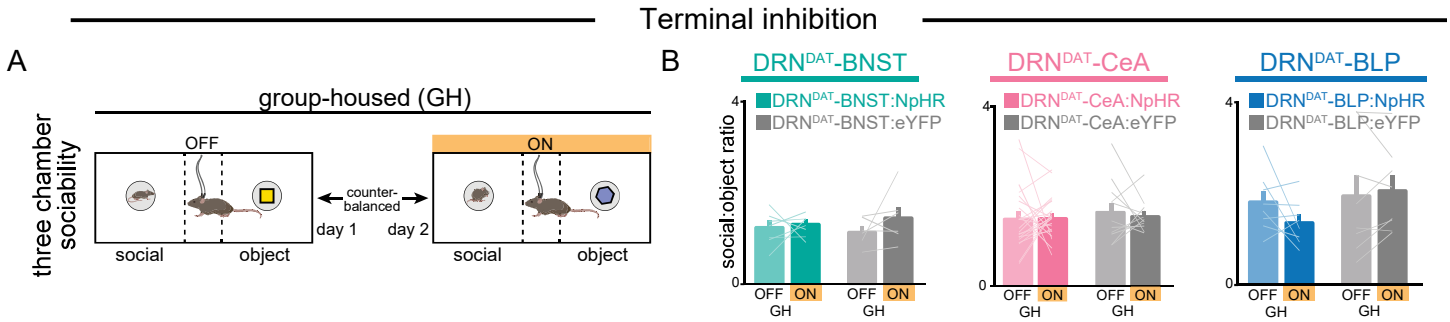
Figure 8--figure supplement 1